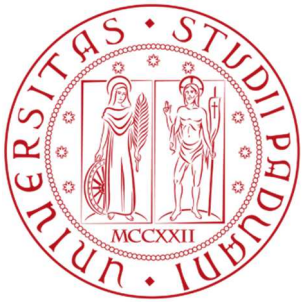

UNIVERSITÀ DEGLI STUDI DI PADOVA

Sede Amministrativa: Università degli Studi di Padova

Dipartimento di Ingegneria Industriale - DII

SCUOLA DI DOTTORATO DI RICERCA IN INGEGNERIA INDUSTRIALE

INDIRIZZO: INGEGNERIA DEI MATERIALI

CICLO XXXIV

Effect of additive manufacturing-induced anisotropy on machinability of Ti6Al4V alloy

Director of the School: Ch.mo Prof. Paolo Colombo

Coordinator of the School: Ch.mo Prof. Paolo Sgarbossa

Supervisor: Ch.mo Prof. Stefania Bruschi

Ph.D. Candidate: Lizzul Lucia

Academic year: 2020-2021

Acknowledgements

I would like to thank Prof. Stefania Bruschi and Prof. Andrea Ghiotti for giving me the opportunity to enter the Ph.D. program and for trusting in my potential and capabilities. I am grateful for their assistance with my research studies, laying solid foundations for my professional development.

I sincerely thank Rachele for always pushing me to do better, for consoling me in times of difficulty and for teaching me with facts that everyone is the creator of its own destiny.

I thank Enrico for being the staple of the group, for his ability to sugar-coat the pill or bring you back down to earth in a pinch.

I thank Marco for being a great teacher, support and companion during the tests in the Kugler room.

I thank my best friend Giulia for always encourage me, for celebrating with me even the smallest goals and listening to my daily rants.

My thoughts go out to all my friends, in particular to Eva and Riccardo, which are all inspiring models, both professionally and personally.

I am grateful to my family for all of the teachings they have offered me, which have provided me with the means to get to where I am now. I know it will always be a safe haven.

I thank Alberto for always being there for me, with the passing of days and moods, with the hope that it will be forever.

Abstract

Additive manufacturing of metals is one of the most impacting processes in the fourth industrial revolution thanks to its technological, economic, and ecological competitiveness. In additive manufacturing the material is added instead of being removed, allowing for the fabrication of near-net-shape complex structures. This ensures reducing the material waste and energy consumption, as well as the lead times, resulting in manufacturing costs savings. Moreover, additive manufacturing offers a particularly high economic advantage for producing high-value-added components of difficult-to-machine metals such as titanium alloys, nickel-based superalloys, and alloyed steels. Despite the numerous advantages, among the major drawbacks to overcome there are the poor dimensional tolerance and surface finish that characterize additively manufactured parts. The surface roughness of such parts is determined by a series of interconnected input variables which, overall, lead to roughness values not less than 4 μm. To obtain a functional form and finish, machining operations are thus required. However, cutting processes can be influenced by the peculiar microstructure of additively manufactured parts. The multiple thermal phenomena taking place during the additive manufacturing process give rise to a microstructural anisotropy and phase distribution differentiating these alloys from the equivalent ones conventionally manufactured. The machinability of parts fabricated via additive manufacturing technologies has recently aroused the interest of the scientific community working on metal machining. According to the literature, it is still not possible to have a clear insight into the effect of the additive manufacturing process on machinability for a given alloy. This limit would be overcome if the mechanics of chip formation would be studied in relation to the microstructural features deriving from the additive manufacturing process. Therefore, more efforts must be put to investigate how machinability is influenced by this type of technology. The work conducted in this Ph.D. research project pointed out the influence of the microstructural anisotropy of additively manufactured Ti6Al4V titanium alloy on its machinability. The results were analyzed considering the microstructural features interaction with the cutting edge under different cutting conditions.

The first part of this thesis is focused on the evaluation of the effect of the microstructural anisotropy in different milling operations, namely slot milling with flat end mills and ball end milling. The different cutting operations were investigated at varying the build-up direction of the additively manufactured parts, and the inclination of the machined surface. The second part of the thesis deals with turning operations at varying the cutting direction and cooling condition. The surface integrity was the main parameter considered to evaluate the machinability, including surface topography, surface defects, microstructural and mechanical alterations. The chip morphology, the cutting forces, and the tool wear were considered as well.

It was found that discontinuity zones in the microstructure, typical of the alloy under examination, are the main microstructural feature affecting their machinability. They help the

material removal when favorably oriented with respect to the tool cutting edge. This leads to reduced cutting forces, increased tool life and improved surface finish.

This Ph.D. thesis aims at finding a systematic method to understand the effect of additive manufactured-induced anisotropy on machinability. The results obtained can be implemented by industries involved in the use of this technology to improve process efficiency and product quality.

Sommario

La manifattura additiva dei metalli è uno dei processi più impattanti della quarta rivoluzione industriale grazie alla sua competitività tecnologica, economica ed ecologica. Nella produzione additiva il materiale viene aggiunto invece di essere rimosso, consentendo la fabbricazione di strutture complesse *near-net-shape*. Ciò permette di ridurre gli sprechi di materiale e il consumo di energia, nonché i tempi di consegna, con conseguente risparmio sui costi di produzione. Inoltre, la produzione additiva offre un vantaggio economico rilevante per la produzione di componenti ad alto valore aggiunto in materiale metallico difficile da lavorare come le leghe di titanio, le superleghe a base nichel e gli acciai legati. Nonostante i numerosi vantaggi, tra le maggiori criticità da superare vi sono la scarsa tolleranza dimensionale e finitura superficiale che caratterizzano le parti fabbricate in modo additivo. La rugosità superficiale di tali parti è determinata da una serie di variabili di input interconnesse che, complessivamente, portano a valori di rugosità non inferiori a 4 μm. Per ottenere forme e finiture funzionali sono quindi necessarie operazioni di lavorazione di asportazione di truciolo. Tuttavia, i processi di taglio possono essere influenzati dalla peculiare microstruttura delle parti prodotte in modo additivo. I molteplici fenomeni termici che si verificano durante il processo di fabbricazione additiva danno luogo a un'anisotropia microstrutturale e a una distribuzione di fase tale da differenziare queste leghe da quelle equivalenti prodotte convenzionalmente. La lavorabilità di parti fabbricate tramite tecnologie di produzione additiva ha recentemente suscitato l'interesse della comunità scientifica che studia la lavorazione dei metalli. Da letteratura, non è ancora possibile delineare l'effetto del processo di produzione additiva sulla lavorabilità per una data lega. Tale limite verrebbe superato se si studiasse la meccanica di formazione del truciolo in relazione alle caratteristiche microstrutturali derivanti dal processo di fabbricazione additiva. Pertanto, devono essere compiuti maggiori sforzi per indagare su come la lavorabilità sia influenzata da questo tipo di tecnologia. Il lavoro svolto in questo dottorato di ricerca ha evidenziato l'influenza dell'anisotropia microstrutturale della lega di titanio Ti6Al4V prodotta in modo additivo sulla sua lavorabilità. I risultati sono stati analizzati considerando l'interazione della microstruttura della lega con il tagliente dell'utensile al variare delle condizioni di taglio.

La prima parte di questa tesi è focalizzata sulla valutazione dell'effetto dell'anisotropia microstrutturale in diverse operazioni di fresatura, ovvero scanalatura con fresa piana e finitura con fresa sferica. Le diverse operazioni di taglio sono state studiate al variare della direzione di costruzione dei pezzi fabbricati con manifattura additiva e dell'inclinazione della superficie lavorata. La seconda parte della tesi tratta delle operazioni di tornitura al variare della direzione di taglio e della tipologia di lubrorefrigerante. L'integrità superficiale è stato il parametro principalmente utilizzato per valutare la lavorabilità, includendo la topografia e i difetti superficiali, le alterazioni microstrutturali e meccaniche. Sono state considerate inoltre la morfologia del truciolo, le forze di taglio e l'usura dell'utensile.

Si è riscontrato che zone di discontinuità nella microstruttura, tipiche della lega in esame, costituiscono la principale caratteristica microstrutturale che ne influenza la lavorabilità. Esse favoriscono l'asportazione di materiale se orientate favorevolmente rispetto al tagliente dell'utensile. Ciò porta alla diminuzione delle forze di taglio, all'aumento della vita dell'utensile e al miglioramento della finitura superficiale.

Questa tesi si propone di trovare un metodo sistematico per comprendere l'effetto dell'anisotropia indotta dalla manifattura additiva sulla lavorabilità. I risultati ottenuti possono essere applicati nelle industrie che utilizzano tale tecnologia per aumentare l'efficienza del processo e la qualità del prodotto finito.

Tables of Contents

List of Tables

List of figures

List of Abbreviations and Symbols

Abbreviations

AM/AMed	Additive Manufacturing/ Additively Manufactured
AMER	North, Central, and South America
APAC	Asia Pacific
BD	Build-up Direction
BJ	Binder Jetting
BSED	Backscattered Electron Detector
CAD	Computer Aided Design
CAGR	Compound Annual Growth Rate
CD	Cutting Direction
CNC	Computer Numerical Control
COVID-19	Coronavirus Disease of 2019
DoE	Design of Experiment
EB-DED	Electron Beam Direct Energy Deposition
EBM	Electron Beam Melting
EB-PBF	Electron Beam Powder Bed Fusion
EDS	Energy-Dispersive X-Ray Spectroscopy
EMEA	Europe, Middle-East, and Africa
ETD	Everhart-Thornley Detector
FT	Face Turning
HU	Horizontal Upward
INFN	Istituto Nazionale di Fisica Nucleare
L-DED	Laser Direct Energy Deposition
LED	Light Emitting Diode
L-PBF	Laser Powder Bed Fusion
LT	Longitudinal Turning
MQL	Minimum Quantity Lubrication
PVD	Physical Vapor Deposition

R&D	Research & Development
SEM	Scanning Electron Microscope
SL	Sheet Lamination
SPD	Severe Plastic Deformation
VU	Vertical Upward
WAAM	Wire Arc Additive Manufacturing
WR	Wrought

Symbols

α	clearance angle
a_e	radial depth of cut
αGB	α phase layer at prior β grain boundaries
a_p	axial depth of cut
d	depth of cut perpendicular to the machined surface (ball end milling)
Φ	shear angle
f	feed
$Fres$	resultant cutting force
Fx, Fy, Fz	cutting force in x, y and z direction
f_z	feed per tooth
γ	rake angle
h	uncut chip thickness
$\varkappa$	registration angle
L_0	first full slot
L_f	last full slot
pf	pick feed
Ra	linear arithmetical mean height
Rt	total height of roughness profile
Sa	areal arithmetical mean height
Sdq	root mean square gradient
Sdr	developed interfacial area ratio
Sku	kurtosis

Smr1	peak material portion
Smr2	valley material portion
Spk	reduced peak height
Ssk	skewness
Str	texture aspect ratio
Svk	reduced dale height
t_r	tool rotation
vc	cutting speed

Chapter 1

Introduction

1.1 Additive manufacturing of metals: an overview

Additive Manufacturing (AM), thanks to the unique advantages it offers, represents a breakthrough in the manufacturing field. In this technology the material is added layer-by-layer instead of being removed, allowing for versatility in its applications: it allows producing complex geometries with nearly complete design freedom in a rapid design-to-manufacture cycle. AM has successfully expanded from manufacturing non-structural prototypes in the mid-1980s to structural components, extending the range of materials that can be used (from polymers to metals and ceramics).

To comprehend the origins of metal AM, it is necessary to start from those of AM with polymers, the latter being the first technology developed and whose advances are closely intertwined. The first AM system commercialization in the world dates back to 1987 and concerns the stereolithography technique for polymeric materials. This event provided wholly new possibilities to designers and engineers, acting as a push for the new and rapidly rising market of short-life items. The AM processes applied to metals developed in the 1990s and quickly deployed to the market. The first metal AM technologies were based on the direct laser sintering methods: in 1994 the German company EOS presented their prototype EOSINT M160 machine. One year later the same company introduced the EOSINT M250 machine for the production of metal tools for plastics injection molding, inaugurating the rapid tooling manufacturing [1,2]. These technologies were capable of producing metal parts from two metal powders with a liquid phase sintering process technique, leading to components with mechanical properties closer to a composite than to a metal alloy. In fact, the process consisted of one-step melting of a low melting matrix material, typically bronze or copper, around high-strength material particles, mostly steel. AM processes with high-energy fiber lasers capable of melting one component metal alloys were developed in the late 1990s: in 1999 F&S Stereolithografietechnik GmbH presented the first Laser Powder Bed Fusion (L-PBF) system in collaboration with the Fraunhofer Institute for Laser Technology, in Germany [1]. Further to the laser-based AM technologies, ARCAM, a Swedish company, patented the Electron Beam Melting (EBM) technology in 1993 and launched the first commercial technology in 2002 [3]. In the same years other AM systems, such as binder jetting and direct energy deposition, have been developed and is still growing today becoming more efficient and reliable over time.

The growth of the AM technology on a wide scale started in 2013, when patents on a polymer-based AM technology, the fused deposition modeling one, expired and low-cost printers began to enter the consumer market. This event led to a surge in stock prices of publicly-traded AM companies, and many keen industrial users and R&D departments purchased L-PBF equipment. In the years immediately following, L-PBF system producers witnessed a steady increase in sales, with the medical device industry being the main industrial driver. The biomedical industry was the first one using EBM and L-PBF technologies to manufacture dental implants, acetabular cups, and spinal cages for series production [4].

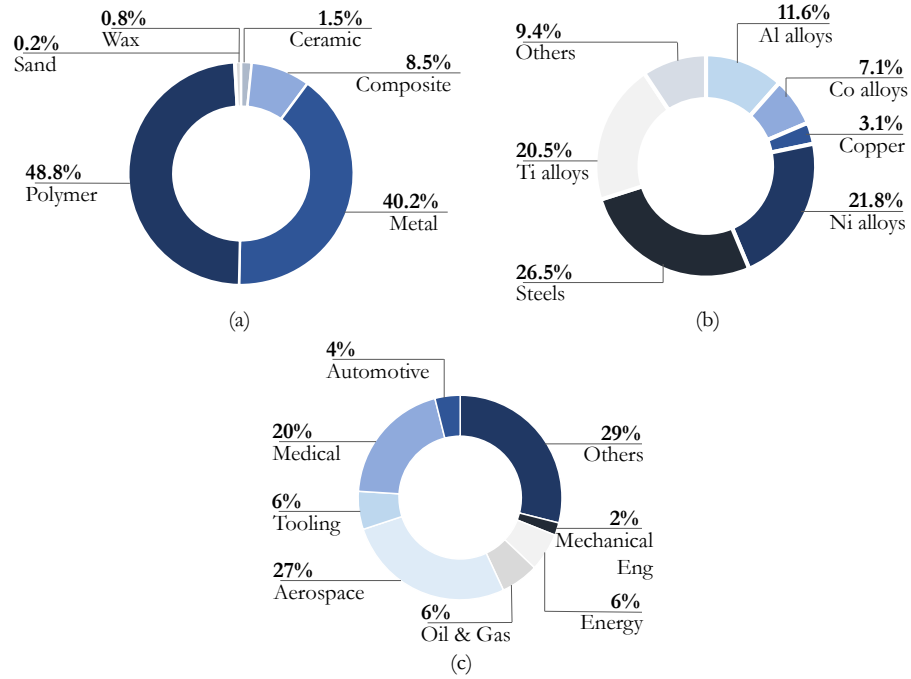

Figure 1.1: AM materials by material types in 2020 (a) [5]; available metals for AM in 2020 (b) [5]; metal AM sales revenue by industry in 2019 [6].

Nowadays metal AM is used for a wide range of industrial applications and materials (see **Figure 1.1 (b)** and **(c)**), with increasing trends in all the market categories, i.e. hardware, software, material, and research. Currently, the aerospace, turbine, and helicopter industries account for the majority of the total metal AM sales revenue, followed by the medical one. One of the primary elements driving market expansion nowadays is demand from the automotive industry [7], for the development of light-weight design to reduce fuel consumption or battery discharge, which in the second place positively affects the carbon footprint. Therefore, the majority of alloy usage in AM is driven by high-end applications. As a result, high strength and high-temperature materials such as titanium alloys, nickel-based superalloys, and alloyed steels are dominating. Powder feedstock drives the majority of the AM market size for materials, followed by wire materials, with Laser Powder Bed Fusion (L-PBF) being the most popular technique. Many of the AM early adopters were based in Germany and other European countries, as previously stated. However, market share is now more evenly divided, with both suppliers and buyers from all major industrial world areas. According to the 2024 forecast, AMER (North, Central, and South America) will grow at a rapid rate to triple the current market size, with APAC (Asia Pacific) following closely behind. The EMEA (Europe, Middle-East, and Africa) growth will be at a slower rate than the global average, however, EMEA will continue to be the most important region in terms of market size [6].

Polymeric materials are still leading the AM market thanks to the higher development level of material and part manufacturing services, resulting in a market that is more than double in size of the metal equivalent. However, the systems sales revenues of the two materials are comparable and in the last years, the number of commercially available polymer and metal materials became also equivalent (see **Figure 1.1 (a)**). The 2019 Wohlers Report [8] stated that

the revenue from metals in AM had increased by 41.9% compared to the previous year, with an overall market size valued at 2.02 billion euros. Despite the COVID-19 pandemic, the whole AM market registered an overall growth (+ 7.5%), albeit reduced compared to the previous ten years [9]. Considering the impact of COVID-19, the metal powders and the metal AM markets are expected to grow at a Compound Annual Growth Rate (CAGR) of more than 3% and 14%, respectively, during the projected period 2020-2024 [7].

From the picture just outlined, it is possible to conclude that metal AM is meant to increase its economic influence in the coming years, assuming more and more importance in the manufacturing industry in several fields, offering new opportunities for production.

1.2 The industrial problem

With AM processes devoted to metal alloys, it is possible to obtain complex structures, avoiding the design limitations that characterize the conventional manufacturing methods or the starting industrial blanks. Moreover, AM limits the need to assembly to a great extent since the process is continuous and the part is manufactured in a single shot. Some examples of design freedom are: the possibility to easily produce components with optimized internal channel geometry for fluid flows impossible to obtain with drilling operations [10], and lattice structures for reducing structural component weight or improved mechanical performance and osseointegration for biomedical implants [11]. AM allows cost reduction under several points of view: the time-to-market is shortened since it is possible to produce complex parts on-demand and *in situ*, without the need of components stocking or long shipping distances, with the possibility of a rapid re-designing of the parts which can be easily digitally modified. The AM processes offer a particularly high economic advantage for producing high-value-added components using high-performance alloys which fall into the category of difficult-to-machine metals such as titanium alloys, nickel-based superalloys, and alloyed steels. Furthermore, the material is added only where structurally needed, reducing the material usage and waste [12], allowing also to fabricate protective coatings or repair worn components [13–15]. The factors that reduce the manufacturing costs just listed are the same that label the AM as green manufacturing, helping reducing material wastage and energy consumption, lowering the carbon footprint of the entire process.

Despite its many advantages and its great technological potential, AM still has room for progress and open challenges to overcome its major drawbacks. Among them, we can find the poor surface finish and dimensional control of the fabricated parts [13,16], high residual stresses [17,18], poor microstructural control [19], and the high cost of materials and especially of the AM machines [12]. The majority of metal additively manufactured (AMed) parts include material removal operations among the post-processing steps, to guarantee that the manufactured parts fulfill the design specifications (see **Figure 1.2**). The surface roughness of AMed is determined by a series of interconnected input variables which, overall, lead to surface roughness values not less than 4 μm. Moreover, AMed components for high-end applications, such as for the aerospace and automotive industries, require high geometrical precision and surface quality, making it necessary operations of subtractive nature to obtain a functional form

and finish. This need, on the other hand, has been the driving force for the development in the mid-2000s of hybrid processes in which the direct deposition metal AM technologies have been integrated into Computer Numerical Control (CNC) machining centers [20].

However, cutting processes can be influenced by the peculiar microstructure of AMed parts. The multiple thermal phenomena taking place during the additive manufacturing process give rise to a microstructural anisotropy and phase distribution differentiating these alloys from the equivalent ones conventionally manufactured, no matter the type of alloy [21,22]. The machinability difficulties are clear from a practical point of view: unexpected cutting behaviors are on the agenda for those working with AMed alloys, showing differences not only compared to conventionally manufactured alloys but also among different pieces of the same AMed batch.

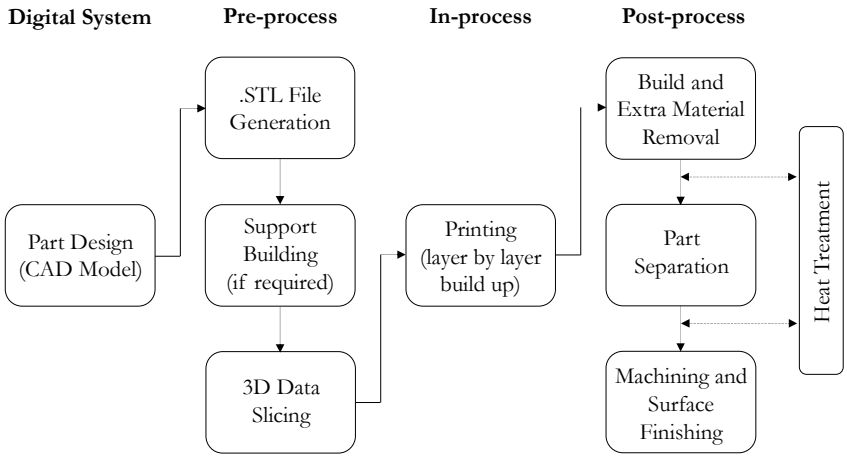

Figure 1.2: Typical workflow for metal AMed parts production. Adapted from [17,23].

1.3 The scientific relevance

The machinability of parts fabricated via AM technologies has recently aroused the interest of the scientific community working on metal machining [24–26]. In recent years, lots of effort have been put also into modeling machining operations through either analytical or Finite Element-based methods [27–29]. However, if the former give reliable results just in case of orthogonal cutting operations, which are not representative of industrial processes, the latter still need high computational costs and prevent real-time forecast for process optimization. Moreover, all the aforementioned methods cannot take into consideration the complexity of the anisotropic microstructure that characterizes AMed parts. Theoretical approaches or modeling do not always produce the desired result, and it is always preferable to clarify them using experimental data [30]. This underlines the urge for further experimental investigations when machining AMed components. According to the literature, it is still not possible to have a clear insight into the effect of the AM process on machinability for a given alloy, resulting in the unpredictability of the AMed part behavior once machined.

This problem would be overcome if the mechanics of chip formation would be studied in relation to the microstructural features deriving from the AM process itself. Therefore, more

efforts must be put to investigate how machinability is influenced by this type of technology to increase the efficiency of the entire process chain and the quality of the final products.

1.4 Research objectives

The purpose of this research work is to provide a systematic approach to understand the influence of AM-induced anisotropy on machinability that can be used by those industries that utilize AM to improve the productivity and the quality of the final products. In particular, the goal is to find a phenomenological explanation to correlate the machinability of Laser Powder Bed Fused (L-PBFed) Ti6Al4V alloy with its microstructure.

In order to achieve this goal, the experimental steps outlined below were followed:

i. Microstructural analyses: first, a minor but fundamental step, was to verify that the microstructure of L-PBFed Ti6Al4V samples fabricated for this research was compliant with what is published in the literature. The microstructure was then analyzed and studied at various build-up orientations and geometries of the samples.
ii. Machining: different cutting operations were performed on L-PBFed Ti6Al4V workpieces at changing of their build-up orientation or their surface inclination.
iii. Machinability assessment: the machinability under the different conditions above stated was analyzed considering extensively the surface integrity. The chip morphology, together with the cutting forces and the tool wear were considered as well.
iv. Phenomenological explanation: finally, a phenomenological explanation was hypothesized for the machinability results found, closely correlating them with the previously analyzed microstructural features.

1.5 Dissertation outline

The thesis is divided into five chapters and a quick preview of the contents is given as follows:

Chapter 2: Literature review. This chapter gives first a brief classification of the various metal AM methods, focusing on the L-PBF one. A rapid overview of the typical L-PBFed alloys is then presented, and the L-PBFed Ti6Al4V alloy is described in detail. The issue of the surface finish in L-PBFed is outlined. The concept of machinability is then presented and the criteria for its evaluation are described in detail, with specific comments on the Ti6Al4V machinability. Finally, the chapter reports the state of the art of the machinability of AMed parts. Conclusive remarks outline the gaps that the present research work intends to fill.

Chapter 3: Experimental procedure. This chapter describes the experimental procedure adopted for the study of the machinability of the L-PBFed Ti6Al4V alloy. First of all, the main equipment used is reported in detail, namely the AM technologies for the realization of the

samples and the machine tools for their post-processing, namely milling and turning. Then the process parameters and geometries used for the L-PBFed samples and the cutting parameters of the various machining operations are presented. Finally, the chapter reports the analyses for the characterization of the aforementioned samples.

Chapter 4: Results and discussion. This chapter illustrates in detail the machinability results, and the relative discussion, of the L-PBFed Ti6Al4V alloy both for the milling and turning operations described in Chapter 3. First, surface finish and general microstructural results of the as-built samples under examination are reported by way of example. Then, the machinability evaluations for milling operations are reported in detail, followed by the turning operations ones. At the end of each paragraph concerning a definite L-PBFed workpiece-cutting operation combination, specific conclusions are outlined.

Chapter 5: Conclusions. The specific conclusions outlined in Chapter 4 are resumed, presenting final considerations, perspectives, and future works.

Chapter 2

Literature review

This chapter gives a brief classification of the various metal AM methods, describing their working principles, and examining their main properties. Detailed information is given for the L-PBF technology. An overview on the typical AMed alloys is then presented, focusing on Ti6Al4V alloy. Then a section is devoted to the explanations of the concept of machinability. The most interesting criteria to its evaluation, i.e. tool wear, chip morphology and cutting forces, and workpiece quality, are described in detail, with specific comments on the Ti6Al4V alloy. Finally, the last paragraph describes the state of the art of the machinability of AMed parts.

2.1 Metal additive manufacturing

In this paragraph, a brief overview of the AM technologies and metal alloys are reported, focusing on the L-PBFed Ti6Al4V alloy. The issue of the AMed parts surface quality is highlighted.

2.1.1 Metal additive manufacturing technologies

To date, there are about twenty recognized metal AM systems with various fabrication techniques. The great majority of them can be classified, according to the ISO 52900 standard [31], based on:

- physical state of feedstock: melted, solid state or their combination;
- feedstock supply format: powder material, filament/wire material, sheet material;
- feeding mode: through a deposition nozzle, wire feeder, powder bed, sheet stack;
- joining method: selective deposition, selective fusion, complete fusion, friction welding;
- source of fusion (where applicable): electron beam, laser, electric arc, ultrasound;
- process category: directed energy deposition, powder bed fusion, sheet lamination.

Although some techniques have already attained a high level of maturity and expansion in the manufacturing industry, others have the potential to boost their applicability and profitability in various marker sectors. Among the latter group, it is possible to find the Binder Jetting (BJ) and Sheet Lamination (SL) processes. The BJ process consists of deposing over a loose powder metal layer a binder material through an inkjet. The latter glues the powder together where required, according to the Computer Aided Design (CAD) model. After the binder spraying, the powder platform is lowered and the process is iterated until the entire part is built. The obtained part is the so-called green, characterized by a low relative density (about 60%) which has to be heat treated in a controlled environment. The heating allows to remove the binder and to powder sintering to obtain a denser metal part. This process is characterized by considerable shrinking, degrading the dimensional precision of the part, which is the main disadvantage of this technology [32]. However, one of the key advantages of BJ is that parts can be manufactured without the use of support structures, allowing for the stacking of many pieces onto a single built platform [33]. The SL technology consists in joining together, sequentially, thin sheets until the single piece is built. The piece is then cut out in the desired

geometry by milling operation. The joining techniques of the sheets are diverse and may involve the use of adhesives, ultrasonic welding, or friction welding [34]. Since the joining process in SL is solid-state, it is possible to directly link metal components with drastically different properties, allowing for novel multi-metal structures. Among the group the most mature metal AM techniques, Powder Bed Fusion (PBF) and direct energy deposition (DED) technologies are the most common and have a wide range of applications. In PBF the powder remains static inside the build platform and is selectively joined layer-upon-layer according to a predefined two-dimensional path until obtaining the designed geometry. This technique employs a focused thermal energy source for bonding by fusion of the individual particles of powder together [35]. On the contrary, DED allows for the fabrication of metal parts by melting the material with a focused thermal energy source as it is selectively deposited on a surface. The feedstock in this case can be either in wire or powder form, coming from a wire feeder or a nozzle, respectively [36]. Although DED techniques can be used to create full pieces, they are most commonly used for fixing or adding material to existing components. In **Figure 2.1** is reported a classification of the principal metal AM technologies of the just described techniques. The reported classification differentiates the metal AM technologies based on the feeding mode, the thermal energy source used to heat the feedstock, and the feedstock supply format. Metal AM technologies based on electric arc are classified as a DED subcategory called Wire Arc Additive Manufacturing (WAAM).

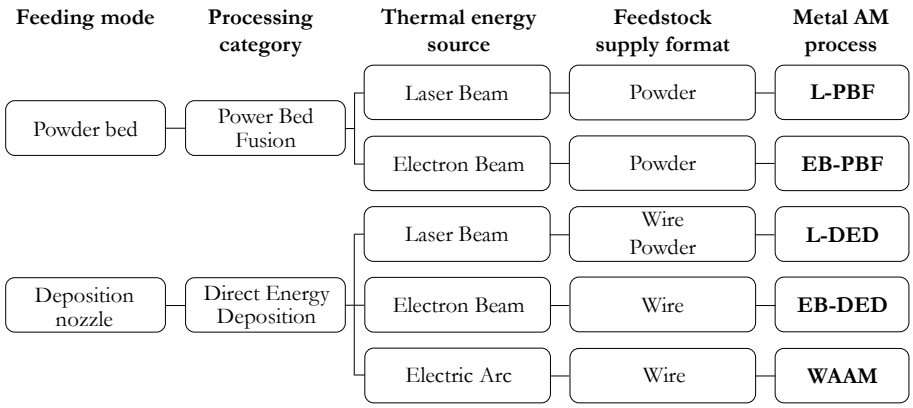

Figure 2.1: Classification of the most widespread metal AM technologies. Adapted from [31].

In **Table 2.1** the key characteristics of the three most used metal AM processes and their printed part characteristics are outlined. It is possible to note that each technology has its advantages and disadvantages, for instance, L-DED is favorable for its deposition rate but leads to components with higher surface roughness and residual stresses. On the contrary, the L-PBF allows to obtain a lower surface roughness but at the expense of the build speed. In general, PBF technologies can produce parts with greater complexity than DED ones, with less powder waste and easier recycling of unmelted powder [37]. For what concerns the L-PBF technology, a laser beam is used as the source of fusion to selectively melt the powder which then solidifies one layer after another. The laser beam is directed and moved in a controlled manner through reflective mirrors according to the slicing path of the digital model. The entire process occurs in an inert atmosphere due to the high reactivity of metal powders. In EB-PBF the source of thermal energy is an electron beam rather than a laser, which is focused and

deflected thanks to electromagnetic lenses instead of mirrors. The operating principle in the two cases is similar, however, the use of the electron beam makes it necessary to work in controlled vacuum conditions, thus raising the complexity of the equipment and therefore its cost [33]. Furthermore, with this technology, the powder bed must be preheated to approximately half of the melting temperature of the powder employed, to avoid the so-called powder pushed away phenomenon, due to the generation of electrostatic charging of powder particles [38]. However, the preheating of the chamber can be seen as an advantage as it allows to obtain parts with low residual stresses (see **Table 2.1**), often avoiding the need for post-process heat treatment.

Table 2.1: Main characteristics of the three most common metal AM technologies.

	Powder L-DED	L-PBF	EB-PBF	Ref.
Build speed (cm^3/h)	100 – 300	25 – 50	50 – 100	[14,39]
Cooling rate (K/s)	$< 10^3$	$10^3 – 10^8$	$10^3 – 10^4$	[13,40]
Roughness *Sa* (μm)	10 – 70	5 – 20	25 – 50	[16,41–44]
Residual stresses (MPa)	200 – 700	100 – 500	10 – 80	[45–47]

2.1.2 Focus on L-PBF technology

L-PBF is one of the first developed metal AM technologies, as reported in Chapter 1, and the leading technology in both the academic and industrial world. There is a substantial amount of literature devoted to L-PBFed metals characterization considering both under microscopic and macroscopic properties of a wide range of alloys [35]. The constant improvement of the system by manufacturers allows for faster build times and lower surface roughness as compared to competing metal AM technologies. In recent years, this technology has undergone strong development, as also evidenced by the large number of companies that have invested in it (over 60 system suppliers), making this type of technology the one with the highest industrialization index [6]. As previously mentioned, L-PBF is based on the laser-induced melting of a powder feedstock. **Figure 2.2** shows a schematization of a general L-PBF system. The process occurs in a working chamber where a substrate plate is fixed on the build platform. The metal powder coming from a supply chamber is spread on the substrate through a leveling system (recoater) at a fixed layer thickness. The recoater can be of several types, such as a roller, a blade, or a brush. The energy source to bind the metal powder is provided by a laser beam, which is directed on the powder bed to selectively melt the powder. The common laser beams used in L-PBF are ytterbium-doped (Yb-fiber), neodymium-doped yttrium aluminum garnet (Nd:YAG) and carbon dioxide (CO_2) lasers. They principally differ for their wavelength: about 1070 nm for Yb-fiber and Nd:YAG and from 9.0 to 11.0 μm for CO_2 lasers. For an efficient powder-laser interaction, a high material absorption at the laser wavelength is desired. Therefore, in L-PBF of metal powders the Yb-fiber and Nd:YAG lasers are preferred because metal particles usually have higher absorptivity at shorter optical wavelengths [48]. Standard L-PBF systems have a laser source coupled to precision optics, however, there are currently many systems that use more than one laser beam for higher productivity.

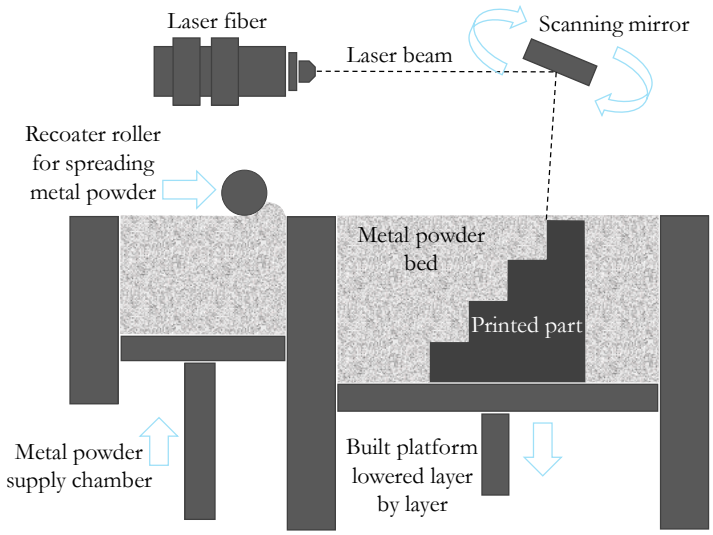

Figure 2.2: Schematic representation of a typical L-PBF system.

A moving mirror system is often used to deflect and guide the laser beam. There are also machine systems in which the laser is moved via a multi-axis gantry which allows for a cost reduction. Once the selective fusion of a layer is completed, the build platform is lowered by the same amount as the set layer thickness, and new powder is spread over the surface. The aforementioned method is repeated until the whole component is formed and the unexposed powder that remained loose is recycled. Due to the metal powder reactivity, the process is carried out in a protected environment of argon or nitrogen, depending on the metal reactivity grade [49]. The build chamber is filled with inert gases before the process begins to minimize the oxygen concentration (< 0.3%). The flow of inert gas is then maintained throughout the process, both to prevent oxidation of the powders and to remove excess powders from the melting zone. Alternatively, L-PBF systems with a vacuum chamber are available to reduce powder oxidation [1].

The main process parameters of L-PBF and their effect on the printed part will be described below. It should be borne in mind that it is not always possible to discern the effect of a single parameter as they contribute synergistically to define the quality of the final component. In fact, linear or volumetric energy densities are often used to describe an AM process and compare studies. The equation for linear energy density is:

$$E_l = \frac{P}{v} \quad (J/mm) \qquad \text{Equation 1}$$

where P is the laser power (W) and v is the laser scanning speed (mm/s). The equation for the volumetric energy density is:

$$E_v = \frac{P}{v \cdot t \cdot h} \quad (J/mm^3) \qquad \text{Equation 2}$$

where t is the layer thickness (mm) and h the scan hatch spacing (mm).

The following are the fundamental process parameters of L-PBF and their principal effect on the printed part:

- Laser power: the fundamental parameter defining a L-PBF machine is its laser unit. Laser beam powers used in this technology range from 50 to 1000 W [13], depending on the melting temperature of the metal: the higher the melting temperature, the higher the laser power.
- Laser spot: in L-PBF machines the laser spot can be fixed or variable. Generally, the spot size ranges from 30 to 180 μm [16]. Increasing the laser spot size can help to accelerate the AM process, however, it reduces the energy density of the process. If the latter falls below a specific threshold, the complete fusion of the powder may be hindered [49].
- Scanning speed: typical scanning speeds in L-PBF processes vary from 10 to 1000 mm/s [13]. By increasing the scanning speed, the other parameters being equal, it is possible to accelerate the AM process, however, the interaction time is decreased. This condition may lead to an insufficient energy density thus a lower molten pool hindering a complete fusion of the powder [49].
- Layer thickness: the layer thickness in L-PBF ranges from 20 to 100 μm [13]. A thicker layer accelerates the printing process, but it can also lead to partial melting of the deposit [49].
- Scan hatch spacing: the hatch spacing is defined as the distance between two adjacent laser passes (see **Figure 2.3**). Its value should be designed to obtain appropriate melt pools overlapping to prevent the creation of porosity in the built part. A poor overlapping causes an incomplete fusion of two successive melt pools, while an excessive overlapping diminishes the melt pool depth or penetration causing poor bonding between layers [50]. Usually, a 25% scan overlap is considered optimal in L-PBF processes [49].
- Scanning strategy: the scanning strategy defines the pattern with which the layers are build up. The pattern can vary as a function of the laser scans sequence and directions on the same layer and among successive layers. The scanning strategy influences the cooling time of fused layers as well as the overall properties of the L-PBFed part. The island (or chessboard) scanning strategy is often preferred since it allows reducing the residual thermal stresses by lowering the cooling rate, thus preventing cracks formation [50].

The ideal process parameters vary based on the metal alloy, type of powder and L-PBF system properties and are relate one to another. The choice of the optimal process parameters to obtain fully dense part with minimal thermal distortion can be supported by the so-called process parameters windows (see **Figure 2.4**).

The L-PBF is an extremely complex process in which multiple thermo-fluid dynamic phenomena are involved. When the laser beam scans the deposited powder layer to melt the powder, large thermal gradients arise. The fused powder forms the so-called melting pool, which travels among the solid particles as the laser beam moves, achieving the equilibrium state

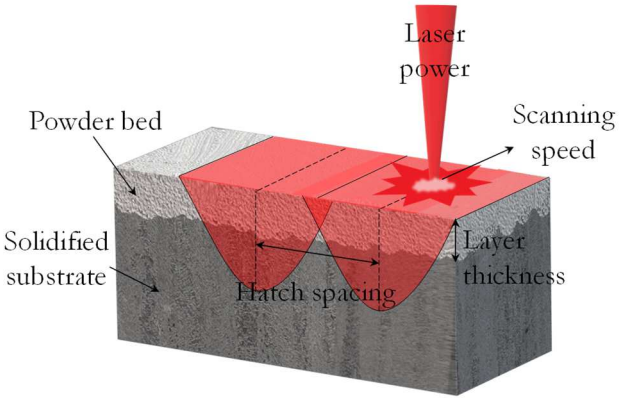

Figure 2.3: Process parameters of L-PBF.

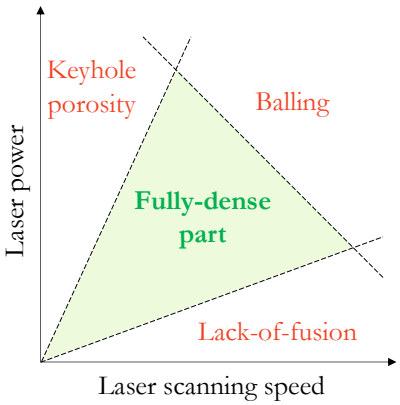

Figure 2.4: Generical diagram of process parameter influence on porosity.

and exchanging heat with the loose and pre-solidified powder, as well as the surrounding environment. When the temperature of the melt pool decreases, the molten material solidifies. Differences in viscosity throughout the melt pool caused by changes in viscosity between the liquidus and solidus temperatures can have a significant impact on the form of the tracks and the subsequent part quality [51]. In particular, the stability of the melt pool greatly influences the surface roughness and density of the printed part. Rapid cooling rates can lead to the formation of segregation, and large temperature gradients to high residual stresses which, overall, worsen the mechanical properties of the L-PBFed part. Among the physical phenomena impacting the evolution of the melt pool, there are heat conduction, convection, gravity, and capillary forces, melting and solidification. A minor effect is attributed to solidification shrinkage, Marangoni effect, and radiation [51].

Among the benefits of L-PBF technology, there are [33,52,53]: (i) the possibility to manufacture complex geometries with support-free overhangs up to 45°, with the ability to achieve up to 10° overhangs, (ii) lattice structures are feasible and easy to realize, (iii) the ability to produce hollow bodies and high-resolution features, (iv) efficient use of materials since the unmelted powder can be easily recovered and recycled, (v) materials flexibility, (vi) fine microstructures are achieved due to high solidification rates, (vii) good dimensional control since no negligible shrinkage occurs, and (viii) mass customization.

The main L-PBF process drawbacks are [53–55]: (i) challenging removal of powder from small size channels, (ii) high equipment cost, (iii) absence of on-line quality control, (iv) significant residual stresses, (v) high surface roughness, (vi) anisotropic properties due to anisotropic microstructure.

Due to points (iv) and (v), the parts obtained with L-PBF, and in general with all metal AM processes, require post-processing. Usually, heat treatments are carried out to reduce thermal stresses and stabilize the microstructure, besides closing the minor pores. To ameliorate the surface quality of functional surfaces, finishing machining operations are conducted. The generation of surfaces in L-PBF will be covered in detail later, in Section 2.1.5. The metal powders used in L-PBF processes are discussed first, followed by the primary metals in L-PBF and their properties. The aim is to better understand the relationships between the L-PBF induced microstructure and mechanical properties of L-PBFed parts. A more detailed description will concern the Ti6Al4V titanium alloy, which is the material under consideration in this research work.

2.1.3 Metal alloys in L-PBF and their properties

Metals that can be processed by L-PBF should fulfill two major requirements: i) good weldability and ii) availability in powder form. The first condition is necessary to avoid solidification cracking which is detrimental for the soundness of the printed component [22] and should be avoided. As previously mentioned, the optimal L-PBF process parameters also depend on the properties of the metal powder. Both the chemical and physical properties of the metal powder affect the energy density involved in the process. In fact, those properties strongly influence the powder absorptance, i.e. the ratio of the absorbed to the incident radiant flux. Furthermore, heat conductivity, heat capacity, and latent heat are the main material properties influencing the L-PBF process and output. Finally, granulometry and particle size distribution of the metal powder must also be considered as they alter the absorbance depending on the apparent density of the powder [56]. Usually, lower particle size requires lower laser energy to achieve an optimal fusion of the powder and thus denser parts. High quality parts such as higher hardness, mechanical properties, and better surface finish can be achieved using powders with good flowability which is improved by a narrow particle size distribution [42,57]. Regardless of the kind of laser, powder materials have higher absorptance than corresponding bulk materials.

Typically, fine metal powder in the 5 - 50 μm size range with good quality and spherical shape are preferred in L-PBF processes. Good quality powders are characterized by low levels of contaminants, reduced surface oxidation and good flowability. This allows obtaining better part quality with low porosity, internal stresses, part distortion, and surface roughness [58]. The quality of the powder is determined mainly by the production process. Hence gas and plasma atomized powders are widely used. In the first case, the molten alloy is atomized by an argon or nitrogen flow at high pressures [59]; in the second example, a metal wire is fed into the apex of a gas plasma flow, where it is melted and atomized all at once [60]. The use of plasma-based technology is particularly performing for the production of powders of reactive and high melting point materials such as titanium, nickel, molybdenum and their alloys. A more

sophisticated plasma-based powder production method is the so-called plasma rotating electrode process in which the metal source is a rotating bar instead of a wire [61]. The molten metal is centrifugally ejected forming droplets that solidify before reaching the walls of the atomization chamber. This process results in fine powders of high purity, with fully spherical shape and smooth surfaces. Moreover, the particle size distribution is highly uniform, promoting homogenous melting during the L-PBF process. The interlayer bonding is thus favored, increasing at the same time the mechanical properties and surface finish of the printed part. On the contrary, gas atomized particles present spherical morphology but with satellites on the surface which reduce the flowability and degrade the final part quality. Additionally, such powders often contain entrapped gas bubbles leading to porosity in the component [62]. The quality of the powders comes at the expense of their cost; therefore, the raw materials must be selected according to the quality of the L-PBFed piece to be obtained.

As a consequence of a highly concentrated heat source in a short period of time, high cooling rates and thermal gradients characterize the L-PBF process. Therefore, fine grains, non-equilibrium microstructures and directional solidification develop in the printed part, leading to anisotropic microstructures with highly possible metallurgical defects [63]. In particular, long grains grow along the build-up direction, which corresponds to the greatest thermal gradient direction during the L-PBF process. Metallurgical defects can include porosities of various types that form inside the printed component. The porosity is usually classified as gas pores, lack-of-fusion porosity, or cracking [64,65]. The first arise when external gas is trapped in the melt and does not reach the surface before solidification (exogenous porosity), or when low melting point constituents within the alloy vaporize during melting (endogenous porosity). In both cases the pore assumes a rounded shape with dimensions less than 100 μm. On the contrary, keyhole porosities, deriving from the rapid solidification of the molten metal hindering the complete filling of the gap, are irregular and with dimensions higher than 100 μm. The formation of cracks is, instead, related to the thermal stresses developing during and after the L-PBF process. This makes clear that metals fabricated by L-PBF present structures, microstructures, and phases arrangement that greatly diverge from their conventionally manufactured counterparts (for instance, cast or wrought components). Because of such differences in microstructure and surface finish, the mechanical behavior of L-PBFed metals may differ significantly from that of traditionally manufactured metals [66].

Aluminum alloys

Aluminum alloys are among the lightweight alloys most commonly used in L-PBF processes and AlSi10Mg is the most studied, followed by the AlSi12. The L-PBFed AlSi10Mg parts exhibit better mechanical properties, such as higher ultimate tensile strength, ductility, hardness and impact energy, than the equivalent cast alloy [67,68]. This is due to the very fine microstructure and fine Si precipitates that form in L-PBFed parts as a result of the high solidification rates [69]. Moreover, the majority of studies report anisotropic mechanical behavior related to the microstructural anisotropy which shows grains alignment with the build direction [67,68]. The main issue related to aluminum alloys processed via L-PBF is their high reactivity with oxygen, even at low temperatures. The oxide films forming on the molten alloy during the process reduces the wettability preventing proper melting. Moreover, oxides remain trapped in the molten pool during solidification, causing weak spots in the final component.

Therefore, when treating with aluminum alloys, the conditions of the surrounding environment are especially critical to attain the desired part quality. Finally, aluminum powders are pretty light and with poor flowability, making it difficult to spread a thin powder layer.

Ferrous alloys

The most common and mature ferrous alloys made by L-PBF are the AISI H13 tool steel and the M300 maraging steel [70]. The studies on the L-PBFed H13 steel reveals that it is composed mainly of martensite and retained austenite with a directional growth of the microstructural texture as columnar grains develop along the build-up direction, which corresponds to the greatest heat gradient direction during the AM process [71,72]. Overall, the microstructure is mixed type showing, besides the columnar grains, also coarse and fine cellular grains. Despite the obvious microstructural anisotropy of H13 tool steel made by L-PBF, studies on the anisotropic mechanical behavior are uncommon. A recent study compared the mechanical behavior of L-PBFed H13 with the conventionally manufactured counterpart, i.e. forged quenched H13 tool steel [73]. This work reported that the microhardness and tensile strength values of the two steels were comparable. However, the L-PBFed H13 steel reported an elongation three times greater than that of the conventionally manufactured one. The high residual stress and porosity of the L-PBFed H13 steel resulted in slightly lower impact energy than that of the forged quenched steel.

For what concerns the L-PBFed M300 maraging steel, it consists principally of martensite in their as-built state, with traces of austenite phase [74]. Microstructural anisotropy characterizes such parts, showing melt tracks on the top surface with cellular microstructure and arcuate melt tracks with fine columnar and/or dendritic grains microstructure on the side surface [25]. This reflects on their mechanical properties: the tensile strength and elongation at fracture are lower when the loading direction is parallel to the build-up one than when it is perpendicular to it [74]. Usually, the as-built L-PBFed M300 parts report greater strength and hardness than conventionally manufactured ones.

Among the austenitic stainless steels, the most studied are the AISI type 316 stainless steel, and its low carbon variant AISI 316L. Generally, the as-built L-PBFed austenitic stainless steels outperform their commonly made counterparts in terms of mechanical characteristics. Higher ultimate tensile strength, yield strength, and hardness are all advantages, but they come at the expense of ductility. The improved mechanical properties in L-PBFed parts are ascribed to a combined effect of grains refinement and high dislocation density due to rapid solidification. These characteristics also cause the degradation of the elongation at fracture, together with the presence of internal defects such as sharp-edged pores, which act as stress concentration sites under loading [75,76]. Due to the rapid cooling rates of L-PBF, such alloys present both γ-austenite and δ-ferrite phases rather than the fully austenitic microstructure of the conventionally processed ones [76]. Moreover, the microstructure of these materials is anisotropic with elongated grains and dendrites directed along the build-up direction of the part, as for the other ferrous alloys above reported. As a result, there is a minor anisotropy in the mechanical properties, with tensile strengths in the longitudinal direction equivalent or greater than those in the transverse direction [13].

Nickel-based alloys

Nickel-based alloys are among the most studied and developed metallic alloys for the L-PBF process. Most of the studies are focused on Inconel alloys, a family of austenitic nickel-chromium-based superalloys with excellent resistance to mechanical and thermal stresses even in corrosive environments. This makes them particularly suitable for building components for the aerospace industry such as gas turbine blades and jet engines. The common nickel-based alloys fabricated via L-PBF are Inconel 625, Inconel 718, Hastelloy X, Invar 36, Nimonic 263 [22,77]. All these alloys present columnar grains oriented along the build-up direction due to the peculiar thermal history of the L-PBF process, but no clear trend was found among the anisotropy and the mechanical properties. The ductility can be either equal or higher when the loading direction is parallel to the build-up direction than when is perpendicular to it [13,78]. The ductility improvement in the parallel direction of loading is attributed to the failure mode occurring which is shearing through columnar grains rather than intergranular failure. On the contrary, the latter prevails in perpendicular loading, leading to improved strengths but lower elongations [79]. In general, the ultimate tensile strength of such alloys is higher than the corresponding cast alloy [77]. Moreover, subsequent laser scans cause strong thermal gradients leading to differential contractions in the L-PBFed parts, thus to high plastic deformation, i.e. to high dislocation density. This results in higher microhardness values of L-PBFed alloys than in the cast one [78].

Titanium and its alloys

Titanium is an optimal target material for L-PBF since it allows for cost savings compared to conventional manufacturing methods. Indeed, with L-PBF, the need for extensive machining operations is avoided, which are costly and problematic for titanium, a well-known difficult-to-cut metal. Moreover, thanks to the strong appeal for aerospace and biomedical devices industries, titanium and its alloys have been extensively researched in the AM sector. Commercially pure titanium (α-type titanium alloy) is widely utilized as metal or biomedical implants. The microstructure of commercially pure titanium processed by L-PBF can vary from plate-like α grains to acicular martensitic α' grains obtained, respectively, at lower and higher scanning speed, being the other process parameters constant. A low scanning speed allows for the complete allotropic transformation of β phase to the α one during solidification, whilst at a higher scanning speed the temperature gradients increase leading to the presence of the metastable martensitic phase in the final L-PBFed part. The mechanical properties of L-PBFed commercially pure titanium are greater than the same material conventionally processed, showing enhanced yield and ultimate tensile strengths, wear resistance, compressive properties, and microhardness [80]. These improvements are attributed to the grain refinement by the AM process and to the presence of the acicular α' grains and are all desirable aspects for biomedical implants purposes. The scenario of titanium alloys fabricated via L-PBF, and in general, via AM, is 95% dominated by the Ti6Al4V alloy because of its excellent strength-to-weight ratio [6,13]. Other titanium alloys processed via L-PBF are quite rare, among these, there are the α - β titanium alloy Ti6Al7Nb [81] and the β titanium alloy Ti24Nb4Zr8Sn [82]. The former exhibits an α' martensitic microstructure in as-built conditions, with mechanical properties better than the same wrought alloy, while the latter presents comparable or lower

properties compared to the same alloy processed by hot rolling or forging. In fact, due to the high oxygen content in the starting powders, L-PBFed Ti24Nb4Zr8Sn components do not exhibit the beneficial superelastic characteristic of the conventionally manufactured counterparts.

2.1.4 Focus on Ti6Al4V alloy in L-PBF

Ti6Al4V alloy is the most utilized titanium alloy in the world. More than 80% of its use belongs only to the aerospace industry. Another extensive application of this alloy is intended for medical prosthetics [83]. The marine, chemical and automotive industries employ it as well, even if in smaller amounts. Ti6Al4V offers outstanding resistance to medium-low temperatures but has a great specific resistance and stability also at temperatures above 883 °C, besides a good corrosion resistance. The chemical composition of the Ti6Al4V alloy grade 5 is reported in the table below.

Table 2.2: Chemical composition (weight %) of the Ti6Al4V alloy grade 5 according to [84].

Al	V	Fe	O	C	N	H	Ti
5.50–6.75	3.5–4.5	<0.30	<0.20	<0.08	<0.05	<0.015	Bal.

In this paragraph, the microstructure of the Ti6Al4V alloy induced by the L-PBF process and the resulting mechanical properties will be described in detail and compared to that of a conventionally manufactured one. Both the as-built and post heat treatment conditions will be considered.

Conventionally manufactured Ti6Al4V alloy

Since titanium may undergo allotropic transformations, microstructure in α - β alloys can be considerably modified by heat treatments and by the processing as well. The phase diagram of Ti6Al4V alloy is reported in **Figure 2.5**, showing the phase changes occurring at different temperatures. The main physical-thermal and mechanical properties of the wrought Ti6Al4V alloy grade 5 are reported in **Table 2.3** and **Table 2.4**, respectively.

Table 2.3: Main physical and thermal properties of the wrought Ti6Al4V alloy grade 5 [85].

Density	Thermal conductivity	Melting point	Beta transus
4.43 g/cm^3	6.7 W/mK	1604 °C (*solidus*) – 1660 °C (*liquidus*)	980 °C

Table 2.4: Main mechanical properties of the wrought Ti6Al4V alloy grade 5 [85].

Ultimate tensile strength	Yield tensile strength	Elongation at break	Young modulus
950 MPa	880 MPa	14%	113.8 GPa

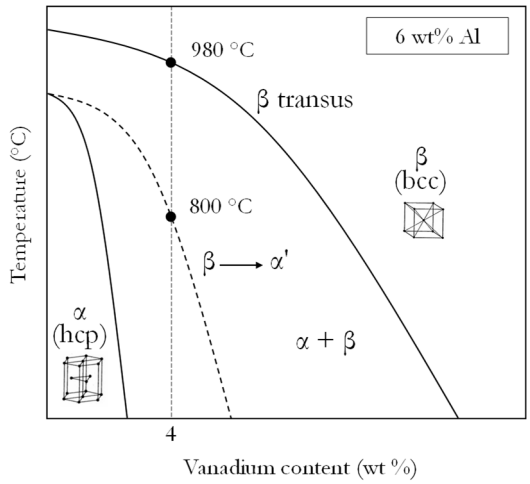

Figure 2.5: Phase diagram of Ti6Al4V alloy.

The typical microstructures that can be obtained in Ti6Al4V alloy conventionally manufactured are lamellar, equiaxed, and bimodal [83], as shown in **Figure 2.6**.

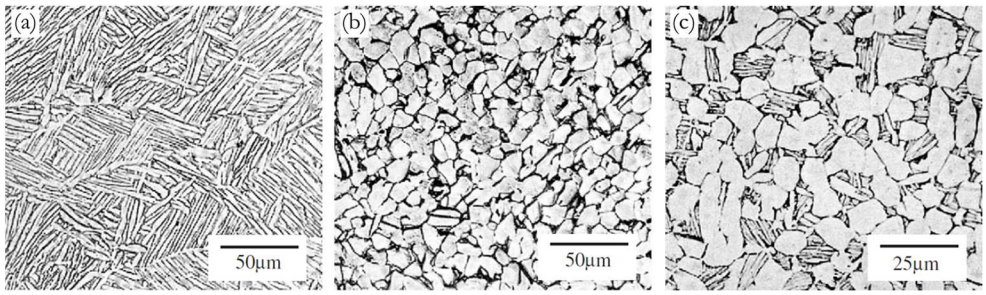

Figure 2.6: Typical microstructures of Ti6Al4V alloy conventionally manufactured; (a) lamellar, (b) equiaxed, and (c) bimodal. Adapted from [83].

The lamellar structure can be obtained by air cooling (annealing) starting above the β transus, which is the minimum temperature at which the β phase is the only phase present. With this heat treatment is possible to produce the so-called Widmanstätten structure: α plates, transformed by the β matrix through nucleation and growth, separated by the β phase. The size of the platelets depends on the cooling rate, the greater the rate, the finer the microstructure. Extremely fast cooling will lead to a martensitic (diffusionless) transformation. Unlike the martensitic transformation in steels, in this case, the increase in hardness and strength is minor. Furthermore, in titanium alloys, there are two forms of martensitic structure depending on the content of alloying elements. For reduced contents of β-stabilizing elements, the crystal lattice becomes hexagonal and the martensite is defined as α'. Whereas for high solute content, martensite has an orthorhombic crystal structure and is called α" [86]. The bimodal microstructure (or duplex microstructure) can be obtained by solution treatment below β transus, cooling in air, and a final aging treatment. This kind of structure consists of equiaxed grains of the primary α phase and a fine lamellar structure of the secondary α phase. The equiaxed structure can be obtained similarly to the bimodal one, the only process parameter to be modified is the rate of cooling from the temperature at which recrystallization

annealing is performed. If this is sufficiently slow, there is no formation of a lamellar structure among primary α phase grains, but they tend to enlarge.

Macro and microstructure of L-PBFed Ti6Al4V alloy

As previously stated, L-PBF is characterized by very rapid solidification. The high temperature gradients generated lead to macrostructures and microstructures which differ from the ones of the conventionally manufactured alloy just presented.

The as-built Ti6Al4V L-PBFed parts present on the side cross-sections, a macrostructure characterized by elongated grains, vertically developed across several layers with lengths up to several millimeters [14], as reported in **Figure 2.8 (a)**. Since the Ti6Al4V components solidify first as β phase (see **Figure 2.5**), the columnar grains which form along the build-up direction correspond to the cubic β grains, whose preferential crystal growth direction is the <100> one [87]. The latter aligns along the largest heat transfer direction within a melt pool, which coincides with the L-PBF build-up direction [88]. The vertical heat flux of the laser beam and the consequent high thermal gradients allows for the β grains expansion over many layers during the melting phase, according to the solidification map of the Ti6Al4V alloy illustrated in **Figure 2.7**. In fact, the as-solidified macrostructure of titanium components produced by L-PBF is the consequence of a conflict between the nucleation of new equiaxed grains and the epitaxial development of long columnar grains from the bottom of the melting pool on partially fused grains [89]. Moreover, the partial remelting of the previously deposited layers, in addition to acting as a densification factor of the L-PBFed part, allows for the elimination of the nucleation barrier for solidification and the development of such columnar grains across the layers [87]. On the top cross-section of the L-PBFed parts, the pattern of the chosen scanning strategy is often visible [19,90].

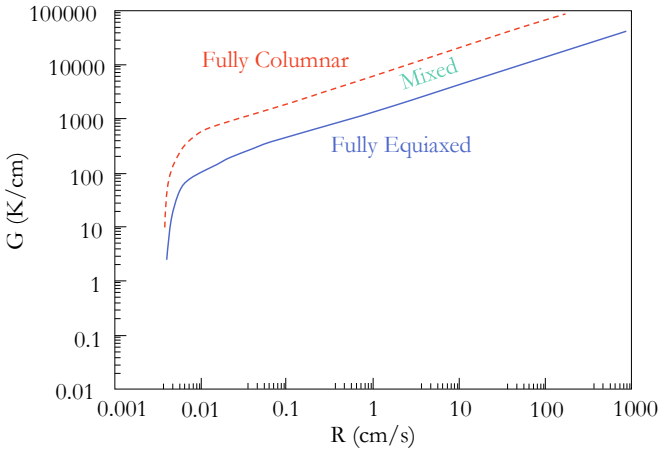

Figure 2.7: Solidification map of Ti6Al4V alloy. For low values of solidification rate velocity (R) and high values of thermal gradient (G), a fully columnar structure is formed, while a fully equiaxed structure is observed in opposite case (high R and low G). Adapted from [91].

Because of the extremely high cooling rates of such process, the cubic β phase completely converts into hexagonally packed α'-martensite when cooled (α' develops for cooling rates higher than 410 °C/s) [19]. The newly developed martensitic phase has a distinct crystallographic connection with the β phase according to a specific Burgers relation:

$(100)_{bcc}//(0001)_{hcp}$ and $\langle 1\bar{1}1\rangle_{bcc}$ $\langle 11\bar{2}0\rangle_{hcp}$. In the case of the L-PBFed Ti6Al4V alloy, this determines the preferred growth orientation of the martensitic needles at an inclination of around 40° - 45° with respect to the build-up direction with a herringbone pattern [22], as visible in the zoomed box of **Figure 2.8 (a)**.

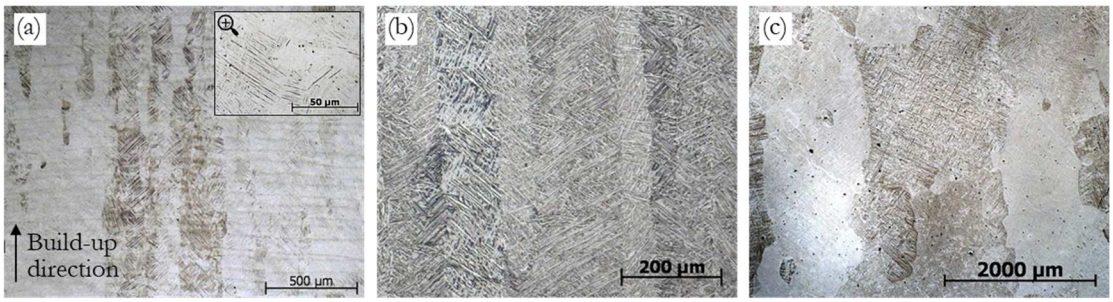

Figure 2.8: Typical microstructure of the L-PBFed Ti6Al4V alloy in as-build condition (a), after high-temperature subtransus heat treatment (b), and after high-temperature supertransus heat treatment (c). Adapted from [19].

Thanks to the presence of the fine α' grains, the ultimate tensile strength (up to 1206 MPa) and the yield strength (up to 1166 MPa) of as-built L-PBFed Ti6Al4V are in average 20-30% greater than wrought and cast equivalent alloy, whilst the ductility has a marked opposite trend and can be up to 80% lower in the case of the L-PBFed alloy [13,92]. The microstructural anisotropy above described is reflected on the mechanical properties of the L-PBFed Ti6Al4V: the ductility when the loading direction is perpendicular to the build-up direction can be up to five times higher than the ductility when the load is applied in the parallel direction to the build-up one [92]. This difference in ductility in the as-built condition is principally related to the defects present in the bulk, in particular to the lack of fusion pores between two successive layers. This kind of defect is very common and concur with the microstructural anisotropy since they are aligned along the layers, perpendicularly to the build-up direction. When loading the specimens parallel to the build-up direction, such defects are subjected to opening as in the case of mode I load in fracture mechanics. This situation is particularly critical since the extremities of such pores are sharp and act as stress concentration sites. When loading perpendicularly to the build-up direction, such porosities tend to close and result less detrimental than in the other case as shown by experimental tests.

Heat treatments for L-PBFed Ti6Al4V alloy

Usually, heat treatments are carried out on the as-built parts in order to stabilize the microstructure, relieve the thermal stresses, reduce the porosities, and improve the mechanical properties [19,92]. As reported in the ASTM F3301 standard [93], the post-processing heat treatments to be carried out on Ti6Al4V alloys can be of various typologies according to the specific requirements of in-service properties of the printed part. In general, treatments can be divided into low-temperature and high-temperature strategies. The heat treatments devoted to the only scope of reducing thermal stresses are carried out at lower temperatures, among 700 °C and 800 °C (typically 730 °C for 2 hours) [92], ideal for parts requiring great dimensional stability while maintaining appropriate mechanical properties. At such temperatures the microstructural modifications are marginal and only a partial transformation of the α' phase

into the stable α and β phases occurs. A typical microstructure of L-PBFed Ti6Al4V subjected to such treatment is shown in **Figure 2.9 (a)**. This results in a slight microhardness decrease, as well as a decrease by 15% of ultimate and yield strengths, but still within the acceptance range for aeronautical applications. A slight improvement in ductility is obtained even if the strong anisotropy is preserved [92,94]. The presence of the retained β phase, albeit in small quantities, at the grain boundaries of the α lamellae, allows for the slip transfer at the α-β interface, explaining the increase in ductility [94].

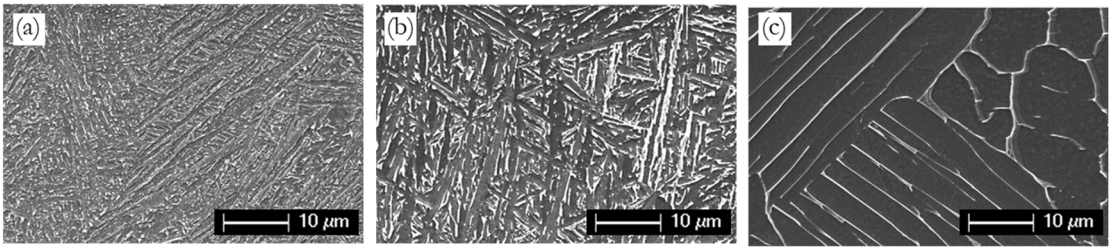

Figure 2.9: Typical microstructure at high magnification of the L-PBFed Ti6Al4V alloy after low-temperature heat treatment (a), after high-temperature subtransus heat treatment (b), and after high-temperature supertransus heat treatment (c). Dark zones are α phase, the dark zones are β phase. Adapted from [19].

High-temperatures strategies allow for both stress relieving and microstructural stabilization. They consist of solution treatments, eventually followed by tempering treatment to change the volume fraction, chemical composition, size and morphology of the strengthening phases. This allows obtaining the best mechanical properties of the L-PBFed piece, making it suitable for the majority of the industrial applications. The solution treatments are usually carried out below the β transus (between 900 °C and 980 °C) to avoid excessive grain growth and thus a deterioration of mechanical properties [19,92]. With such treatment, the as-fabricated martensitic phase α' gradually decomposes into a stable microstructure constituted of α and β phases (see **Figure 2.9 (b)**). However, the subtransus solution treatment does not allow for grain morphological alterations and the grain boundaries and shape of the prior β grains remain unvaried. After the heat treatment, within the prior β grains the previous acicular martensitic grains are transformed into colonies of α phase lamellae with β phase at their boundaries, maintaining the 40°- 45° orientation with respect to the build-up direction as visible in **Figure 2.8 (b)** (α and β phases are in light and dark respectively). Hence, the anisotropic microstructure still dominates even if the porosity is reduced. Along some prior β grains boundaries, continuous α phase layers, the so-called αGBs reported in **Figure 2.10**, may form upon the heat treatment, which is symptomatic of the diffusive nature of the β-α transformation [88]. The microstructure of subtransus heat-treated L-PBFed Ti6Al4V becomes therefore comparable with the one obtained after EB-PBF process [88,95]. The size of the α colonies is limited to that of the prior β grains and the size of the α phase lamellae can be varied as the residence time inside the furnace varies. As the size of these grains varies, the mechanical properties of the piece are affected. A study by Sharma et al. [96] identified a direct correlation between the prior β grains width and the one of the α lamellae at their inside, i.e. high β grains width corresponds to high α lamellae width. The latter was found to be well correlated to the microhardness values through the Hall-Petch relation, concluding that the α lamellae width controls the mechanical properties of the AMed part.

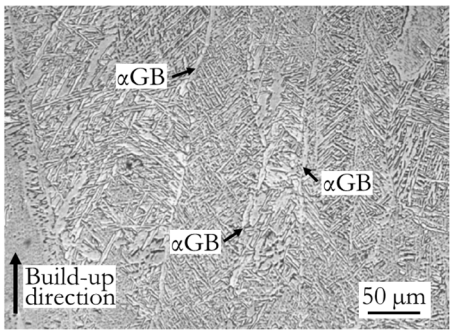

Figure 2.10: Microstructure of the AMed Ti6Al4V alloy reporting αGBs along the boundaries of the prior β grains. Adapted from [88].

The described anisotropy of the L-PBFed parts reflects on their mechanical properties. Overall, this kind of heat treatment allows for a great increase in ductility with respect to the as-built part, keeping the ultimate tensile and the yield strengths higher than the conventionally manufactured counterparts, even if lower than the as-built condition. The anisotropy in mechanical properties is maintained even if reduced in relation to non-treated or low-temperature treated parts [92]. Literature studies show that prior β grains represent a key role in determining the mechanical response of heat-treated L-PBFed workpieces. In fact, as previously described, after heat treatment, the β grains are surrounded by αGB layers, which act as a weak junction point where failure preferentially occurs [94], as showed in **Figure 2.11**. In particular, heat-treated L-PBFed Ti6Al4V parts usually exhibit lower ultimate tensile stress and yield stress and higher elongation when the tension is applied along the longitudinal direction with the respect to the β grains [95].

Supertransus solution treatments (above 980 °C) can be useful to change the grain morphology and obtain equiaxial grains (see **Figure 2.8 (c)**), even if, as previously stated, the grains size considerably increases (see **Figure 2.9 (c)**) which is not the best feature for components with structural purposes.

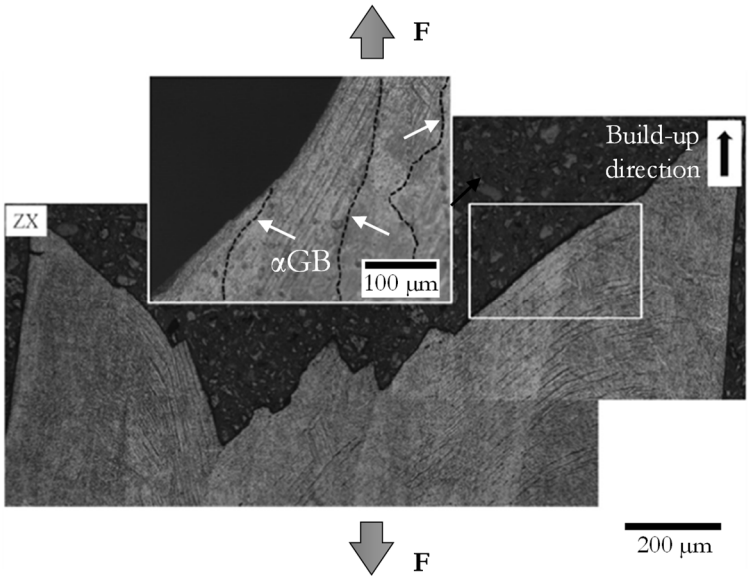

Figure 2.11: Fracture surface of a tensile test carried out along the build-up direction of a heat-treated L-PBFed Ti6Al4V sample. Adapted from [94].

The ultimate tensile and yield strengths reach similar values to that of the conventionally manufactured alloys with a 15% drop in Young modulus [92]. Even if with supertransus heat treatment an equiaxed structure is achieved, the anisotropy in mechanical properties can still be detected.

Table 2.5 reports the typical values of the main mechanical properties of as-built and heat-treated L-PBFed Ti6Al4V alloy. It is possible to conclude that L-PBFed Ti6Al4V remarkably differs from the one manufactured through conventional processes.

Table 2.5: Main mechanical properties of as-built and heat-treated L-PBFed Ti6Al4V alloy [92,94,95].

	Ultimate tensile strength (MPa)		Yield tensile strength (MPa)		Elongation at break (%)		Young modulus (GPa)	
	Long.	Trans.	Long.	Trans.	Long.	Trans.	Long.	Trans.
As-built	1117	1199	967	1075	8.9	11.8	119	113
High-Temp. subtransus	1041	1063	945	960	14.5	10.9	115	119
High-Temp. supertransus	951	1019	836	913	7.9	8.9	95	96.7
Low-Temp.	1052	1065	937	974	9.6	7.0	117	112

2.1.5 Surface generation in L-PBF

The surface roughness of AMed parts is determined by a series of interconnected input variables associated with the type of AM technology, process parameters, part design, and material feedstock. Among the metal AM methods, L-PBF provides the lowest surface roughness as reported in **Table 2.1** previously commented. Nevertheless, compared to conventional manufacturing processes, the quality of the surface topography is still a major disadvantage of AMed parts. To date, the possibility of minimizing roughness by tuning the process parameters is limited and, at best, it is possible to obtain surface roughness of about 5 μm [16].

The main reasons for which lower roughness is obtained with L-PBF are that powders with smaller granulometry and lower layer thicknesses are usually employed in such technology than the others. Both factors contribute to the reduction of the roughness of an AMed piece [13]. Keeping the AM technology and the type of metal powder constant, the factors that mostly influence the roughness of a L-PBFed part are its design and the improper melting of powders. The inclined and curved surfaces are approximated by stepped layers resulting in the so-called staircase effect (see **Figure 2.12**). The roughness resulting from the staircase effect depends on the layer thickness and on the build inclination angle and increases at increasing both the factors. Reducing the layer thickness to improve the surface topography should be weighted taking into account the resulting increase in part fabrication time. Alternatively, a modification in the part design can be considered to avoid critical build inclination angles of the surfaces of major interest [97].

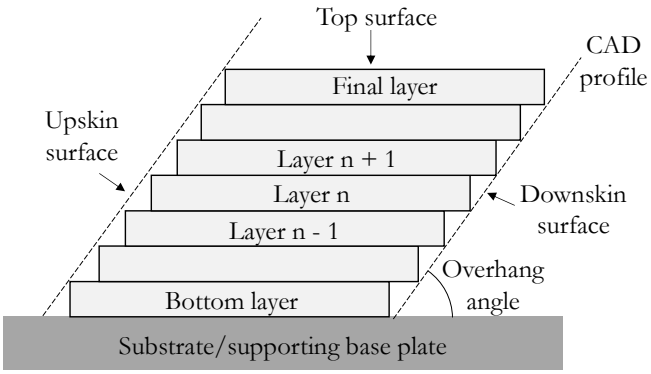

Figure 2.12: Staircase effect of L-PBFed parts. Adapted from [16].

The surface topography degradation due to the improper melting of powders is caused principally by partially fused particles, balling or spatter phenomena. When the energy density used in the process is insufficient, some powder only partially melts and stick on the printed part. The order of magnitude of the surface roughness, in this case, is comparable to that of the granulometry of the powder employed. The balling and spatter phenomena lead to the formation of confined protuberant features resembling spheres. When the laser scanning speed is excessively high, the melting pool becomes unstable, giving rise to the fluid mechanics phenomenon called Rayleigh instability. The melt pool tends to shrink breaking into small islands to reduce the surface energy, creating small drops of molten metal which are dragged on the edges of the molten pool solidifying as balls [98]. The balling phenomenon can be reduced by increasing the energy density intake by low scanning speeds and high laser powers. As a result, increasing the heat input help to minimize surface roughness [13]. Though, too high energy densities can be deleterious to surface finish because of a significant increase of thermal stresses and a non-uniform solidification rate. In fact, the spatter phenomenon usually takes place at high laser powers. This phenomenon gives rise to both micro and macroparticles with 20 - 100 μm of diameter, which stick on the solidified surface upon the laser scan. They originate when the flux of vapor on the surface is as high to create a pressure force that causes liquid metal to be ejected from the melt pool. Because of the surface tension inclination to reduce surface energy, when the liquid metal extends on the sides getting thinner and splits up into droplets [99,100].

Other surface features affecting the surface topography of L-PBFed parts are weld tracks and weld tracks ripples together with porosities. Weld tracks along the laser route are caused by laser-powder bed interaction during layer creation, whereas weld track ripples are caused by the thermocapillary convection flow (Marangoni effect) inside the melt pools. Upon the solidification of succeeding melt pools this results in semi-periodic patterns along the weld tracks [101]. Finally, the porosities which form into the bulk and previously described in Section 2.1.3, can be visible on the surface of the L-PBFed part as small voids or retreats. **Figure 2.13 (a)** reports a scheme of the just described features, while **Figure 2.13 (b)** reports experimental evidence of the surface of as-built L-PBFed Ti4Al4V parts under examination in this study.

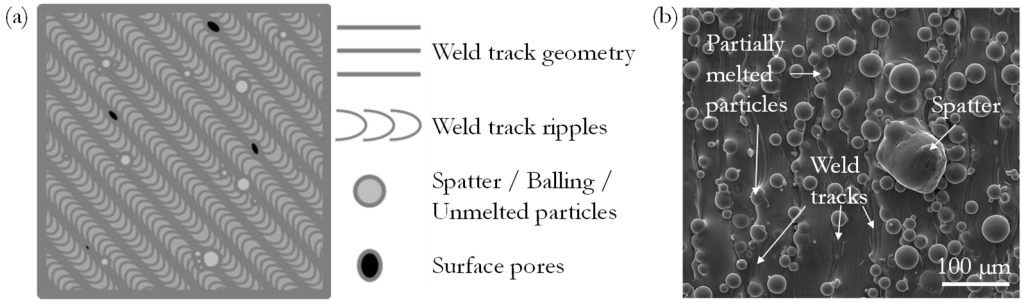

Figure 2.13: Scheme of the typical surface features of an L-PBFed part (a) adapted from [101], and experimental evidence of the surface of as-built L-PBFed Ti4Al4V parts under examination in this study (b).

It is worth noting that the parameters that influence the internal quality of an L-PBFed part are the same ones that influence also the surface topography. However, working with the parameters inside the optimal process window as reported in Section 2.1.2, does not necessarily lead to an optimized quality of the surface topography [16].

The considerations made in this paragraph make clear the need to resort to post-processing operations to increase the surface quality of L-PBFed pieces. L-PBFed components for high-end applications require high geometrical precision and surface quality, which can be achieved with machining operations to obtain a functional form and finish (see the workflow of **Figure 1.2**). Moreover, surface roughness can greatly affect the part performance since is one of the main factors influencing the high-cycle fatigue performance by offering spots for fatigue initiation [102]. As a result, post-surface treatments are critical for achieving excellent mechanical properties.

The next paragraph is devoted to the explanations of the concept of machinability and the criteria for its evaluation which will be later discussed on AMed parts.

2.2 Introduction to machinability

Machinability is a material property that refers to the ease or difficulty with which a given material, or group of them, can be machined, i.e. how simple or difficult it is to form the workpiece using a specific cutting tool [103]. Accordingly, all engineering materials are classified as either easy-to-machine or difficult-to-machine. Machinability is not only linked to the specific properties of the workpiece material, rather, it is regarded as a resultant property of the machining system that is directly or indirectly influenced by multiple factors such as the workpiece and tool materials, cutting parameters, cooling/lubrication strategies, part fixture, and machine tool. To evaluate the machinability a variety of parameters can be taken into considerations, which are grouped into tool life, chip formation mechanism, and workpiece quality. A scheme of the factors influencing the machinability and the machinability evaluation criteria are reported in **Figure 2.14**.

As anticipated, the Ti6Al4V alloy belongs to the difficult-to-machine materials because of its physical, chemical and mechanical properties. In fact, titanium and its alloys have low

thermal conductivity (see **Table 2.3**), therefore the heat developed during the cutting operation is slow to disperse and the majority of the heat is concentrated on the cutting edge and tool face, reducing tool life. Moreover, at tool operating temperatures, titanium has a strong alloying tendency and chemical reactivity with cutting tool materials. This results in smearing, welding, and galling, as well as fast cutting tool deterioration. Titanium and its alloys have a low Young modulus (see **Table 2.3**). This means that, especially at low depths of cut, the workpiece tends

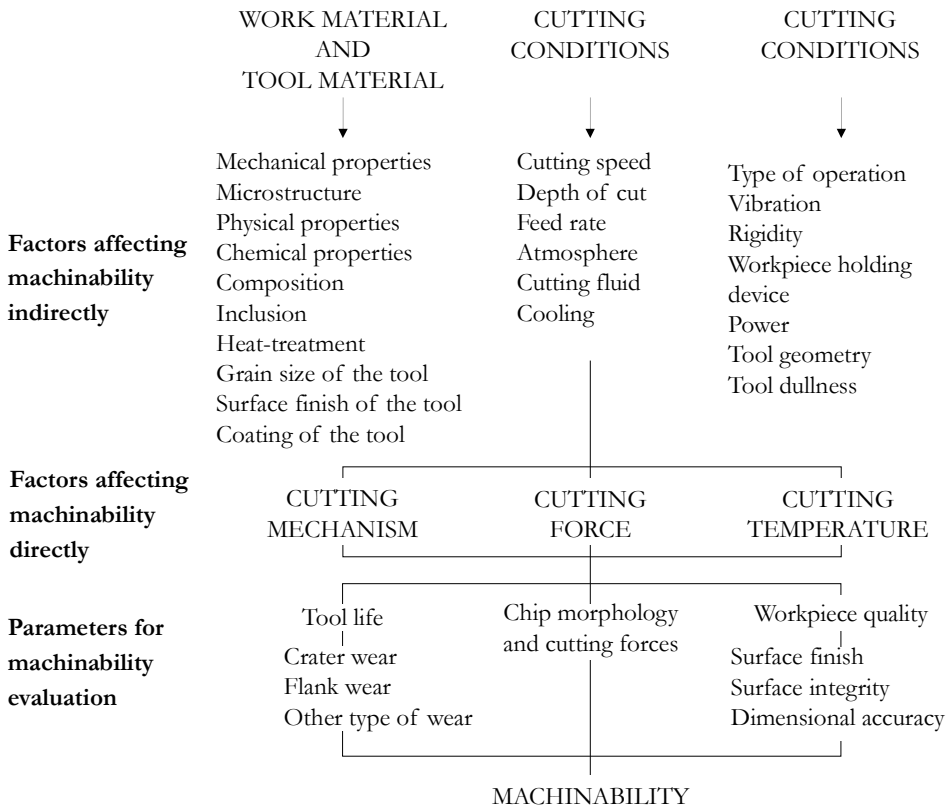

Figure 2.14: Factors influencing machinability and its evaluation parameters. Adapted from [104].

to undergo excessive elastic deformation, preventing a good finish. Moreover, slender parts are prone to deflect under tool pressure, which can lead to tool rubbing, chatter and, as a result, poor tolerances. Therefore, the overall rigidity of the machining system is critical, and sharp cutting tools with positive cutting edges and sufficient clearance angles should be used [103].

The most interesting criteria to evaluate the machinability, i.e. tool wear, chip morphology and cutting forces and workpiece quality, are described in detail in the following paragraphs, with specific comments on the Ti6Al4V alloy. At the end of this section, a paragraph is devoted to the main cutting fluids and their effects on the machinability of Ti6Al4V alloy.

2.2.1 Tool wear

During machining operations, the tool wears due to mechanical, thermal, and chemical loads. The tool wear extent depends on a range of variables among which the workpiece and tool material, tool geometry, cutting parameters, and cooling conditions are the most significant.

The main tool deterioration phenomena usually occurring are:

- Flank wear: tool material loss from the tool flanks during cutting, resulting in the gradual formation of a flank wear land. The flank wear width can be uniform, irregular, or localized and depends mostly on abrasion caused by undesired rubbing of the clearance face against the workpiece material
- Face wear: tool material progressive loss from the tool face during cutting. Face wear can be either crater type or stair-formed. The former consists in the gradual formation of a crater with the maximum depth at a certain distance away from the principal cutting edge and directed roughly parallel to it. The stair-formed face wear occurs when the maximum depth of the wear zone, measured perpendicular to the tool face, is at the intersection of the wear scar and the tool main flank. The rake face is subjected to high pressure and temperature stresses, and this type of wear is induced mostly by diffusive wear caused by cutting tool material dissolving into the chip substance. As a result, face wear is extremely temperature-sensitive and is highly dependent on the solubility of tool material in the workpiece one.
- Notch wear: excessive localized damage which occurs at the flank and rake face at the same time, resulting in the creation of a single groove.
- Chipping: deterioration of the tooth edge wherever parts of the edge break away. Chipping can be uniform, non-uniform, or localized.
- Flaking: tool fragments are lost as flakes from the tool surfaces. This deterioration phenomenon is most common in coated tools.
- Cracks: fracture of the cutting tool material without material loss. Cracks can form both on the tool face and tool flank perpendicularly, parallel, or irregularly located with respect to the main cutting edge.
- Catastrophic failure: rapid and unexpected complete failure of the cutting edge.

The above-reported tool wear phenomena can be utilized as tool-life criteria, i.e. a predefined numerical value of a certain type of tool wear that defines when the end of tool life has been reached. The deterioration phenomena definitions and tool-life criteria are recommended by ISO 8688-2 standard [105] for end milling and ISO 3685 standard [106] for turning operations. The common tool life end criterium is the width of the flank wear land which is recommended to be 0.3 mm averaged over all teeth for the uniform type of wear and maximum 0.5 mm on any single tooth for the localized type of wear. Other kinds of tool-life criteria can be used if the flank wear width can not be applied for the studied case, such as the depth of face wear or chipping.

For a given tool-workpiece combination, tool wear is frequently expressed as a plot of tool deterioration against tool sliding distance or cutting time, forming the so-called tool wear curve (see **Figure 2.15**). Usually, the tool wear curves can be divided into the three conventional zones [107], namely:

(i) Rapid initial tool wear: significantly high wear rate occurs due to increased wear caused by tool layer deterioration during cutting.

(ii) Uniform tool wear: a steady-state region in which regular cutting tool action should take place.

(iii) Accelerated tool wear: rapid wear region that end with cutting tool failure. This region is frequently characterized by significant cutting forces and temperatures, as well as intense tool vibrations.

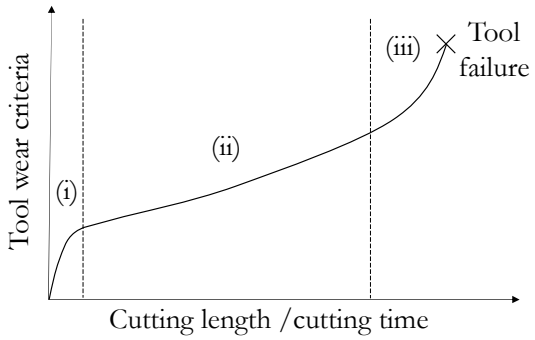

Figure 2.15: Typical tool wear curve reporting the evolution of the tool deterioration and cutting length or cutting time.

The main tool wear phenomenon causing the tool deterioration when machining Ti6Al4V alloy is adhesion, besides abrasion and attrition. Ti6Al4V alloy is characterized by a good chemical inertness at room temperature, making it appropriate for biomedical implants, however, it becomes very reactive when temperatures exceed 500 °C. Therefore, under the temperatures developed during cutting operations, there is a high tendency to react between the tool materials and the titanium alloy through diffusion/dissolution mechanism. Consequently, the chips produced tend to stick to the cutting edges, leading to build up edge (BUE) formation which leads to chipping and premature tool failure. For this reason, coated cutting tools are not always the best choice to cut titanium alloys. In fact, the most common coatings contain Ti (such as PVD-TiAlN), increasing their chemical affinity, and thus reactivity, with the workpiece material. Special tungsten carbide uncoated tools with ultra-fine grains and high abrasive resistance of the flank are available for machining Ti6Al4V alloys [108]. Also in the latter case, the dominating tool deterioration phenomena are the diffusion/dissolution which is promoted at increasing cutting temperatures [109] and micro-chipping. Moreover, high cutting speeds and temperatures can cause the formation of cracks due to thermal shock. To machine titanium alloys, sharp tools and inserts with positive cutting edges are recommended.

2.2.2 Chip formation and cutting forces

Machining operations always result in chips formation: the cutting edge penetrates the workpiece material, which is thereby plastically deformed and slides away along the rake face of the cutting tool [110]. Chip formation influences to a great extent cutting forces and temperatures, thus tool wear and workpiece surface integrity [106]. As a result, it is essential to comprehend the cutting conditions that lead to easy-to-handle chips while minimizing the detrimental impacts on the cutting tool and workpiece surface. Chips can be classified into different typologies reported in **Figure 2.16 (b)**. *Discontinuous chips* arise when the chip does not undergo plastic deformation and is cyclically broken up into little fragments since cracks propagate throughout its thickness. This type of chip is typical of brittle materials or materials

with stress concentration areas. They can also be formed when cutting ductile materials at extremely low speeds and feed rates. When evaluating the chip formation during the cutting of titanium alloys, the most researched aspect is the development of adiabatic shear bands [111]. The two main theories developed to describe the chip formation mechanism are the shear instability and the crack initiation and propagations ones, but there are still some aspects that need to be fully understood. It is widely believed that the chip formation mechanism in titanium alloys upon machining, is based on adiabatic shear, also known as thermoplastic instability, within the primary cutting zone, which is mostly originated by the localized shear deformation and happens when the thermal softening rate exceeds the one of hardening. The poor thermal conductivity of such alloys, lead to heat accumulation in the primary shear zone and thus to cutting temperatures increase also in the secondary deformation zones, which can ultimately lead to a metallurgical transformation. In particular, the α phase transformation to β phase one is promoted. The latter may further favor adiabatic shear banding because of its higher number of slip systems. Some researchers believe that at low cutting speeds the chip formation mechanisms for titanium alloys can be of crack initiation and growth type. The crack can originate at the free surface of the chip and propagate to the tool tip or the opposite [112]. Adiabatic shear leads to *segmented chips* (see **Figure 2.16 (b)**), characterized by zones of strong localized shear separated by zones of material with lower deformation. This type of chip is usually obtained at high cutting rates; however, segmentation can occur at relatively low speeds for materials with low heat conductivity and thermal capacity, such as titanium alloys. If the heat developed in the cutting zone is not dissipated rapidly enough, the catastrophic shear becomes confined, and the narrow chip segments formed are separated by undeformed regions [113]. Such segment separation becomes more pronounced at increasing cutting speed, until complete segment separation occurs, resulting in *elemental chip* creation (see **Figure 2.16 (b)**).

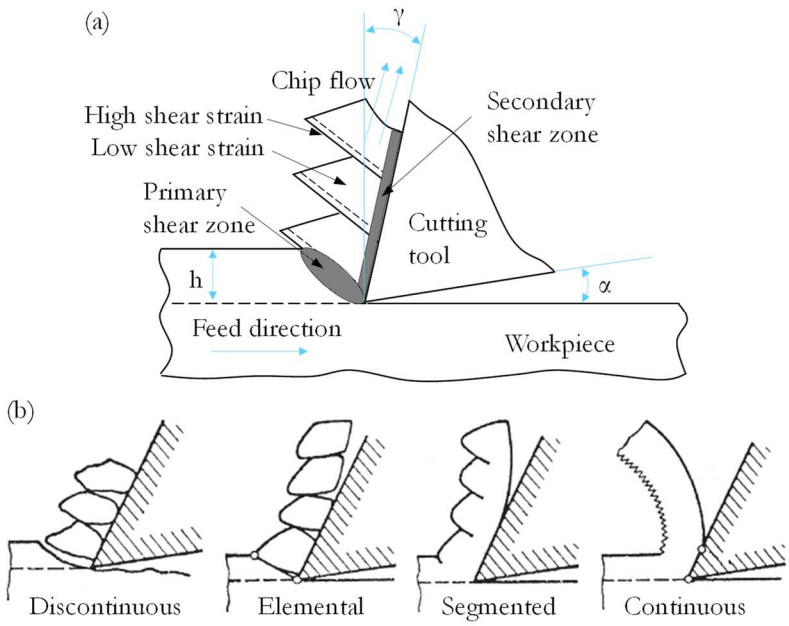

Figure 2.16: Schematization of the chip formation mechanism where h: uncut chip thickness, α: clearance angle, γ: rake angle (a), and classification of chip typologies (b). Adapted from [103,114].

Shear localization causes large periodic fluctuation in machining forces and, as a result, chatters vibration [115]. Such cyclic variation of forces should be avoided, by choosing the appropriate cutting parameters, as it subjects the cutting tool to fatigue stresses and may result in chipping or catastrophic failure of the cutting edges. Segmented chips are common when machining titanium alloys at a variety of cutting speeds and feed rates, a couple of examples are reported in **Figure 2.17**, where it is visible that the shear localization is more marked at higher cutting speed. This is a key issue when machining titanium alloys. Usually, low cutting forces and good surface finish are related to the formation of *continuous chips* (see **Figure 2.16 (b)**), typical of ductile materials with uniform and fine-grained microstructure [103]. In this case, the chip slides away along the rake face of the tool with a constant rate in a stationary flow and is promoted by high cutting speeds, positive rake angles, low friction on the rake face, and low undeformed chip thickness. A sub-category of continuous chip is the *lamellar chip* which presents cleavages on the free surface due to uniform concentrated shear bands. The lamellae develop as a result of thermal or elastomeric phenomena at high frequency formation and are usually found when machining highly ductile materials with increased strength, favored by high cutting speeds [110]. Continuous chips can be of various shapes according to the ISO 3865 standard [106], such as ribbon-like, helical, spiral, needle-like etc., further subdivided into long and short, i.e. size, and in snarled, connected, or loose, i.e. physical condition. As previously anticipated, the chip form is strictly connected to the workpiece material, tool geometry and condition, as well as the used cutting parameters. Therefore, when comparing the chip of different cutting operations, a difference in their morphology implies a difference in the abovementioned variables, giving valuable information about the cutting operation and tool conditions. Finally, it is worth to underline that chip formation is highly affected by the microstructural state of the material, and this is particularly true in the machining of titanium alloys [116], because of its allotropic nature.

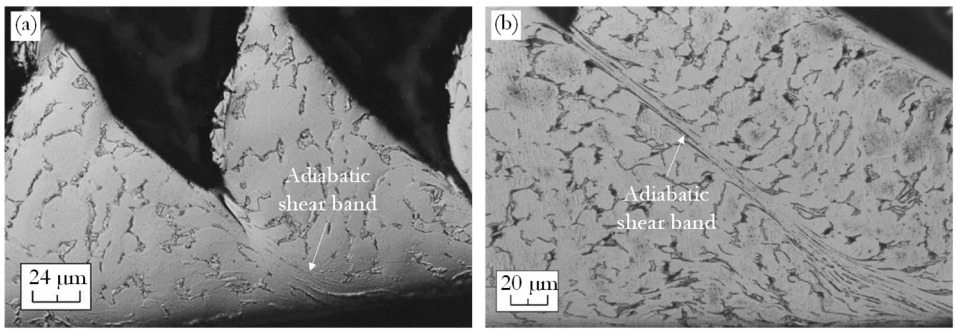

Figure 2.17: Adiabatic shear bands in Ti6Al4V titanium alloy chips, obtained by orthogonal cutting at 1.2 m/s (a) and at 13 m/s (b) of cutting speed. Adapted from [111].

Cutting forces in machining are affected by a variety of factors relating mainly to workpiece properties, cutting parameters and machine system stability. Usually, workpiece materials with higher hardness and yield strength lead to higher cutting forces because of the increased difficulty in chip formation [117,118]. Among the cutting parameters, the more influencing on the cutting forces are the depth of cut, cutting speed and feed per tooth [119]. Usually their increase leads to increased cutting forces because of the strain hardening mechanism of the work material prevailing over the thermal softening one. However, in a certain range of cutting

forces or feed per tooth, the softening prevails over the hardening, because of high heat generation lowering the material flow stress, leading to lower cutting forces [115,120]. The machining system is made up of the machine tool, cutting tool, and workpiece that is held in place on the working zone by a fixture system. The dynamic characteristics of the overall system are quite complex and, as a result, vibrations might often occur under certain unfavorable machining circumstances. The vibrations, which can be natural, forced or self-excited, can influence the cutting forces and thus the machining performance [103]. In the case of titanium alloys, the low Young modulus can easily lead to variations in chip thickness thus favoring high vibration levels, especially chattering or self-excited ones [121]. The cutting forces control is of primary importance since, as the cutting forces increase, there is an increase in tool wear and a worsening of the surface quality.

2.2.3 Workpiece quality

Machining operations greatly affect the quality of the workpiece material in terms of topographical, metallurgical, and mechanical modifications, i.e. the surface integrity. Topographical modifications include the surface finish variations such as the surface texture and the occurrence of defects, metallurgical alterations may include phase transformations and microstructural deformations, whilst mechanical modifications comprise hardness variations and the change of the residual stresses state [122]. In **Figure 2.18** is reported a schematization of the surface and sub-surface alterations induced by machining operations. The surface integrity of a component greatly affects its in-service performances such as corrosion and fatigue resistance [123], therefore its study can provide important information both on the machinability and on the component properties after machining.

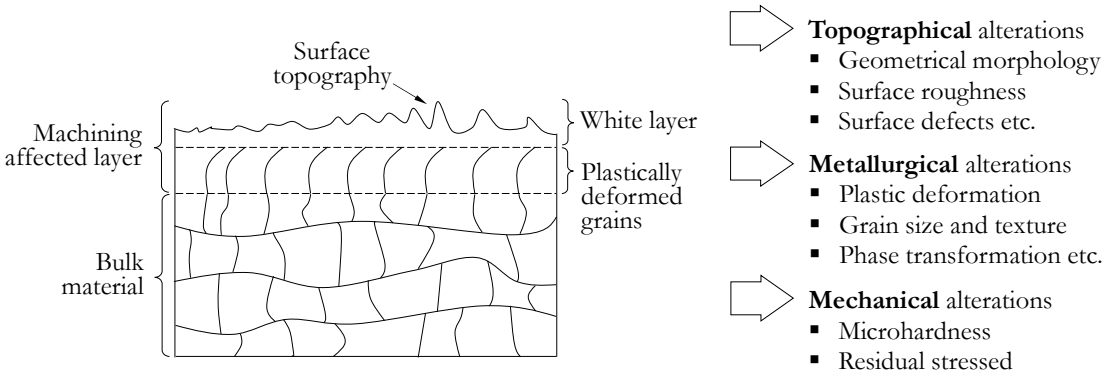

Figure 2.18: Schematization of the surface integrity alterations induced by machining operations.

The main surface modification induced by a machining operation is the texture affecting the surface roughness parameters. In fact, the tool cutting edge forms a series of peaks on the workpiece surface, forming a lay pattern in accordance with the cutting parameters used for the machining operation. The dominant pattern usually is defined by the so-called feed marks, which are spaced apart as much as the feed per tooth set for the operation. The higher the feed the lower the density of peaks and the higher their height [103,124], which usually leads to higher surface roughness. In **Figure 2.19** is reported a visual example of what was just described. Generally, an increase of the cutting speed in milling operations improves the

surface quality [125], however, in turning operation the opposite is valid. In fact, at higher cutting speed, the cutting temperature usually increases due to the increased tool-workpiece interactions, which are known to trigger additional friction which converts into heat deteriorating the surface quality [103]. Besides the effects of the cutting parameters on the surface texture, also the cutting tool geometry has a great effect on it. For instance, larger nose radii, and positive rake angles help to reduce the surface roughness in turning operations [122]. Among the main surface defects of Ti6Al4V machined surfaces there is adhered material, typically smeared chips or chip debris, besides grooves, smeared feed marks, and matrix tearing [126]. Usually, the increasing cutting speed and depth of cut lead to a higher amount of adhered material debris and smearing, because of the increase in temperature around the tool tip [24,127].

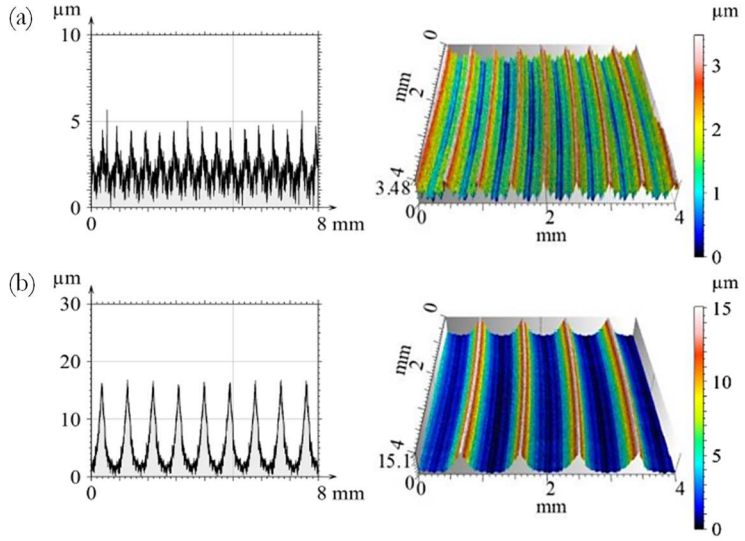

Figure 2.19: Roughness profiles and 3D topographies of face milled surfaces at feed per tooth equal to 0.5 mm (a) and 0.9 mm (b). Adapted from [124].

Typically, machined sub-surfaces present grains deformed along the direction of the cutting operation, due to the forces generated by the high strain rates and elevated temperature generated by the tool-workpiece interactions. Such plastically deformed layer can be up to several micrometers of depth and is mainly controlled by both cutting parameters and tool conditions. In fact, the plastic deformation of the sub-surface grains induced by cutting can become more pronounced if more severe cutting conditions are applied or if the tool presents extensive wear [126]. The plastic deformation of grains generally leads to an increased microhardness in such layer, due to the work hardening behavior of metal alloys such the titanium ones. If high temperatures generate during the cutting operations and the heat is not adequately removed by cutting fluids, thermal softening can overcome the strain hardening, and a decrease in the sub-surface microhardness can be detected. When machining Ti6Al4V alloy, the formation of the so-called white layer can take place. White layers are commonly defined as sub-superficial areas where the microstructure is not discernible at a resolution that resolves the bulk and appears white-colored under optical light microscopy. They are composed of ultra-fine grains formed by continuous dynamic recrystallization driven by severe plastic deformation under the high strain rates during cutting operations. The ultra-fine-grained

microstructure of the white layer induces higher hardness and lower Young modulus than the bulk material and can greatly affect the workpiece in-service performances [128].

All the energy involved in the cutting process is not recovered after the release of the thermomechanical loads at the end of the machining operation. Some of it is lost due to plastic deformation of both the chip and workpiece, as above commented. The latter frequently exhibits stresses at the surface and sub-surface even after the load removal, which are therefore named residual stresses. Such stresses significantly influence the mechanical properties as the fatigue resistance and can trigger a crack initiation on the surface, especially if of tensile type, therefore should be removed or prevented. There is no general rule defining the nature (tensile or compressive) of residual stresses after machining, since they are highly sensitive to multiple factors such as workpiece material, cutting tool geometry, cutting parameters, and cooling conditions [122]. Very frequently, a peak of compressive residual stresses is found at a certain distance from the machined surface [122].

The workpiece quality is affected also by the formation of the so-called burrs, which are undesirable protrusions of material over the workpiece surface or a missing portion on the workpiece edge. Burrs formation is associated with serious issues such as the risk of finger injuries for assembly workers, the creation of debris sites during operations, reducing the lifetime of the machined component, reducing tool life, problems in parts assembly operations. As a result, burrs should always be removed, which is a time-consuming and inefficient step in the process chain. Furthermore, it has a significant impact on the production costs: it is estimated that deburring can account for 30% of the cost of the finished part milling [129]. Consequently, burr formation should be minimized. Burr formation is influenced by a variety of elements such as cutting parameters, workpiece mechanical properties, tool and workpiece geometry. Machining ductile materials produces larger burrs at greater cutting speeds and feed rates [130]. The burr height varies erratically with changing cutting parameters and the results of experimental research are not always comparable. In general, very high or low cutting parameter levels are not recommended during milling operations. Tool wear is the factor that most affects the formation of burrs, increasing their extent.

All the above-mentioned features related to machining are greatly affected by the use of cutting fluids, as reported in detail below.

2.2.4 Cutting fluids and their influence on machinability

Supplying cooling lubricants into the cutting zone help improving the cutting performance by decreasing the tool wear, besides improving the surface quality of the workpiece. In fact, the use of appropriate cooling lubricants reduces the mechanical, thermal, and chemical loads acting on the cutting edge. Furthermore, thanks to the cooling action of such fluid, the heat is removed from the chip formation zone, positively impacting the surface integrity of the workpiece. Whilst, by lowering the tool-workpiece friction thanks to the lubricating action of such fluids, the cutting force and power are minimized while improving surface quality. In general, the lubricating function is more relevant in low cutting speed operations, while the cooling function in higher cutting speeds because of greater heat development. Fluids with a primary lubrication function must be provided in order to establish a wear-protected coating

on the sliding surfaces, while coolants must penetrate to the tool cutting edge. Besides the main functions just mentioned, the cooling lubricants serve also to remove the chips from the cutting zone and to prevent undesired chemical reactions of the newly generated surfaces [110].

A general classification of coolant fluids is to divide them into mono and bi-phase fluids. The first category includes liquids or gases, the second includes solid suspensions and fluid-gases mixtures. Liquid cooling lubricants are the most widespread and are divided into neat oils, mineral-soluble oils, semi-synthetic fluids, and synthetic fluids [103].

The principal delivery strategies of the cooling lubricants are flooding, minimum-quantity lubrication (MQL), cryogenic cooling, and compressed air. Flooding is the most common way of delivering cooling lubricants which consist of supply a large amount of fluid with a low-pressure nozzle on the cutting zone. It allows for a continuous flow of fluid while also removing chips from the cutting zone. The typical flow rates of such cooling delivery method range between 30 and 1000 l/h [131]. The high amount of fluid consumption is the main limitation of this cooling/lubrication technique, causing dangerous effects on workers' health, and on the environment, besides high machining costs. To overcome these disadvantages, efforts have been put to find effective alternatives. Machining in dry conditions can be an option to reduce health and environmental impacts, however this technique it is not always applicable, especially when machining difficult-to-cut materials such as titanium alloys. A successful alternative is the MQL delivery strategy [132]. MQL consist of a mixture of compressed air and a little amount of oil in the form of thin drops generating an aerosol on the cutting zone. This type of system has mainly a lubricating action rather than a cooling one, and the heat is removed mainly by compressed air. The most common media used in MQL are synthetic esters, which are vegetable oils chemically modified and fatty alcohols, which are long-chained alcohols derived from mineral oil or natural raw materials [133]. MQL reduces the cutting forces, lowers contact temperature, and improves chip control by shortening the contact length between the insert and the material [103,134]. In **Figure 2.20** the effects of different cooling lubricating conditions in milling operation are reported, showing that MQL is more effective than wet (flood) cooling condition in increasing the tool life. The principal mechanism of machining improvement by MQL is the so-called Rebinder effect: tiny particles infiltrate the workpiece surface and help the plastic flow at the rear surface of the chip.

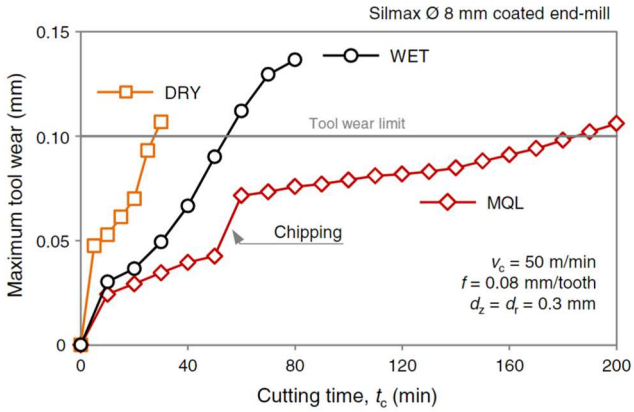

Figure 2.20: Tool wear curves at varying cooling lubricating conditions in milling operations of a titanium aluminide-based alloy [134].

In this system the flow varies between 0.01 and 2 l/h, lowering to a great extent the cutting fluid consumption, which is the main benefit of this technique [131]. Consequently, this allows for a reduced health hazard for the workers and to reduce environmental pollution (no need for lubricant disposal) with respect to conventional cooling lubricants strategies.

Cryogenic cooling consists of the delivery of cryogenic fluid such as liquid nitrogen or liquid carbon dioxide at temperatures well below 0 °C. The benefits of such cooling strategy are multiple. When delivered onto the cutting zone, the cryogenic fluid immediately evaporates and returns into the atmosphere leaving no residues or contaminants on the workpiece. This allows for the erasing of the disposal costs of the cutting fluid and the cleaning of the workpiece, besides the advantages in terms of the environment. Moreover, with the low temperatures characterizing such process, it is possible to increase the cutting rates without affecting the tool wear, reducing production costs and increasing productivity. Finally, the surface integrity can also take advantage of the low temperatures since phase changes are prevented, and dynamic recrystallization is favored. Cryogenic cooling is particularly advantageous for materials such as titanium, which present low thermal conductivity and low Young modulus. In fact, the low cutting temperatures hinder the material to stick, reducing the tool-chip frictional forces and induce the work material to become harder and stronger, preventing the tool rubbing [135]. A comparison between the surface defects of flood and cryogenic machining is reported in **Figure 2.21**. Flood cooled surface is characterized by a higher amount of adhered material than cryogenic cooled one.

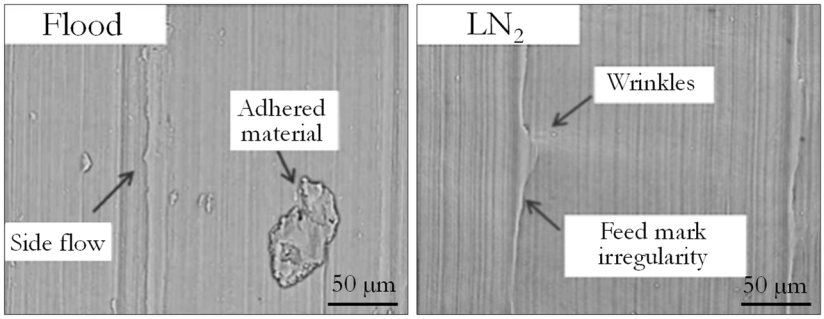

Figure 2.21: Comparison between defects of surfaces machined with flood and liquid nitrogen cooling. Adapted from [136].

In general, when machining titanium alloys cutting fluids have to be employed to reduce high stresses and temperatures. The cutting fluid has to function both as coolant and lubricant to minimize the cutting forces and avoid chip welding, which is a phenomenon often experienced during titanium machining.

The observations reported in this chapter clarified why titanium alloys, including the Ti6Al4V one, with its microstructural and mechanical characteristics, are considered a difficult-to-machine material with respect to other metal alloys with comparable hardness. In order to accomplish a good machining efficiency at acceptable costs, suitable cutting tools, cutting conditions, and machine system must be chosen appropriately.

2.3 Machinability of AMed parts

At present, the optimization of the AM process parameters can only partially solve the high surface roughness that characterizes the as-built AMed parts due to the intrinsic phenomena taking place during the manufacturing process, as discussed in Section 2.1.5. In practice, almost all the AMed parts need some post-processing steps to smooth their functional surfaces [26,102]. AMed components for high-end applications, such as for the automotive and aerospace industries, require high geometrical precision and surface quality, making it necessary post processing operations such as machining, grinding, chemical polishing, shot peening to obtain a functional form and finish. CNC milling and turning are the most common post-processing technologies to finish the surface of components and are frequently employed in the processing of complex parts thanks to digital control systems. These post-processing operations encounter some issues when applied to AMed artifacts, because of the peculiar microstructure of the latter. The mechanical anisotropy, derived from the microstructural anisotropy, has been widely studied for various metal alloys, as discussed in detail in Paragraph 2.1, and it has been shown that the presence of the columnar grains strongly affects the local mechanical properties of each metal alloy. However, the machining response of anisotropic microstructures of AMed parts has not been investigated in depth, yet and gained attention only in the last years.

The majority of the works on AMed parts machinability deals with the Ti6Al4V alloy and with L-PBF, which are the most widespread among AMed metals and technologies, respectively, as commented in the Introduction. In general, works on milling operations are more common than turning ones. Among metal alloys other than the titanium ones, the most studied are the steels. In particular, in a work by Guo et al. [24], the AISI 316L stainless steel manufactured via L-DED was face milled in dry condition and its machinability was studied in detail. They found that the cutting force, the tool wear and the surface roughness *Ra* of the samples with a build-up orientation of 0° is higher than those with 90° build-up orientation. These results were correlated to the samples Rockwell macrohardness, which was higher in the first group of samples than in the second one because of the microstructural anisotropy. The main results are reported in **Figure 2.22**. Fortunato et al. [26] studied the tool wear, cutting forces, and surface roughness *Sa*, in dry face milling of L-PBFed maraging steel with different heat treatments. However, the microstructural investigation was limited and no explanation on the correlation between the microstructural anisotropy and the machinability was given. A similar study was conducted by Bai et al. [25], which, however, conducted also the chip morphology analysis and phenomenology, besides a deeper workpiece quality examination. Moreover, they advanced a hypothesis on the correlation between microstructure and machinability. They found that, in the as-built samples, the differences in cutting forces at varying the cutting direction were due to the interactions between the cutting tool and the melt tracks. Fernandez-Zelaia et al. [137] evaluated the machinability of the L-PBFed CoCrMo alloy, limiting their study to the machining force response. They showed that the cutting force was sensitive to the part mechanical anisotropy driven by both the morphology of the microstructure and crystallographic texture. Ball end milling on WAAMed nickel-based alloy was carried out by Schroepfer et al. [138] considering the cutting forces and the surface integrity

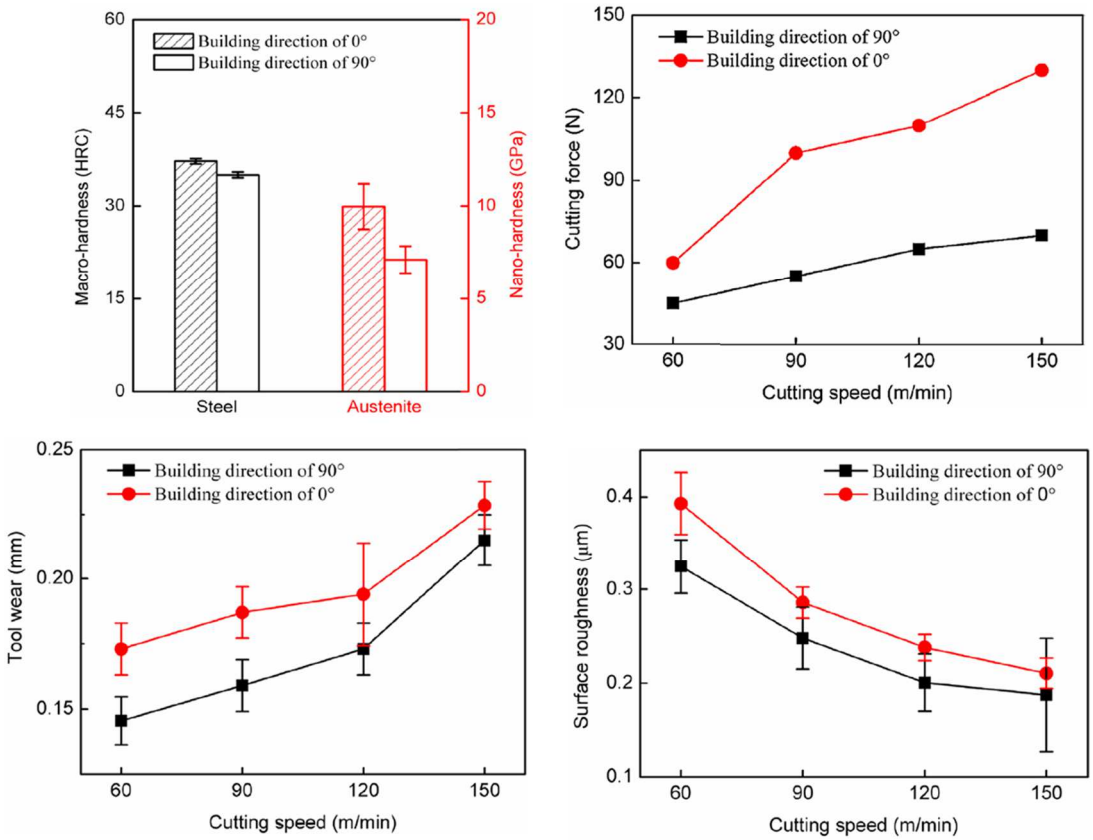

Figure 2.22: Main results of the study by Guo et al. on the L-DEDed AISI 316L machinability [24].

of the machined samples. This study revealed that ultrasonic-assisted milling allowed for lower cutting forces, surface roughness, and tensile residual stresses than conventional milling. Therefore, the attention was put principally on the machining process rather than on the AMed part microstructure. A study on the machinability CrMnFeCoNi high entropy alloy manufactured by L-PBF was conducted by Litwa et al. [139]. The effect of end milling operations was considered on a wide range of machinability parameters, however, the study mainly focused on the differences between the AMed alloy and a conventionally manufactured stainless steel, without any reference to the AM-induced microstructure. Zhao et al. [140] performed dry end milling on L-DEDed FeCr alloy considering mainly the cutting forces and the chip morphology. They found that the cutting speed and vibrations reached a peak when cutting in correspondence of the welding line between two successive layers because of the finer microstructure in those zones. The surface quality was not analyzed.

For what concerns the machinability of AMed Ti6Al4V alloy, Hojati et al. [141] investigated the machinability of the EB-PBF titanium alloy under flood micro-end milling operations. They compared the cutting forces, burrs morphology and surface quality with the same conventionally manufactured alloy. The surface quality analysis was limited to two roughness parameters (namely *Sa* and *Sz*), without any insight on the microstructure. A wide machinability characterization was carried out by Ni et al. [142] on end milling operations on L-PBFed Ti6Al4V alloy, in comparison with the conventionally manufactured one. The AMed samples were manufactured with different rotations angles between subsequent layers, namely 0° (perfectly overlapped layers), 90° and 67.5°. The cutting force results were related to the

different microhardness among the analyzed samples and surfaces, however, no interpretation on the different surface quality was made concerning the microstructure. They found that the microhardness of the top surfaces was always higher than on the front surfaces, which consequently led to higher cutting forces in the first case than in the second, as reported in **Figure 2.23**.

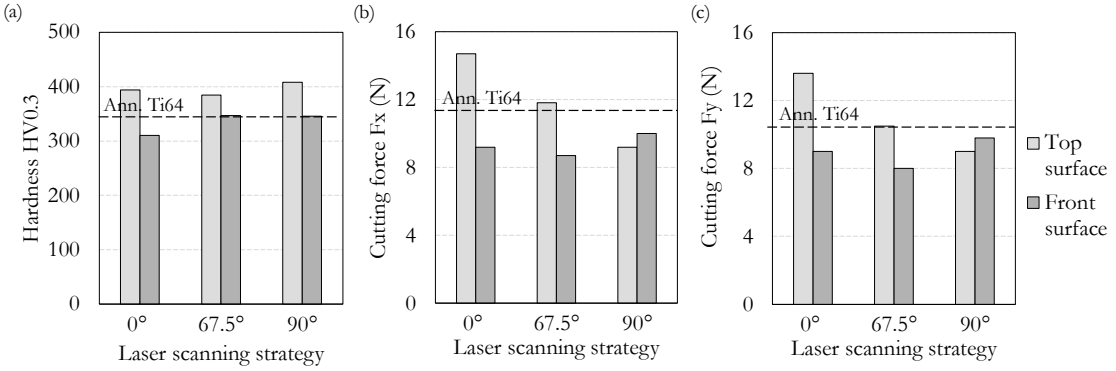

Figure 2.23: Comparison of microhardness (a), cutting force in *Fx* (b) and *Fy* (c) directions between the top and front surfaces of different L-PBFed Ti6Al4V alloys. The dashed lines refer to the values of the wrought annealed Ti6Al4V alloy. Adapted from [142].

Dry face milling was instead carried out on the same alloys of the previous work by Milton et al. [143]. The surface roughness *Ra* results were not commented in relation to the microstructural consideration. The latter was only nominated commenting the cutting force results but without going into detail. they found that the *Ra* values were the lowest when machining the side surface of the samples, perpendicularly to the build-up direction, which corresponded to the lowest axial cutting force, the only component of the cutting force to have led to differences between the samples. For what concerns turning, few documents on the AMed Ti6Al4V alloy have been found. The majority of them focused on the study of surface integrity and tool wear of AMed Ti6Al4V with the analog wrought alloy [144,145], showing the worst machinability of the former. In particular, Shunmugavel et al. [144] carried out face turning operations on L-PBFed Ti6Al4V alloy after low-temperature heat treatment and compared the results with the wrought annealed Ti6Al4V alloy. They found that the cutting tool wears out more when machining the AMed Ti6Al4V as compared to wrought alloy, which increased at increasing the cutting speed. The higher tool wear resulted in higher surface roughness *Ra*, higher amount of adhered material on the surface, and higher depth of plastically deformed grains. The results were explained in relation to the higher brittleness and microhardness of the AMed alloy than the wrought one without referring to the material anisotropy. Sartori et al. [145] analyzed the tool wear in longitudinal turning of Ti6Al4V alloy manufactured via both EB-PBF and L-PBF. The latter was machined both in as-built and heat-treated conditions. The same cutting operations were carried out on the wrought annealed Ti6Al4V alloy, both in dry and cryogenic conditions. The wear of the cutting insert was extensively studied and it was concluded that the EB-PBFed alloy has the best machinability, the as-built L-PBFed the worst one, whereas the wrought and heat-treated L-PBFed are comparable. Cryogenic cooling conditions allowed for a reduction in tool wear. The results were correlated to the different thermal conductivity of the alloys differently manufactured. The machinability in longitudinal turning operations of L-DEDed Ti6Al4V alloy was assessed

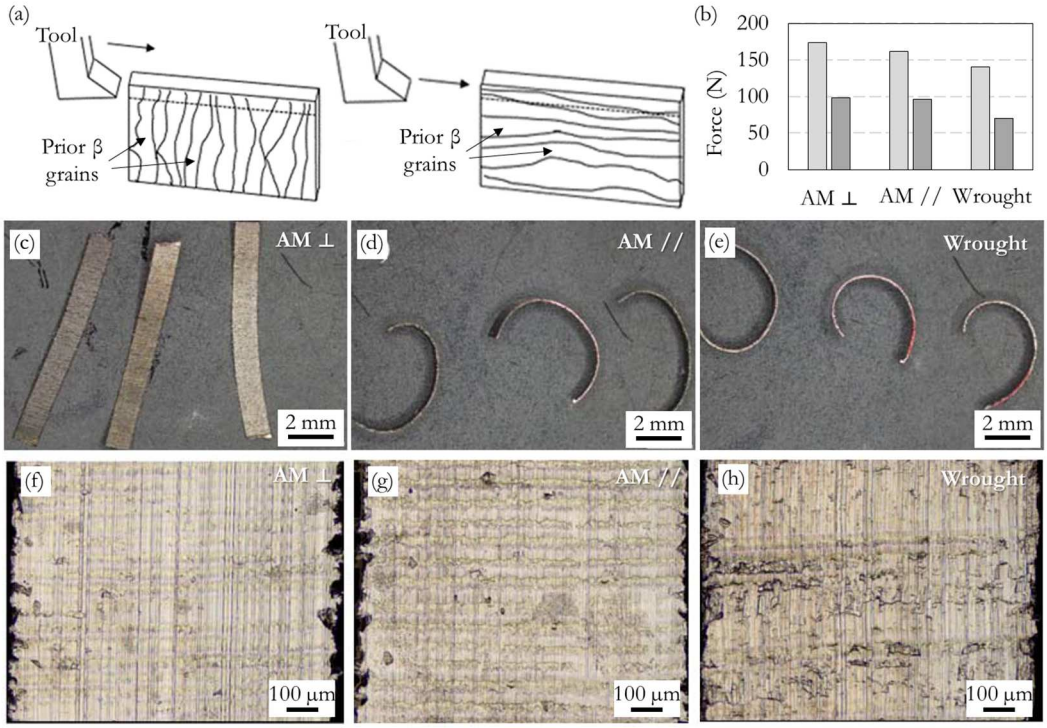

Figure 2.24: Tool-workpiece configuration during orthogonal cutting of L-PBFed Ti6Al4V with cutting tool perpendicular (AM ⊥) and parallel (AM //) to the prior β grains (a), cutting forces (b), chip morphology (c), (d), (e) and surface finish (f), (g), (b) in AM ⊥, AM // and wrought alloy machining, respectively. Adapted from [146].

by Oyelola et al. [147]. The study principally focused on the different machinability between coated and uncoated inserts, rather than on the effect of the AM-induced microstructure role. Lastly, a work on machinability in orthogonal cutting of heat-treated L-PBFed Ti6Al4V and wrought Ti6Al4V alloys was conducted by Shunmugavel et al. [146]. They examined the influence of the build-up orientation on the machinability of the AMed titanium alloy at different cutting directions with respect to the main microstructural features, i.e. the prior β grains. They found that the cutting forces are higher when machining perpendicularly to the build-up direction across prior β grains, than when machining parallelly to the prior β grains or the wrought samples. The first condition led also to straighter chips and better surface finish thanks to limited tool-workpiece friction and sticking phenomena compared to the other cutting strategies. The main results are reported in **Figure 2.24**. This is the first work concerning the machinability of the L-PBFed Ti6Al4V alloy in which microstructural anisotropy was considered, pointing out the different machinability depending on the workpiece orientation to the cutting edge. However, orthogonal cutting operations are not representative of the conventional cutting conditions used at the industrial level.

In **Table 2.6** a summary of the analyzed literature dealing with the machining of AMed metals is reported. It is worth noting that none of the aforementioned studies, particularly on AMed Ti6Al4V alloy, gave a detailed explanation to support the correlation between microstructural anisotropy and machinability. Moreover, the analyses of the surface topography were in all cases scarce, and the great majority of them referred to linear roughness parameters, instead of the more reliable areal roughness parameters.

Table 2.6: Summary of the literature dealing with AMed metals machining.

Material	Machining operation	Machinability parameters					Ref.
		Tool wear	Cutting forces	Chip morphology	Surface topography	Other workpiece qualities	
EB-LBFed Ti6Al4V	Micro-end milling	×	✓	×	Limited to *Sa* and *Sz*	Burrs morphology	[141]
L-PBFed Ti6AL4V	End milling	×	✓	✓	Limited to R*a*	Surface defects	[142]
L-PBFed Ti6AL4V	Face milling	×	✓	×	Limited to R*a*	Metallographical alterations, nanohardness	[143]
EB-LBFed and L-PBFed Ti6Al4V	Longitudinal turning	✓	×	×	×	×	[145]
L-PBFed Ti6AL4V	Face turning	✓	×	×	Limited to R*a*	Surface defects, metallographical alterations	[144]
L-DEDed Ti6Al4V	Longitudinal turning	×	×	✓	Limited to R*a*	Metallographical alterations, microhardness, residual stresses	[147]
L-PBFed Ti6AL4V	Orthogonal cutting	×	✓	✓	×	Surface defects	[146]
L-PBFed M300	Face milling	✓	✓	×	Limited to *Sa*	Hardness	[26]
L-PBFed M300	Face milling	✓	✓	✓	Limited to R*a*	Surface defects, microhardness, metallographical alterations	[25]
L-DEDed AISI 316L	Face milling	✓	✓	×	Limited to R*a*	×	[24]
L-PBFed CoCrMo	Slot milling	×	✓	×	×	×	[137]
WAAMed IN725	Ball end milling	×	✓	×	Limited to R*a* and *Rt*	Surface defects, metallographical alterations, residual stresses	[138]
L-PBFed CrMnFeCoNi	End milling	✓	✓	×	Limited to R*a*	Surface defects, microhardness, metallographical alterations	[139]
L-DEDed FeCr	End milling	×	✓	✓	×	Microhardness	[140]

2.4 Conclusive remarks

The machinability of parts fabricated by AM technologies has recently aroused the interest of the scientific community working on metal machining. This is attributable to two main reasons: (i) the surface finish and geometrical tolerances of AMed parts can be quite far from those requested for the part in-service performances, and (ii) the profound difference of their microstructure compared with that of conventionally processed alloys with the same chemical composition. AMed alloys exhibit a high degree of anisotropy in their microstructure caused by the fabrication process itself, which is characterized by highly localized heat input in a brief amount of time, inducing high temperature gradients. Therefore, the solidification structures grow along the largest heat flow direction, which is primarily the build-up direction, leading to an anisotropic microstructure. This has an impact on the mechanical properties of the AMed parts, which exhibit as well an anisotropy as a function of the direction of the load application. As a result, unique effects on machining process performances must be expected.

According to the literature on the subject, it can be concluded that it is still not possible to have a clear insight into the effect of the AM process on machinability for a given alloy. This problem would be overcome if the mechanics of chip formation would be studied in correlation with the microstructural features deriving from the AM process. Therefore, more efforts must be put to investigate how the machinability is influenced by the AM. This Ph.D. research project aims at filling the highlighted gap for what concerns the Ti6Al4V alloy produced via the L-PBF technology.

Chapter 3

Experimental procedure

This chapter describes the experimental procedure adopted for the study of the machinability of the L-PBFed Ti6Al4V alloy. First of all, the main equipment used is reported in detail, namely the AM technologies for the realization of the samples and the machine tools for their post-processing, namely milling and turning. Then, the process parameters and geometries used for the L-PBFed samples, and the cutting parameters of the various machining operations are presented. Finally, the chapter reports the analyses for the characterization of the aforementioned samples.

3.1 Experimental equipment

This paragraph describes the experimental equipment used to manufacture the AMed workpieces and to conduct the machining trials. First, the two L-PBF systems utilized for the samples manufacturing are presented briefly, then the milling center machine and its minimum quantity lubrication system are described, together with the acquisition hardware and software used to measure the cutting forces. Finally, the turning center and its custom-built cryogenic cooling system are presented.

3.1.1 L-PBF machines

L-PBF system for milling samples

The AMed workpieces devoted to milling operations were fabricated by the Italian company SISMA S.p.A. using a MYSINT100 SISMA™ 3D printer [148]. The machine is equipped with a fiber laser with spot size of 30 μm and power up to 200 W, and a Ø 100 mm × 100 mm building volume. All samples were built under argon atmosphere at 3 bar, keeping the oxygen content under 0.3%. The flow of the inert gas is stable and uniform ensuring fusion stability minimizing consumption thanks to a patented system.

L-PBF system for turning samples

The AMed workpieces devoted to turning operations were manufactured by the INFN of Padova using the EOSINT™ M 280 3D system by EOS GmbH [149]. The heating source is a ytterbium fiber laser with a maximum power of 400 W and a focus diameter of 100 μm. The printer is characterized by a building volume of 250 × 250 × 325 mm^3 where the samples were printed in an argon environment.

3.1.2 Micro-milling center

All the milling experiments have been carried out on the high-precision CNC machine center Micromaster™ 5X by Kugler (**Figure 3.1**) for micro-milling operations. The machine has a 250 × 250 × 500 mm^3 workspace and is equipped with an aerostatic spindle able to reach up to 60˙000 rpm vertical axis run-out < ± 1.5 μm. An eddy-current sensor is installed for the online monitoring and compensating of the expansion of the spindle caused by thermal and centrifugal forces. Feed motions are generated by X/Y/Z hydrostatic linear stages with

positioning error < ± 0.3 μm and 6˙000 mm/min maximum linear axis speed. The machine base is made of granite to guarantee high thermal end mechanical stability thanks to its very low thermal expansion coefficient (< 6.5 μm/K) and excellent dumping properties. Moreover, to prevent any possible thermal distortion the machine is placed in an air-conditioned room at 20 °C ± 1 °C in controlled humidity. Finally, to ensure repeatability and precision of the experiments, warm-up cycles were always carried out before the cutting tests, as well as accurate tool setting using an integrated touch-trigger probe by Renishaw™ establishing the location and size of the workpieces.

Figure 3.1: Kugler Micromaster™ 5X high-precision micro-milling center.

The milling center was equipped with an MQL system for the delivery of the cutting lubricant through a precision-jet-nozzle of 0.5 mm of diameter on articulated plastic hose. The flow rate and air pressure of the nozzle were 150 ml/h and 0.70 MPa, respectively. The lubricant utilized for the milling trials was the vegetable-based oil, the Accu-Lube™ LB 5000, which is known to be effective for difficult to cut materials, beside the other MQL benefits, as discussed in Section 2.2.4. The oil mist was supplied to the cutting zone at 50 mm of distance with an angle of about 30°.

Cutting forces measurement system

The cutting forces were recorded using a 3-component piezoelectric dynamometer (type 9119AA2 from Kistler™) specially meant to measure small forces such those in micromachining or superfinishing operations. The dynamometer was connected with a high impedance cable to a charge amplifier with integrated DAQ (LabAmp 5167A from Kistler™). The measuring force range was ± 4kN for each force components with *Fx* and *Fz* sensitivity of about - 26 pC/N and about - 13 pC/N for *Fy*. The acquired cutting force data were then processed on a notebook with the DynoWare™ software. The cutting force measuring chain and set-up is shown in **Figure 3.2**.

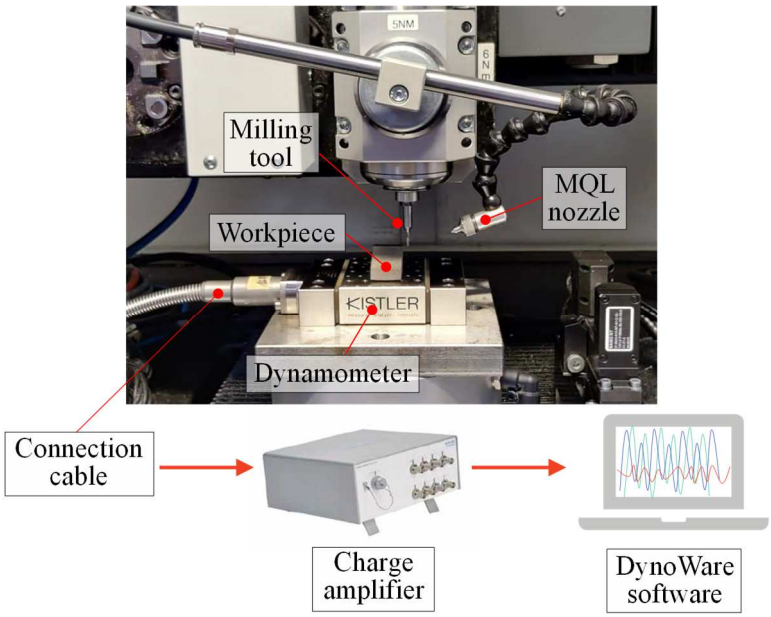

Figure 3.2: Cutting force measuring chain for milling operations.

3.1.3 Turning center

The turning experiments have been carried out on the CNC lathe Mori Seiki™ NL 1500 CNC lathe (**Figure 3.3 (a)**). The machine has a maximum workable diameter and length of 200 mm and 1˙200 mm, respectively. The maximum rotary tool spindle speed is 4˙000 rpm. The lathe is equipped with a conventional cooling lubricant system, i.e. the flood one, and with a specially designed system for cryogenic cooling. The semi-synthetic cutting fluid Monroe™ Astro-Cut HD XBP mixed with water (1:20 mixing ratio) was used in flood cutting and directed to the cutting tool by means of a single nozzle with a flow rate of 400 l/h (**Figure 3.3 (b)**). The cryogenic cooling setup consists of a Dewar flask holding the liquefied nitrogen at high pressure (15 ± 0.5 bar) and low temperature (−192 °C), together with pressure valves and delivery system. The pressure is controlled and regulated at a constant level by means of a pressure control valve and a pressure relief valve installed on the top of the flask. A vacuum insulated tube transports the liquid nitrogen to the lathe turret. The liquid nitrogen is delivered to the cutting zone a mass flow of 54 l/h by means of two external copper nozzles (**Figure 3.3 (c)**) with internal diameter of 0.9 mm, directed on the rake and flank faces of the cutting insert with an angle of 45°.

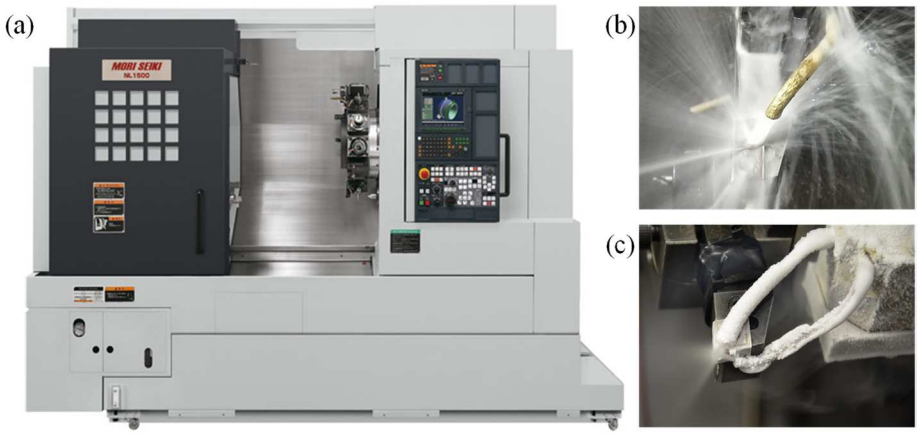

Figure 3.3: Mori Seiki™ NL 1500 CNC lathe (a), photo of the flood (b) and cryogenic cooling (c) delivery apparatus.

3.2 Workpieces material

This paragraph describes in detail the L-PBF parameters used to manufacture the samples for milling and turning trials. All the AMed samples investigated in this work underwent to the same high-temperature heat treatment after the AM process and part removal from the support structures. The heat treatment was executed in an inert argon atmosphere with a heating rate of approximately 6 °C/min up to 950 °C held for 30 min followed by furnace cooling using the RHF™ laboratory furnace by Carbolite Gero Ltd. The heat treatment aimed at stabilize the microstructure, relieve the thermal stresses, reduce the porosities, and improve the mechanical properties, accordingly to what reported in Section 2.1.4. The chosen AM parameters and heat treatment ensured to obtain fully dense parts. In fact, for every sample the density was over 99.9% (± 0.3%), measured using the Archimedes' method.

3.2.1 Samples for milling trials

The L-PBFed samples for milling operations were manufactured with the MYSINT100™ machine described in Section 3.1.1 using the Ti6Al4V grade 5 plasma-atomized powder produced by LPW Technology™ with 15 - 45 μm size range and composition in conformity with that reported in **Table 2.2**. The parts were manufactured using the chessboard scanning strategy with laser power of 105 W, scanning speed of 950 mm/s, hatch spacing and layer thickness of 80 μm and 20 μm, respectively. This led to an overall input volumetric energy density of 69.1 J/mm^3. The prisms were manufactured using 4 × 4 mm^2 squares rotated of 90° from each other and each layer was shifted from the other of 30° on the XY-plane in order to avoid the densification of defects in the same zones and reduce the thermal stresses [50].

Samples with various build-up orientations

To evaluate the anisotropy of AMed parts in flat end milling operations, rectangular prisms (15 × 30 × 10 mm^3) were manufactured with four orientations ranging from 0° to 90° with respect to the horizontal plane of the powder bed as reported in **Figure 3.4**. The four prisms

are named 0deg, 36deg, 72deg, and 90deg to differentiate the manufacturing inclination. The reference system XYZ to refer to is the one shown in **Figure 3.4**.

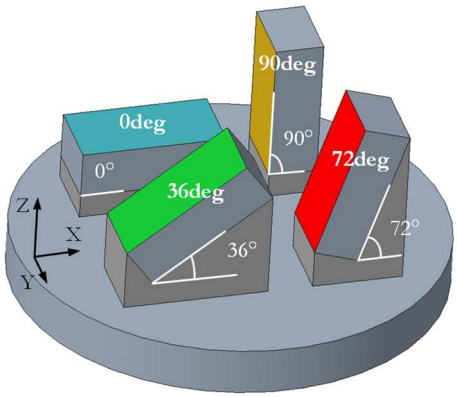

Figure 3.4: L-PBFed Ti6Al4V samples configuration and build-up orientation. The colored face indicates the one that will be machined afterward.

Samples with inclined planes

To evaluate the anisotropy of AMed parts in ball end milling operations, L-PBFed blocks with different plane inclinations were manufactured with the geometry reported in **Figure 3.5**. The growth direction was kept along the height of the blocks (Z-axis). In this study annealed wrought (WR) Ti6Al4V workpieces were also considered as a comparison. This alloy is usually used for aerospace and biomedical applications, fields in which AMed alloys are widely gaining ground. The WR samples were obtained via wire electrical discharge machining from a bar keeping the same geometry of the L-PBFed samples.

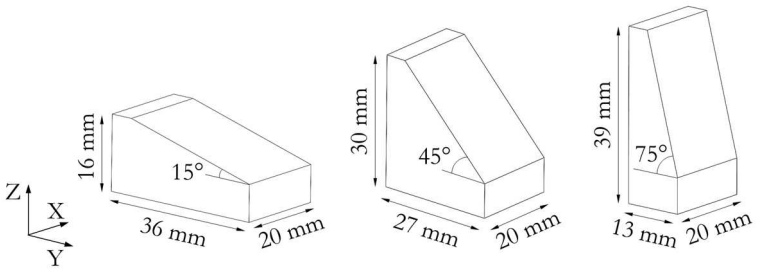

Figure 3.5: Geometry of the AMed and WR workpieces.

3.2.2 Samples for turning trials

The L-PBFed samples for turning operations were manufactured with the EOSINT™ M 280 machine described in Section 3.1.1 using a Ti6Al4V grade 5 powder with composition in conformity with that reported in **Table 2.2**. The L-PBFed samples were manufactured in form of 25 mm diameter cylindrical bars with 60 mm height along the growth direction (Z-axis). The following processing parameters were utilized: 280 W laser power, 1200 mm/s scanning speed, 100 μm hatch spacing, and 30 μm layer thickness. The overall input volumetric energy density was, therefore, of 77.8 J/mm^3.

To evaluate the anisotropy of AMed parts in turning operations the scanning strategy was varied, in particular, the stripes and the chessboard strategies were employed. In the first case,

each layer was composed of 5 mm wide stripes with a scan vector that was rotated by 67° for each successive layer. In the chessboard scanning strategy, the built area was divided into 5 × 5 mm^2 blocks perpendicular to each other with an overlapping of 0.04 mm. Each layer was shifted by 2.5 mm in both the X and Y directions of the scan area.

3.3 Machining trials

In this chapter, details on the cutting parameters of the different machining operations used to evaluate the L-PBFed Ti6Al4V alloy anisotropy are given.

3.3.1 Milling trials

Slotting with flat end mills

To evaluate the effect of the different build-up orientations on the L-PBFed Ti6Al4V machinability, full slots were machined on the upper surface of each specimen (the colored one in **Figure 3.4**). The tests were carried out using the high-precision micro-milling center under MQL conditions described in Section 3.1.2. The testing set-up is displayed in **Figure 3.6 (a)** and a scheme of the milling operation is shown in **Figure 3.6 (b)**.

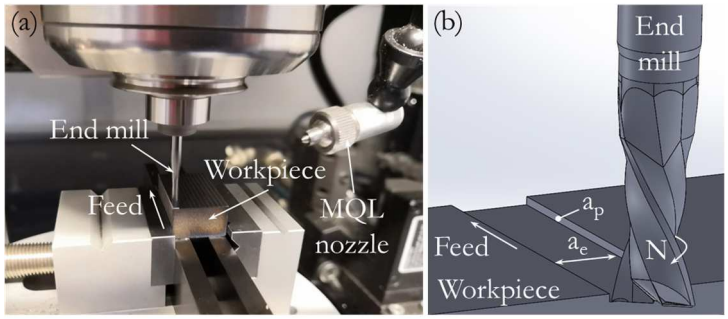

Figure 3.6: Full-slotting milling set-up (a) and scheme of the milling operation (b).

Before executing the slots, the rough superficial layer, typical of as-built AMed parts, was removed to set a ground zero for all the samples. To do so, a milling operation of 0.15 mm depth of cut was performed with a 3 mm diameter end mill, setting 75 m/min and 0.08 mm as cutting speed and feed, respectively. In this way, the initial surface topographies of all the samples were comparable. Since the original 15 × 30 × 10 mm^3 prisms were sectioned for metallurgical and mechanical analyses, the final dimensions of the workpieces used in the milling tests were 15 × 20 × 10 mm^3. The tungsten carbide uncoated double flute flat end mill 2P121-0200-NC H10F by Sandvik™ Coromant was selected for the cutting tests. The end mill has a diameter Ø of 2 mm and a 0.15 mm corner radius R, with 25° of flute helix angle. For each specimen, a new tool was used in order to avoid any influence of adventitious tool wear on the experimental results. Prior to use, each mill cutter was imaged using a FEI QUANTA™ 450 Scanning Electron Microscope (SEM) to inspect the cutting edge radii and verify the absence of any possible production defects, such as damages or micro-cracks. **Figure 3.7** shows the SEM images of the virgin flat end mill geometry.

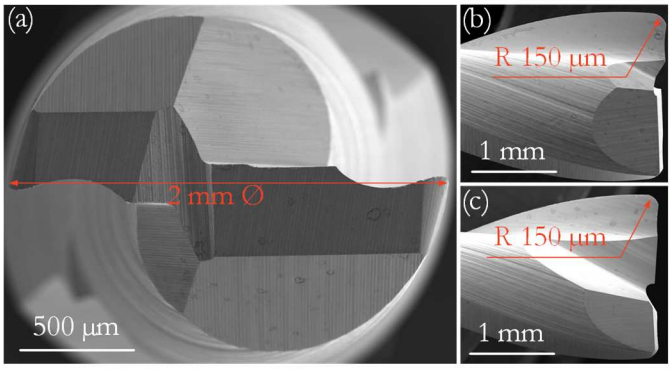

Figure 3.7: SEM images of the cutting tool: top view (a); short tooth (b) and long tooth (c) side view.

The milling process parameters with flat end mills are reported in **Table 3.1** differentiating from the milling tests carried out with Set #1 to assess the tool wear progression, and Set #2 to assess the effect of different cutting parameters on surface finish. The cutting parameters were chosen from the tool supplier datasheet. The depth of cut was kept constant and chosen close to the minimum allowed for the tool geometry. To ensure the data robustness, each machining trial was repeated three times. The limited variation of the collected results proved the good repeatability and reliability of the tests. **Figure 3.8** shows the chosen machining strategy for the full-immersion slotting to assess the tool wear, keeping the cutting parameters constant (Set #1 of **Table 3.1**). The full acceleration at the tool engagement was guaranteed by making the machining operation start sufficiently far from the workpiece. To evaluate how the microstructural anisotropy of the AMed parts affects the machined surface finish, four sets of cutting parameters were considered (Set #2 of **Table 3.1**). Namely, two cutting speed v_c (v_c- and v_c+) and two feed per tooth f_z (f_z- and f_z+) values were chosen at the extremities of the optimal range of values provided by the tool supplier and then combined into four parameters sets. Milling slots were executed with the same cutting direction reported in **Figure 3.8** for the tool wear test. The horizontal (0deg) and vertical-oriented (90deg) samples were considered for these cutting trials.

Table 3.1: Milling tests parameters with flat end mill.

		Set #1	Set #2
Cutting parameter	Symbol	Value	Value
Axial depth of cut (mm)	a_p	0.2	0.2
Radial depth of cut (mm)	a_e	2	2
Cutting speed (m/min)	v_c	75	30 60
Feed per tooth (mm/tooth)	f_z	0.02	0.01 0.05

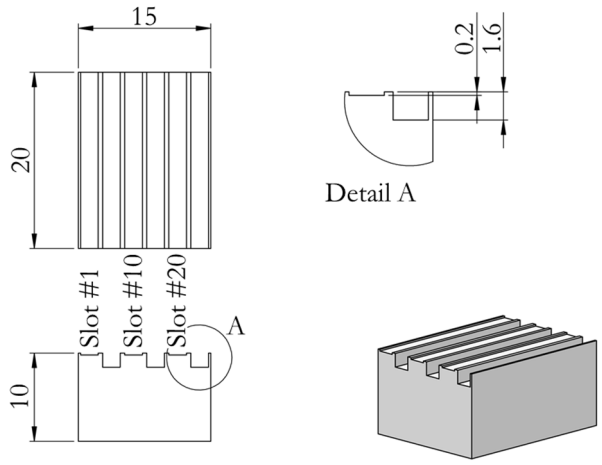

Figure 3.8: Machining strategy for the full-immersion slotting to assess the tool wear.

Machining with ball end mills

To evaluate the effect of the different plane inclinations on the L-PBFed Ti6Al4V machinability, ball end milling operations were carried out on the inclined surfaces of the specimens reported in **Figure 3.5**. The tests were conducted using the high-precision micro-milling center described in Section 3.1.2 under MQL conditions. The testing set-up is displayed in **Figure 3.9**, together with the cutting forces reference system.

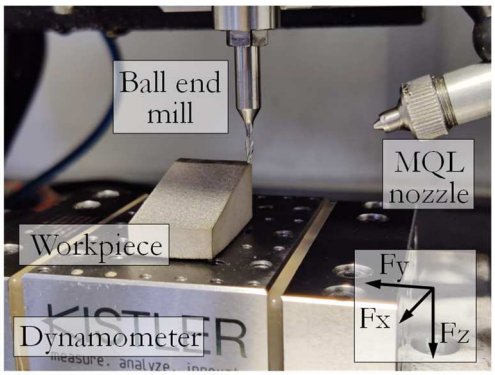

Figure 3.9: Milling set-up with reference system of the cutting forces.

The tools used for the experiments were 2 mm diameter ball nose end mills with two cutting edges made of uncoated tungsten carbide with flute helix angle of 30° (R216.42-02030-AK60A H10F by Sandvik™ Coromant). The overhanging length of the tool was fixed at 27 mm to avoid the workpiece-cutter collision. **Figure 3.10** shows the SEM images of the virgin ball end mill geometry. To prevent the impact of tool wear on the machinability data, for each slot a new tool was used, whose initial integrity was evaluated using the SEM. A roughing operation was performed prior to the execution of the finishing slots. The milling process parameters with ball end mills are reported in **Table 3.2** differentiating from the milling tests carried out wit Set #1 and Set #2, choosing the cutting parameters from the tool supplier catalogue. The Set #1 was selected to assess the effect of different cutting paths on 15°, 45° and 75° inclined planes. The Horizontal Upward (HU) and Vertical Upward (VU) tool paths were utilized for finishing ball end milling on 4 × 4 mm^2 slots in down cutting conditions as

shown in **Figure 3.11**. The Set #2 was selected to assess the effect of different cutting parameters in HU of 45° inclined planes with 4 × 4 mm^2 machining slots. For each workpiece, each cutting condition was repeated three times to ensure the data robustness both on the AMed and wrought Ti6Al4V samples. To evaluate how the microstructural anisotropy of the AMed parts affects the machined surface finish, the 45° inclined surface was considered and HU milling operations were carried out varying the cutting parameters, namely two depth of cut (d15 and d73) and two feeds (f30 and f40) were selected as reported in **Table 3.2**.

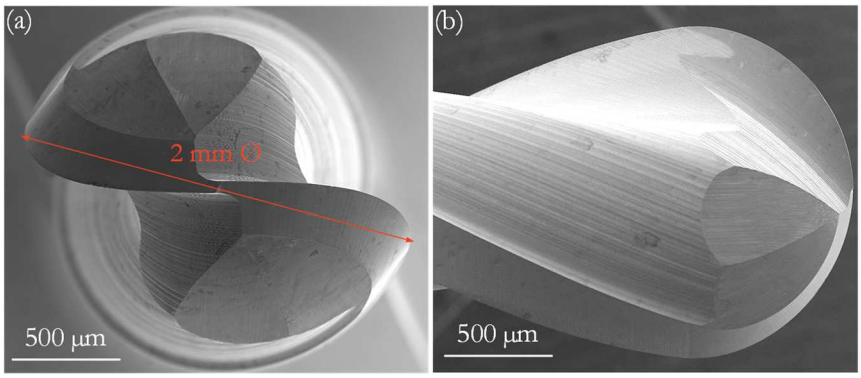

Figure 3.10: SEM images of the cutting tool: top view (a) and side view (b).

Table 3.2: Milling tests parameters with ball end mill.

		Set #1	Set #2
Cutting parameter	Symbol	Value	Value
Depth of cut (mm)	d	0.073	0.015 0.073
Pick feed (mm)	pf	0.1	0.1
Nominal cutting speed (m/min)	v_c	100	100
Feed (mm/rev)	f	0.03	0.03 0.04
Tool path		HU, VU	HU

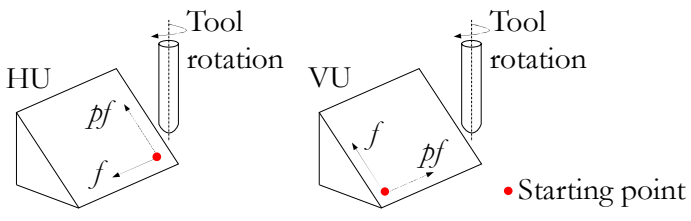

Figure 3.11: Machining strategy for the ball end milling operations. HU and VU cutter path orientations with indication of the tool rotation.

3.3.2 Turning trials

To evaluate the effect of microstructural anisotropy on the surface integrity induced by turning operations, both longitudinal and face turning tests were carried out on the Mori Seiki™ lathe. The machining operations were conducted under both conventional flood and cryogenic conditions as described in Section 3.1.3. In longitudinal turning the tool moves parallel to the rotation axis of the workpiece, whereas, during facing, it moves orthogonally to its axis, as schematically depicted in **Figure 3.12**. This makes possible a different interaction between the cutting tool and the microstructural anisotropy. Turning operations were performed by adopting a PVD TiAlN coated CNMG120404-SM 1105 insert by Sandvik™ Coromant characterized by a rake angle γ of 7° and corner radius R of 0.397 mm (see **Figure 3.13**). A new cutting insert was used for each specimen so to avoid any influence of the tool wear on the experimental results and to isolate the effect of the microstructural anisotropy on the surface integrity results.

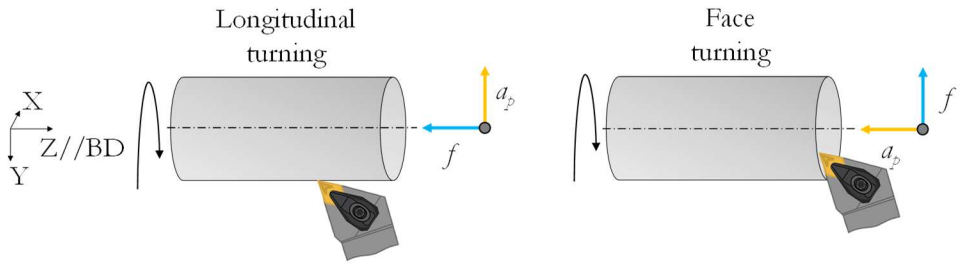

Figure 3.12: Machining strategy for longitudinal and face turning operations. The build-up direction (BD) of the L-PBFed Ti6Al4V is along the Z-axis.

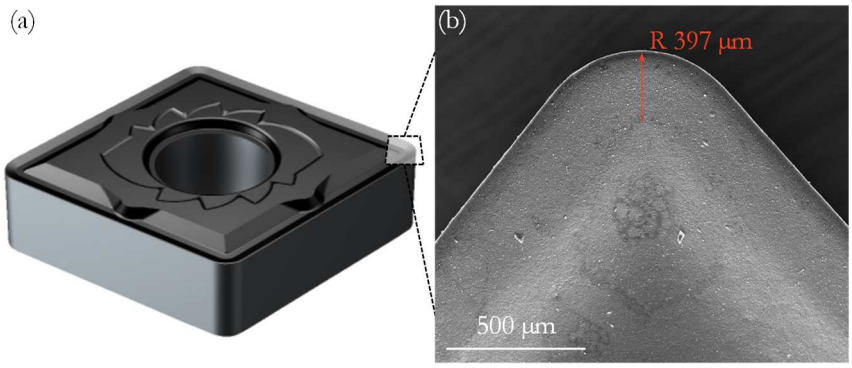

Figure 3.13: Cutting insert image (a) and SEM image of the cutting edge top view (b).

First, a roughing operation was performed with one pass of 0.5 mm of depth of cut and 0.2 mm of feed rate at 80 m/min of cutting speed for both the turning operations. Afterward, a single finishing pass was performed by using the cutting parameters reported in **Table 3.3**, to reach a final diameter of 23.7 mm and a height reduction of 0.65 mm. Both turning operations, i.e. longitudinal and face turning, and cooling conditions, i.e. flood and cryogenic, were applied to samples obtained with different scanning strategy, i.e. stripes and chessboard, for a total number of eight cases. Each parameters combination was employed three times to ensure the data robustness and the average values of all the analyzed data reported with the related standard deviation.

Table 3.3: Turning tests parameters.

		Longitudinal turning	Face turning
Cutting parameter	Symbol	Value	Value
Depth of cut (mm)	a_p	0.15	0.15
Feed (mm/rev)	f	0.15	0.15
Cutting speed (m/min)	v_c	80	80

3.4 Characterization after machining

3.4.1 Microstructural and mechanical characterization

To inspect their microstructure, the L-PBFed Ti6Al4V samples were carefully sectioned at the same height, whenever the geometry of the sample allowed it, by means of an abrasive cut-off wheel. Afterward, the Ti6Al4V pieces were hot mounted, ground using up to 4000 grit SiC paper, and polished with a 1:4 mix of colloidal silica suspension and hydrogen peroxide 30% on a polyester cloth. The metallographically prepared samples were then cleaned with an ultrasonic acetone bath for 15 min, then rinsed in demineralized water, and finally dried with compressed air. Few drops of the Kroll's reagent (1.5 mL HF, 4 mL HNO_3, 94 mL dH_2O) were poured on the Ti6Al4V polished surfaces for 15 s to reveal the grain boundaries.

The microstructure observations were conducted using a DMRE™ optical microscope by Leica equipped with a high definition digital camera. The measurement of the columnar prior β grains width and of the α lamellae thickness was carried out using Matlab™ software on six different micrographs at 50 × and 1000 × of magnification, respectively. The ASTM E112 line intercept method [150] was followed. Ten micrographs at 1000× of magnification were used to measure the extent of the plastically deformed grains in the sub-surface, namely the Severe Plastic Deformation (SPD) layer, every 10 μm via the ImageJ™ software.

Vickers microhardness measurements were carried out using the Durimet™ microhardness tester by Leitz with a load of 50 g or 100 g with 15 s dwelling time, according to specific needs, following the ASTM E92-17 standard [151]. Bulk microhardness was tested in all the material cross-sections through thirty unevenly distributed indentations for each condition. In the case of the cylindrical samples which underwent to turning operations, the nanohardness was considered to assess the material strain hardening related to the lamellae deformation under the cutting forces. The nanohardness was measured using a Berkovich tip of the iMicro™ nanoindenter from Nanomechanics Inc. All the indentations were performed using a load of 30 mN up to 20 μm below the machined surface. For reliable measurement, three 4 × 5 matrices of indentations were performed on each specimen. Rows and columns were spaced 5 μm to each other. The bulk nanohardness was measured as well, performing three 4 × 4 matrices sufficiently distant from the surface, randomly distributed. All the above-

mentioned measurements were recorded to calculate the average values and the respective standard deviations.

3.4.2 Surface quality analysis

Surface defects and topographical analyses

The machined surface micro-morphology and defects were analyzed using the FEI QUANTA™ 450 SEM with the Backscattered Electron Detector (BSED). This mode gives immediate information about the mean composition of the sample, allowing at the same time a good topographical contrast.

The machined surfaces were scanned using the PLU-Neox™ optical profiler by Sensofar with a 20× or 100× Nikon™ confocal objective, as appropriate, with a green LED. Data processing, filtering and evaluation of the surface texture parameters were performed according to the ISO 25178 standards [152]. In particular, the form was removed by selecting a polynomial filter of 1st or 3rd order, depending on the type of sample, i.e. planar or cylindrical, respectively. No other filtering was applied in order to ensure a consistent comparison of the different surfaces, obtained with different cutting parameters. Machined surfaces present a texture that strongly influences their in-service performances [123]. In turn, the parameters considered to be the most significant for the specific case were analyzed and reported. The most noteworthy roughness parameters to characterize a machined surface and its performances in terms of surface topography are reported and described hereafter:

- Amplitude parameters *Sa* (arithmetical mean height), *Ssk* (skewness), *Sku* (kurtosis). The *Sa* parameter is the most common areal parameter, which constitutes a reference for comparison with other research data, generally utilized to estimate the roughness of a surface. The *Ssk* parameter is a measure of the degree of symmetry of the surface heights about the mean plane. An ideal normal distribution has $Ssk = 0$, a surface with a majority of peaks has $Ssk > 0$, whereas when there is a predominance of valleys $Ssk < 0$. This parameter is suitable for describing the load-carrying capacity of a surface and its corrosion tendency. The kurtosis parameter may be used to estimate the presence of peaks or valleys outliers on a surface: a surface with a normal height distribution has $Sku = 3$, whereas a spiky surface has $Sku > 3$ and a bumpy surface $Sku < 3$. This parameter is useful for detecting the existence of either peak or valley defects on the surface.
- Functional parameters *Spk* (reduced peak height), *Svk* (reduced dale height), *Smr1* (peak material portion) and *Smr2* (valley material portion). *Spk* is the mean height of the peaks above the core roughness of the surface, whereas *Svk* is the mean valley depth below the core roughness. The *Spk* parameter depicts the surface sites that are prone to be removed in rubbing surfaces or sites prone to corrosion. The *Svk* parameter is beneficial for distinguishing the presence of potential stress concentration sites or dales where wear debris, a lubricant or a corrosive fluid can concentrate. *Smr1* designates the percentage of material that includes the peak structures associated with the *Spk* parameter. Consistent with *Spk*, *Smr1* represents

the percentage of the surface that is prone to be removed in rubbing surfaces. *Smr2*, which is defined as 100% - *Smr1*, represents the area that includes the deeper valley structures associated with the *Svk* parameter.

- Spatial parameter *Str* (texture aspect ratio) is a measure of the spatial isotropy or directionality of the surface texture. A surface with a dominating lay has a *Str* value of 0.00, whereas a spatially isotropic texture has a *Str* of 1.00.
- Hybrid parameters *Sdr* (developed interfacial area ratio) and *Sdq* (root mean square gradient). Both the parameters are a measure of the spatial complexity of the texture and can be used to distinguish surfaces with comparable *Sa* values. *Sdr* increases with the spatial intricacy of the texture and can find applications concerning surface coatings and adhesion. *Sdq* is a general measurement of the slopes which comprise the surface and find application in sealing systems, surface cosmetic appearance and wettability. For a specific *Sa*, a wider spaced feature may present lower *Sdr* or *Sdq* values than a surface with the same *Sa* but finer spaced texture.

The average values of such areal parameters were reported with the relative standard deviation.

Burrs extent

The SEM BSED was utilized to analyze the morphology of the top burrs in slotting operations. The burrs height was assessed on micrographs at 1000× of magnification of hot mounted slot cross-sections at five different positions along the slot. To measure the burrs height, the image processing program ImageJ™ was utilized. The average values and the standard deviation of ten height measurement for each slot were calculated and reported.

3.4.3 Tool wear analysis

To progressively analyze the tool wear in slotting operations, both the tools and the machined surfaces were examined every 10 slots (i.e. every 200 mm of cutting length) up to their failure, as schematized in **Figure 3.8**. SEM inspection was carried out using both the Everhart-Thornley Detector (ETD) and the BSED to check the worn tools in the same orientations and magnifications used for the virgin ones. To qualitatively characterize the tool wear, the ISO 8688-2 [105] standard for end mills was taken as reference. The material adhered on the worn tools was analyzed by means of the Energy-Dispersive X-Ray Spectroscopy (EDS) technique. Research studies prove that the dominating deterioration phenomena are micro-chipping and adhesive wear in the case of carbide tools that machine titanium alloys [107], as reported in Section 2.2.1. In this case, flank wear width and crater depth, which are commonly utilized as tool-life criteria, may be relatively low even when the tool is near failure [153], or difficult to measure since adhesion occurs. Due to the small size of the end mill utilized, to quantitatively characterize the tool wear, a method commonly used to assess the micro-milling tool wear, i.e. the percentage reduction of the tool diameter, was adopted. In fact, in the case of small cutting tool diameters, the original cutting edges are significantly corrupted by abrasive wear and a new cutting edge may form. The diameter of the circumscribed circle of the top view of the tool

was measured via the ImageJ™ software and the percentage reduction of the tool diameter calculated referring to the measured diameter of each virgin tool, according to literature studies [154,155]. Moreover, an approximate quantification of the total adhered and worn material was carried out using image processing. The SEM image of the top view of the virgin tool was overlaid with that of the tool after the last full slot, highlighting in white the worn zones (i.e. the difference of the geometries of the two overlaid images) and in red the adhesion zones detected with the SEM BSED as shown in **Figure 3.14**. The color histogram of the image thus obtained was utilized to count the number of pixels of the two areas (white: rgb (255, 255, 255) and red: rgb (255, 0, 0)).

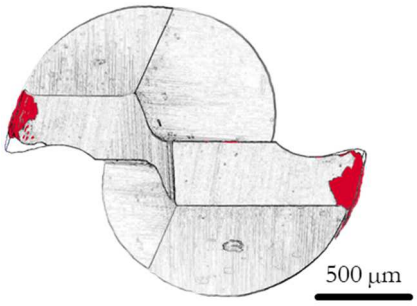

Figure 3.14: Example of the quantification of the total adhered and worn material using the color histogram. White zones represent the worn material, red zones the adhered one.

3.4.4 Chip morphology and cutting forces analysis

The chips were collected at each machining trial and observed under the FEI™ QUANTA 450 SEM with the secondary electron detector, the ETD. The chip lamellae width and chip length were measured using the ImageJ™ software. The mean values of the chip features and the standard deviation were calculated for ten swarfs for each cutting condition.

The cutting forces were recorded in milling operations using the piezoelectric dynamometer described in Section 3.1.2 with a sampling rate of 2.5 kHz in slotting and 10 kHz in ball end milling operations. For each set of cutting parameters, six measurements were carried out, and the resultant cutting force *Fres* was then calculated as follows:

$$F_{res}=\sqrt{F_x^2+F_y^2+F_z^2} \quad (\mathrm{N}) \qquad \text{Equation 3}$$

Chapter 4

Results and discussion

This chapter reports in detail the machinability results and the relative comments of the L-PBFed Ti6Al4V alloy for the machining operations described in Chapter 3. First, surface finish and general microstructural results of the as-built samples under examination are reported by way of example. Then, the machinability evaluations for milling operations are reported in detail, as published by the Author in [156–158]. The results of the turning operations follows, as published by the Author in [159]. At the end of each paragraph concerning a specific L-PBFed workpiece-cutting operation combination, specific conclusions are outlined, which will then be resumed in the Conclusions chapter of this dissertation.

4.1 Preliminary results on as-built L-PBFed samples

In this paragraph the results of some preliminary analyses of the as-built L-PBFed samples are presented. As reported in Section 2.1.5, the as-built surface quality is not suitable for functional surfaces. Typical L-PBFed Ti6Al4V surfaces are reported in **Figure 4.1** for the prisms manufactured at different build-up orientation, namely 0deg, 36deg, 72deg and 90deg. The surface roughness values ranged between 7 and 11 μm in accordance to what found in literature (see **Table 2.1**). The surfaces presented partially melted particles and visible laser scanning paths or layers.

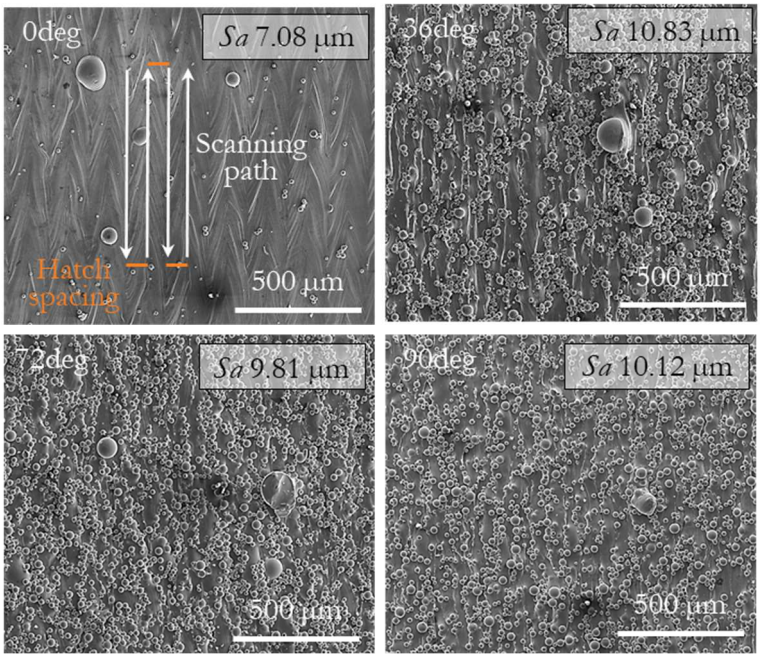

Figure 4.1: SEM images and surface roughness *Sa* of the as-built up-skins surfaces at different build-up orientations. On the 0deg samples the laser scanning path was clear.

Figure 4.2 reports the typical microstructure of the L-PBFed Ti6Al4V alloy. In **Figure 4.2 (a)** a 3D unit is reported which shows clearly the microstructural anisotropy of such parts. **Figure 4.2 (b), (c)** and **(d)** report the microstructure before and after the heat treatment along the build-up direction (BD) of the part. The as-built specimen in **Figure 4.2 (b)** showed a wholly martensitic α′ microstructure and columnar prior β grains developed along the BD, i.e. the direction of the maximum thermal gradient within a melt pool in accordance to the literature

review in Section 2.1.4. The vertical heat flux of the laser beam allowed for the β grains expansion over many layers during the melting phase, and the high cooling rate of the L-PBF process transformed them in acicular α′. More in detail, it was confirmed that the martensitic needles were disposed at about 40°-45° with respect to the BD with a herringbone pattern according to a Burgers relation between the β and α′ phases.

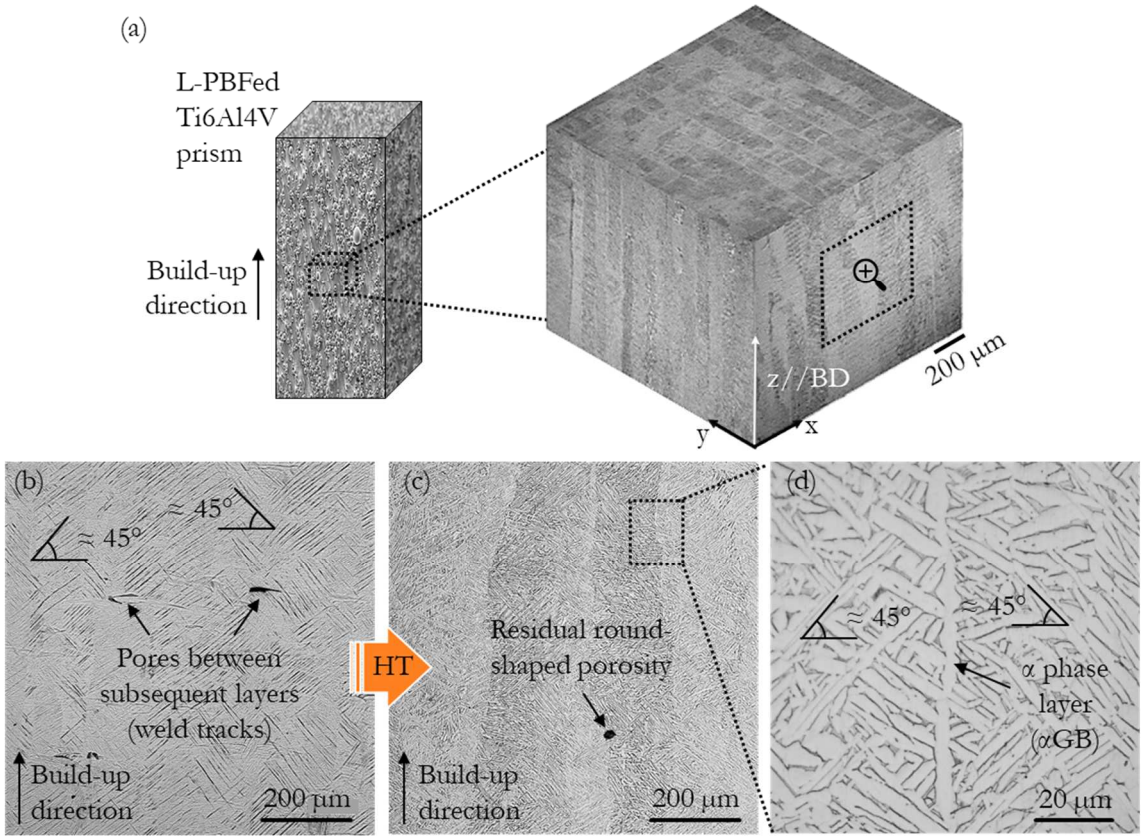

Figure 4.2: Microstructure of the L-PBF Ti6Al4V: 3D representation (a); zoom of the zone highlighted in (a) on the lateral surface before heat treatment (b); after heat treatment (c) and its magnification (d). HT stands for heat treatment.

All the as-built specimens presented defects typical of the L-PBF process such as weld tracks between layers, and randomly allocated round-shaped porosity (see **Figure 4.2 (c)**). After heat treatment, a lamellar mixture of α and β phases was observed inside the columnar prior β grains (see **Figure 4.2 (d)**), where the α phase is light and the β one is dark. The anisotropic microstructure still dominated even if most of the porosities were closed. Along the prior β grains boundaries, continuous grain boundary α layers, the αGBs, formed, as shown in **Figure 4.2 (d)**, which is symptomatic of the diffusive nature of the β-α transformation.

4.2 Machinability in milling operations

4.2.1 Slotting with flat end mills – tool wear

Specific microstructural and mechanical considerations

Figure 4.3 reports the L-PBFed Ti6Al4V microstructures along the XZ plane as a function of the different build-up orientations after heat treatment. Each image shows that the prior β grains are aligned along the BD. Such epitaxial growth of columnar β grains is attributed to the thermal gradient throughout the workpiece, as previously described. The prior β grains appears alternatively dark and light due to the different α lamellae orientations.

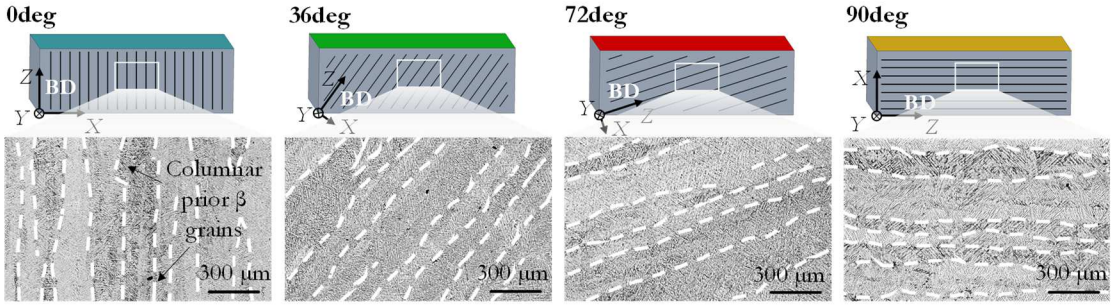

Figure 4.3: L-BPF Ti6Al4V microstructures of the lateral (XZ plane) surface as a function of the different build-up orientations after heat treatment.

The prior β grains width size distribution histograms and their average value for the different samples are presented in **Figure 4.4**. The mean prior β grains width gradually increases with the inclination angle, from 96.1 ± 50 µm for the 0deg sample to 106.2 ± 60 µm for the 36deg sample and further to 131.2 ± 69 µm for the 72deg sample. For the 90deg sample, the β grains width settles to a value closer to the one of the 36deg sample. It is worth noting that the high standard deviation relative to the average value is the result of the large size distribution reported in **Figure 4.4**. These findings show that the prior β grains width is strictly correlated to the build-up orientation, thus governing the anisotropy of the AMed components.

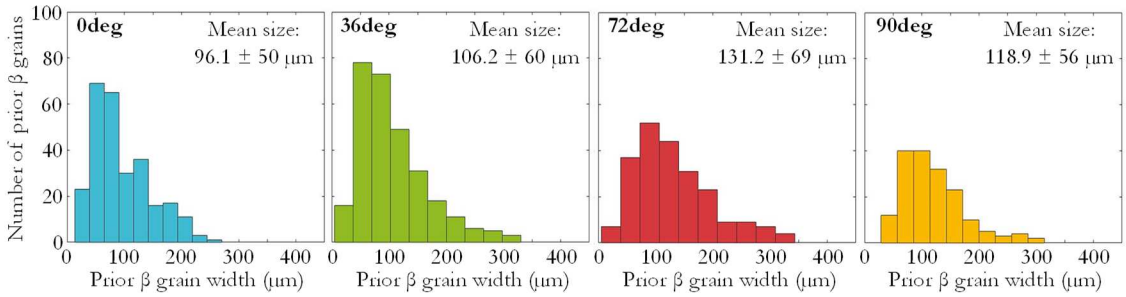

Figure 4.4: Prior β grains width size distribution histograms and their average grain size as a function of the different build-up orientations.

As reported in Section 2.1.4, the lower the cooling rate of the AMed part during its fabrication, the higher the β grains width. This means that the different build-up orientations of the L-PBFed Ti6Al4V samples led to a different heat losses mechanism at a certain height from the

base plate. In particular, the cooling rate lowered with the increase of the inclination angle since the numbers of the subsequent deposited layers increased, in accordance with the fact that the heat accumulates at increasing numbers of the deposited layers [14]. This would have brought the 90deg sample to have the widest prior β grains since it is the sample with the higher number of layers. However, this was not verified due to the predominant influence of its lower layer area that favored the heat loss. From the literature review reported in Section 2.1.4 it was found that the prior β grains play a key role in determining the mechanical response of the AMed workpieces. In fact, as previously described, the β grains are often surrounded by an αGB layer, which acts as a weak junction point where failure may preferentially occur. Moreover, there is a direct correlation between the prior β grains width and the one of the α lamellae at their inside, i.e. high β grains width corresponds to high α lamellae thickness. Finally, the latter controls the mechanical properties of the AMed part through the Hall-Petch relation.

Table 4.1 reports the α lamellae thickness and the microhardness values of the L-PBFed Ti6Al4V samples as a function of the build-up orientation. The α lamellae thickness was well related to the width of the β grains, in agreement with what reported literature. The correlation between the α lamellae mean thickness and the microhardness was found to be quite good (R^2=0.64), even if a stronger correlation was found in [96]. The average microhardness of the 36deg and 72deg samples settled to lower values compared to the one of the 0deg sample, in agreement with the prior β grains and α lamellae size. In fact, the α lamellae are slightly thicker for the 36deg and 72deg samples compared to the 0deg ones. On the contrary, the microhardness of the 90deg sample approached the one of the 0deg sample, being the α lamellae thickness comparable if the standard deviation is considered. This may be related to the particular cooling conditions of the 90deg sample that was previously pointed out.

Table 4.1: Thickness of the α lamellae and microhardness as a function of the build-up orientation.

	Sample			
	0deg	36deg	72deg	90deg
α lamellae thickness (μm)	2.22 ± 0.88	4.61 ± 0.67	6.23 ± 0.74	3.06 ± 0.69
Microhardness ($HV_{0.1}$)	372 ± 20	337 ± 10	348 ± 12	376 ± 22

Tool wear results

Tool wear tests were conducted using the cutting parameters reported in **Table 3.1**. **Figure 4.5 (a)** displays the tool wear progression for the four AMed samples as a function of the cutting length, whereas **Figure 4.5 (b)** shows the SEM images of the tools teeth at the last monitored slot compared with the original edges highlighted in red. The results indicate that tool wear increased at increasing build-up orientation of the samples. In general, the tool wear curves, regardless of the orientation of the samples, can be divided into the three conventional zones, namely: (i) rapid initial tool wear, (ii) uniform tool wear, and (iii) accelerated tool wear, as reported in Section 2.2.1. In fact, the tool wear rapidly increased at the first 200 mm of cutting length for all the samples, settling at tool diameter reductions between 2.7% and 3.7%. After the next 200 mm, in all the cases a nearly steady state of the tool wear was observed, represented by the plateau of the wear curves. Subsequently, the 90deg and 72deg samples

brought to a rapid increase of the tool wear (slope ~ 7), whilst the 0deg and 36deg samples showed a wear increase with a halved slope (~ 3). Whereupon, the curves started to have different trends depending on the orientation of the AM-induced anisotropy even if maintaining the general ranking. At 1 m of cutting length, the tool diameter reductions were 3.7% for the 0deg sample and 7.5% for the 90deg sample, being the other two in the middle. The catastrophic failure of the tool that machined the 90deg sample occurred at 1.08 m of cutting length, which is 29%, 35% and 40% lower than the cutting length reached when machining the 72deg, 36deg and 0deg samples, respectively, revealing that the effect of the build-up orientation on the machinability of the AMed Ti6Al4V is substantial.

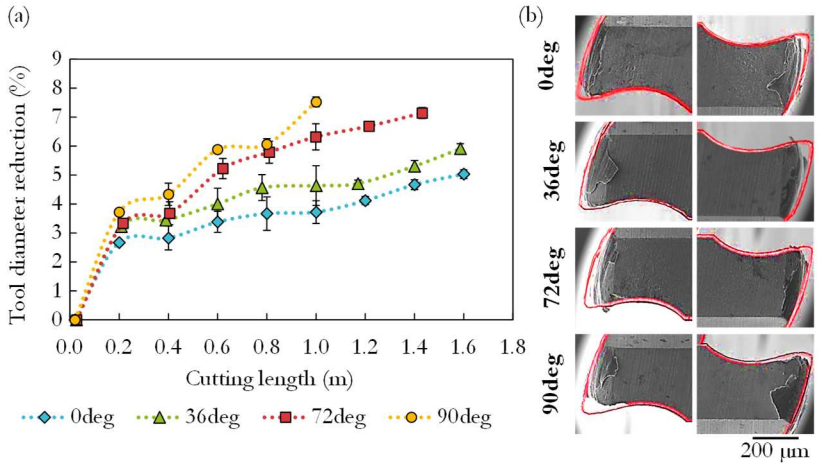

Figure 4.5: Tool wear curves as a function of the cutting length (a) and SEM images of the tools teeth top view at the last monitored slot compared with the original edges highlighted in red (b).

Figure 4.6 shows the SEM images, detected with both the ETD and BSED, of the teeth faces that machined the 0deg and 90deg samples, as the most representative. The tool wear phenomena were principally abrasion, attrition, and adhesion. Abrasion was caused by tooth rubbing against the workpiece material, leading to material loss at the tooth edges, which mainly changed the cutting edge profile. The rough and irregular zones on the teeth faces are primarily caused by the mechanical detachment of tungsten carbide grains by both the chip and workpiece material, which is the so-called attrition. This wear mechanism is triggered by a confined tensile stress state on the tool caused by the chip flow during interrupted cutting [160,161]. The stair-formed face wear, together with flaking and micro chipping, were the main detected tool material loss phenomena and occurred extensively in both the short and long teeth of all the milling tools, particularly when machining the 90deg sample, in agreement with the wear curves of **Figure 4.5 (a)**. Nevertheless, the principal wear typology was adhesion as observable from the SEM BSED images of **Figure 4.6 (a)**. The different compositions of the elements present on the tool face are reported in the EDS spectra of **Figure 4.6 (b)**. The dark (1) zones are representative of the main chemical elements of the Ti6Al4V alloy, whilst the light (2) zones of the tool material.

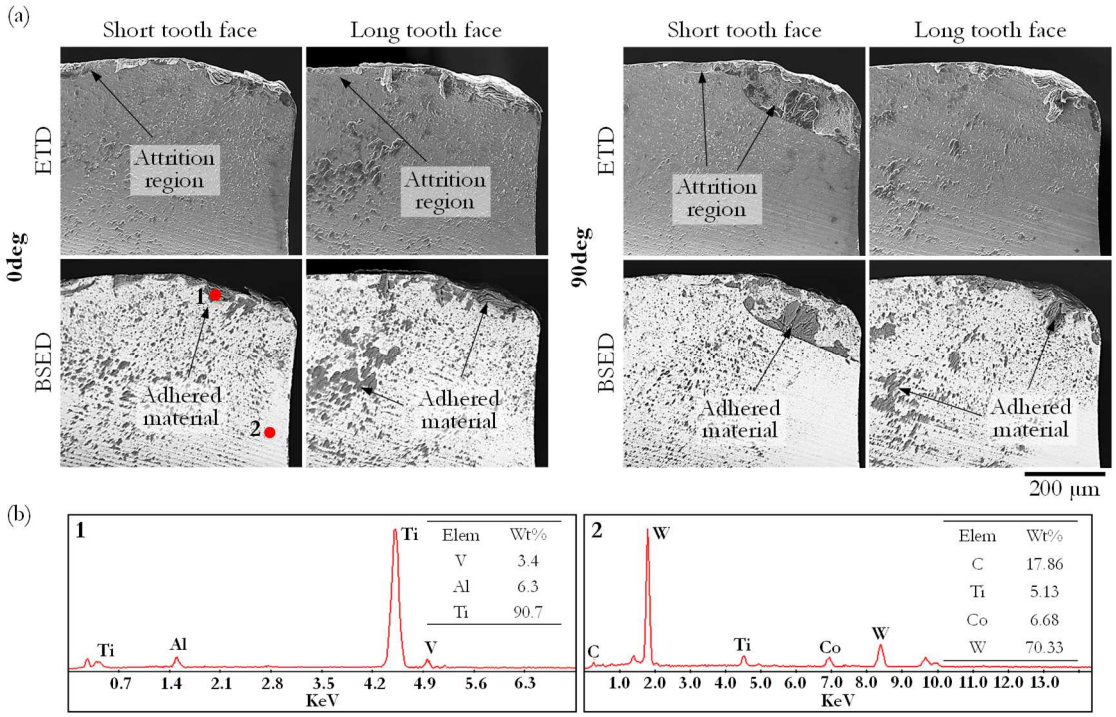

Figure 4.6: SEM images detected with ETD and BSED of the short and long tooth faces of the milling tools after machining the last monitored slot of the 0deg and 90deg samples (a). Representative EDS spectra of the dark (1) and light (2) zones (b).

Based on the image processing described in Section 3.4.3, **Figure 4.7 (a)** shows the relative percentage of adhesion and abrasion tool wear mechanisms of the tools after machining the last full slot. **Figure 4.7 (b)** report an example of the images processed to quantify the two mechanisms with the color histogram at different build-up orientations. It is worth noting that abrasion was always less than adhesion, and it gradually increased going from the 0deg to the 90deg samples. The occurrence of a high amount of adhesive wear is typical of titanium alloys, which present a chemical affinity with elements present in tool materials such as carbon, cobalt and tungsten, as found in the literature review. The amount of adhered material varied during the cutting length progression since detachment of the adhered material arose as it is observable from **Figure 4.8 (b)**. In **Figure 4.8** the tool wear progression in terms of tool diameter reduction and burrs extent is shown. After the first full slot (L_0), regardless of the samples build-up orientation, no changes in the tool geometry were evident and the burrs were tiny and not visible to the naked eye. At half lifetime of the tool ($L_f/2$), both abrasion and adhesion occurred in large amount, the former shown by the tool diameter reduction. This reflected also on the burrs extent that increased significantly, especially in the down-milling side. This phenomenon is related to slotting process dynamics. As the tool engages the workpiece, the chip thickness starts at zero thickness and increases up to the maximum at the middle line of the slot (up milling side of the slot). Once the maximum chip thickness is reached, it decreases reaching zero at the exit point (down milling side). In the down milling side, the chips are disposed behind the tool and the uncut material is pushed out generating large and irregular burrs on this side [162]. At the final full slot (L_f), the burrs amount and extension increased dramatically, as a consequence of the reduced sharpness of the tool caused

by both abrasive and adhesive wear. The reduced sharpness of the cutting edge, in fact, avoided the complete break off of the chips that stacked at the edge of the slots [163].

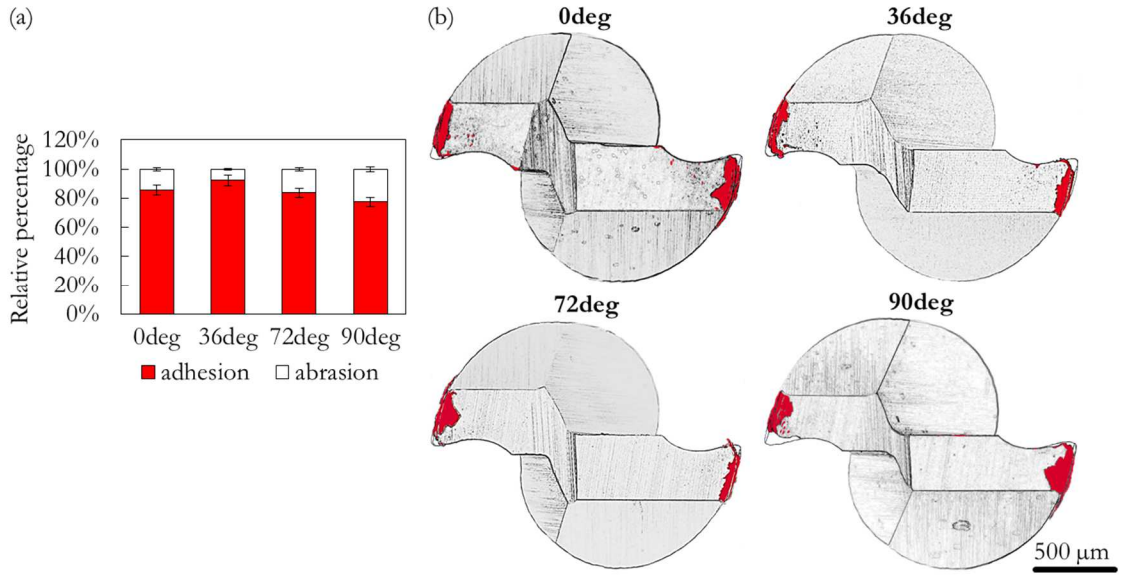

Figure 4.7: Relative percentages of adhesion and abrasion tool wear mechanisms (a), and the images processed to quantify the two mechanism with the color histogram at different build-up orientations (b).

Machined surface topography and quality

To assess the effect of the AM-induced anisotropy on the machined surface finish and its variation with the tool wear, the surface roughness *Sa* of the bottom surface of the first L_0 and last L_f slots were considered and displayed in **Figure 4.9 (a)**. The roughness values of the first slots well correlate with the hardness values above commented. In fact, harder surfaces generally lead to higher surface roughness [117]. Overall, the surface roughness of the machined surfaces increased with the increase of the tool wear, except for the 90deg sample. In the latter case the *Sa* value of the last slot was about the half of the initial one due to the high damage that the cutting edge underwent: the tool wear led to the cutting edge radius increase (as can be seen in **Figure 4.8 (b)**) reducing the tool sharpness, which, in turn, induced the decrease of the feed marks heights. On the other hand, when machining the other samples, the tool wear was lower, avoiding a significative tool geometrical modification and thus not exceeding the limit after which the roughness started to decrease.

To better understand the roughness evolution of the machined surfaces at varying tool wear, **Figure 4.9 (b)** reports the *Sa* values for all the analyzed slots of the 0deg and 90deg samples and the related tool wear curves. It is worth noting that the roughness of the 90deg sample increased gradually with the length of cut till 0.8 m, whereas the next 200 mm led to an increase of tool wear (accelerated tool wear before catastrophic failure) that resulted in the already mentioned *Sa* decrease. For what concerns the 0deg sample, the *Sa* values increased gradually following the trend of the tool wear curves. In this case, the tool reached the catastrophic failure before assessing the surface roughness decrease. The obtained results demonstrate indeed the strong correlation between the tool wear and surface finish, showing that the latter decreases with the increase of the tool wear.

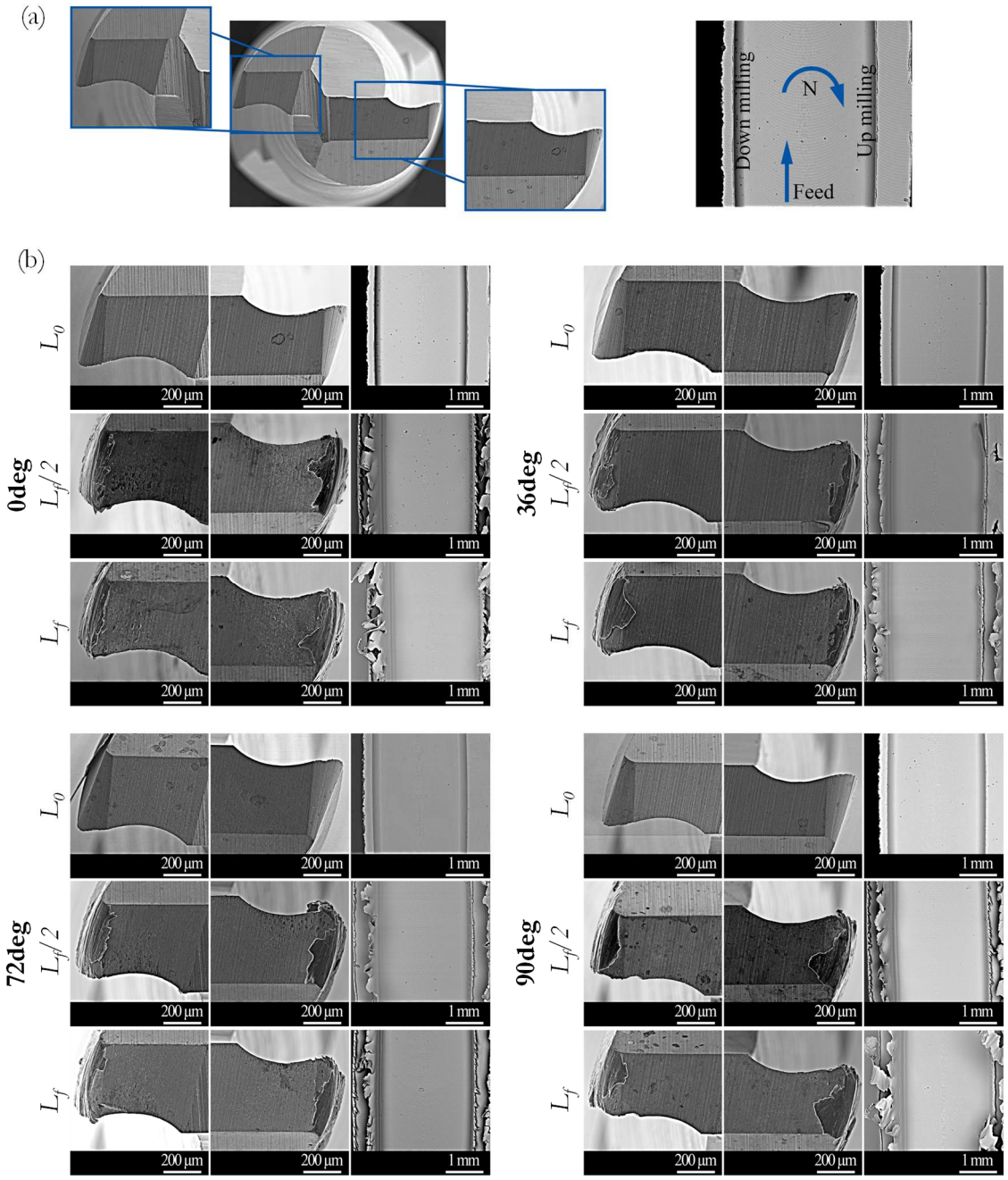

Figure 4.8: Tool wear evolution in relation with the burrs extent. Three different cutting length are showed for each tool at L_0, $L_f/2$ and L_f.

In **Figure 4.10** the SEM images of three zones of the machined surfaces (i.e. down milling side, up milling side and slot center) for the 0deg and 90deg samples are reported. Surface defects were rarely found at the first slot L_0. At the center of the slot, feed marks can be principally seen with very little smearing and few particles of adhered material. At the down and up milling sides, a surface characterized by ripples and tool feed marks was observed due to the continuous change of the cutting mechanisms during the milling process [164]. In fact, at the tool engagement and disengagement points, the chip barely forms because of the low uncut chip thickness, so the workpiece material is removed under plastic or elastic deformation (ploughing cutting mechanism). However, when the cutting edge advances into the material,

the minimum chip thickness is reached and a shear band forms progressively along the tool-rotating track (shearing cutting mechanism). At the last slot L_f, smeared feed marks and adhered material, mainly chips debris, were always present on the machined surfaces, regardless of the slot zone. In particular, the 90deg sample was characterized by the highest amount of defects because of the highest tool wear extent. The down milling side did not experienced variations with respect to its status at L_0, while the up milling side drastically changed. In the latter case, a continuous edge of scales was found on the shoulder of the slot. This high surface irregularity may be caused by high cutting forces and tool vibrations that usually rise when the tool wear reaches the zone (iii) of the tool wear curve before the catastrophic failure.

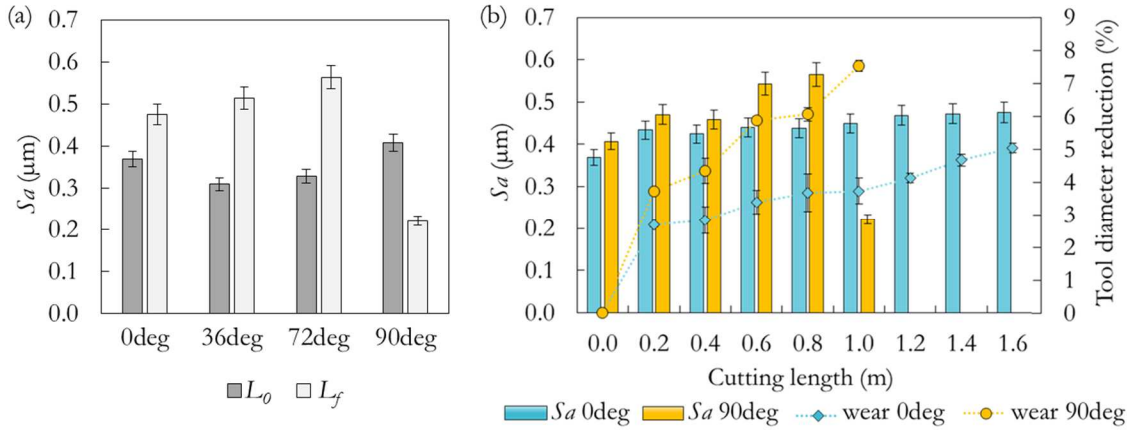

Figure 4.9: Surface roughness *Sa* at L_0 and L_f as a function of the samples build-up orientations (a) and *Sa* values and tool wear curves at increasing length of cut for the 0deg and 90deg samples (b).

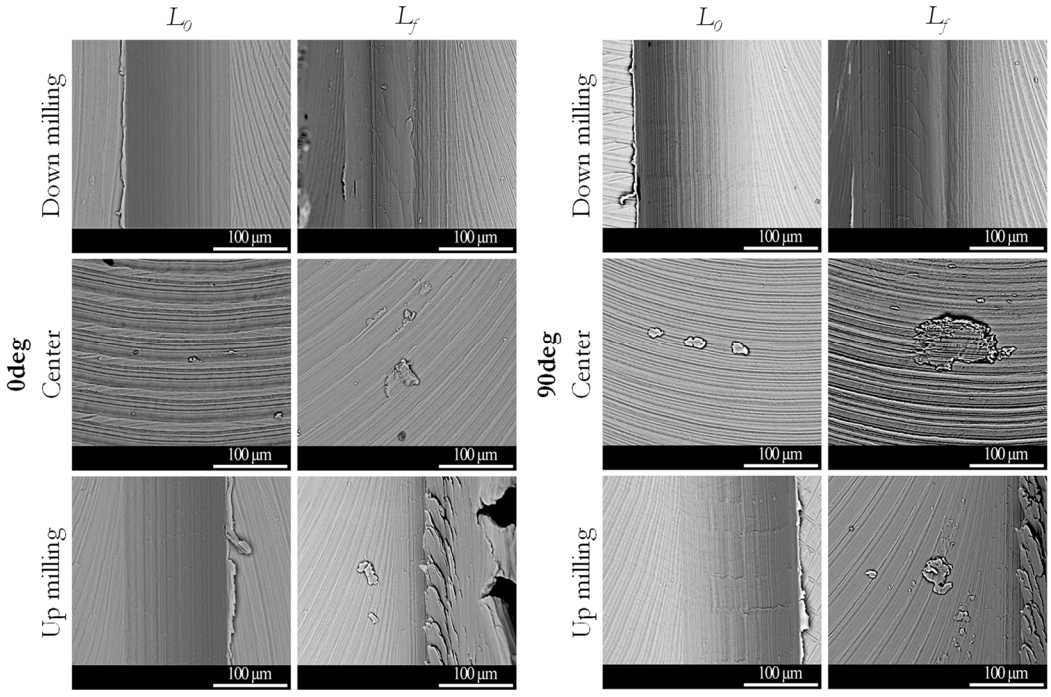

Figure 4.10: SEM images of down milling, up milling and slot center zones of the 0deg and 90deg samples at L_0 and L_f.

Chip morphology and cutting forces

Lamellar ribbon-like chips with faint serration were always obtained in the first slot L_0 as shown in **Figure 4.11**, indicating the prevalence of the shearing mechanism during the cutting process [110]. The free surface of the chips was characterized by fine and close-packed lamellae developed along the chip width. The chip contact surface was more regular, with shallow grooves parallel to the chip length caused by the scratching action of the hard carbide particles embedded in the tool metal matrix. The chip length at the first slot was compliant with the radial depth of cut that is the tool diameter length. The chip thickness was symmetrical with respect to the center line of the slot, being thinner at the edges and growing progressively to the center where the maximum thickness reached that equal to the feed per tooth. For what concerns the chips width, the measured value was higher than the depth of cut. This can be attributed to the fact that, during the cutting process, the metal forming the chip flows towards the two free sides, being compressed in the cutting direction by the tool rake face [165]. Chips that formed at increasing tool wear (see column L_f in **Figure 4.11**) were shorter and ripped in two because of the great rubbing and shearing action of the damaged cutting edge. At increasing cutting length, the cutting edge radius increased and the plastic deformation of the chip under the cutting forces was more intense. This can bring either to more grooved chip contact surfaces and marked ridges and serration as for the 0deg and 90deg samples, or to thin and flat chips as for the 36deg and 72deg samples. Another relevant geometrical characteristic of the chip is its curling degree, indicative of the material behaving as a bi-metallic spring due to the thermal gradient between the chip sliding surfaces and the free one. **Figure 4.11** shows that no sensible difference in the chip curling degree is visible at L_0, according to the presence of negligible wear, regardless of the sample build-up orientation. On the contrary, at L_f, curler chips were obtained when machining the 90deg sample due to the higher temperatures arisen as a consequence of the severe wear. Especially in this case, in fact, powdery chips were formed, suggesting the predominance of the ploughing mechanism in agreement with the tool wear results.

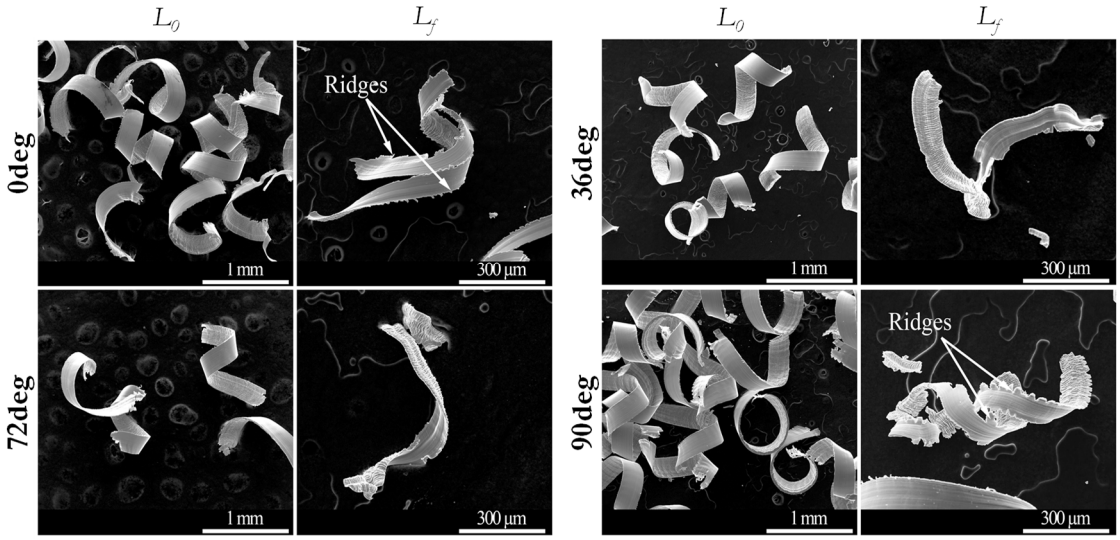

Figure 4.11: SEM images of chip morphology evolution from L_0 to L_f.

Analyzing the swarf at a higher magnification, a distinction between the chips produced machining the 0deg and 90deg samples was observed, as visible in a representative case in **Figure 4.12 (a)**. The chip thickness at the chip center is slightly higher in the case of the 90deg sample with respect to the 0deg one, meaning that the chip compression ratio in the case of the 90deg sample was higher, hence higher the cutting power [166]. Consequently, the shear plane angle Φ at the primary shear zone, highlighted in white in **Figure 4.12 (a)**, is lower for the 90deg sample, which is an index of higher cutting forces [113]. This was confirmed by the cutting force measurements carried out at a later stage, when machining the 0deg and 90deg samples at L_0, as reported in **Figure 4.12 (c)**. The residual cutting forces were 26.91 ± 0.80 N and 31.33 ± 0.43 N for the 0deg and 90deg samples, respectively. Thus, the average cutting force is 16% higher in the 90deg sample than in the 0deg one. These results agree with the tool wear results, being the tool life lower when machining the 90deg sample.

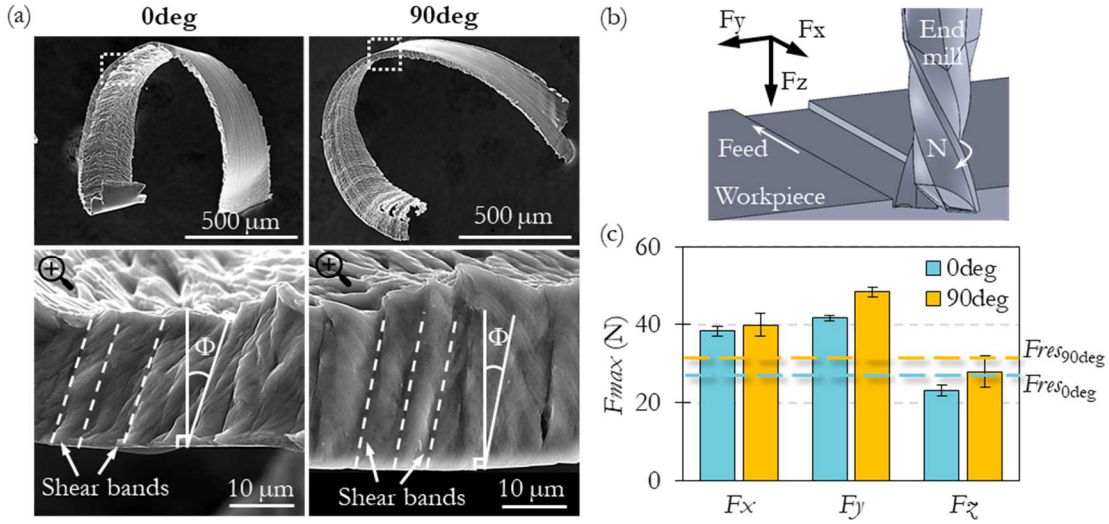

Figure 4.12: Chip morphology and magnified image of the chip thickness of the 0deg and 90deg samples at L_0 (a); cutting force reference system (b); maximum cutting forces *Fmax* plot of the 0deg and 90deg samples at L_0 with indication of the corresponding residual forces *Fres* (c).

Tool-workpiece interactions

The tool wear depends on a range of variables among which the workpiece and tool material, tool geometry, cutting parameters, and cooling conditions are the most significant, as reported in Section 2.2.1. Since in the machining tests carried out in this work, all the above-mentioned characteristics were kept constant, the different tool wear trends can be attributable just to the workpiece material. Thus, to better correlate the tool wear with the AM-induced material anisotropy, microstructural considerations are mandatory. As already reported, after the heat treatment, an αGB layer developed along the prior β grains, representing a discontinuity of the microstructure and a weak point along which cracks may develop. **Figure 4.13 (a)** shows the direction of the cutting process with respect to the αGB layers for the 0deg sample, which showed the lowest tool wear. When the end mill rotates, it progressively engages the material with the so-called registration angle $\varkappa$, which, for the end mill utilized in this work, approaches 90°. The orientation angle of the αGB layers relative to the registration angle for

the 0deg sample is shown in **Figure 4.13 (b)** and, in this case, the two angles correspond, giving a *positive* interaction. This facilitates the chip formation and thus the material removal, reducing the forces acting on the cutting edge and increasing the tool life. For the 90deg sample, the situation is opposite, since the prior β grains, thus the weak αGB layers, are oriented horizontally with respect to the registration angle. Based on the same reasoning, for the 36deg and the 72deg samples, the situation is intermediate. The tool wear curves can be also explained considering the prior β grains width discussed above. In fact, the probability that the tool cutting edge, when rotating, encounters favorably an αGB layer, is higher for the 0deg sample than for the others, being the prior β grains width lower.

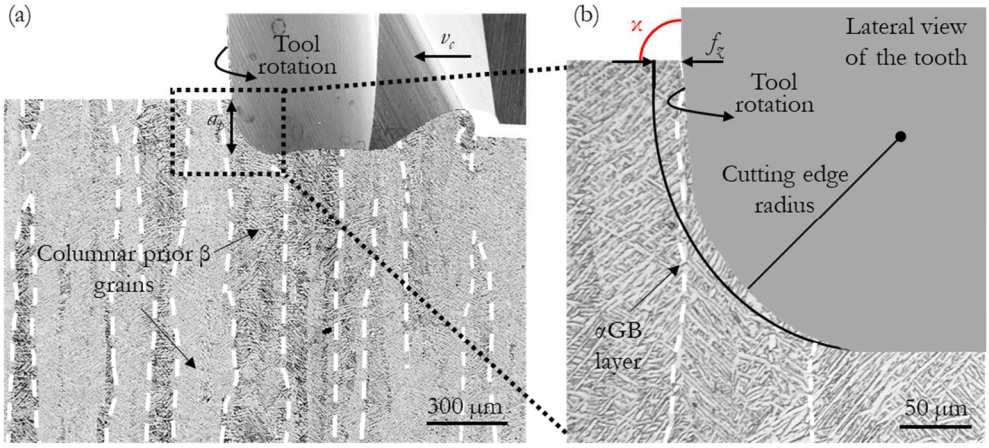

Figure 4.13: Tool engagement with respect to the prior β grains orientations for the 0deg sample (a), and zoomed picture showing the orientation angle of the αGB layers relative to the cutting tool registration angle $\varkappa$ (b).

Conclusions

The principal findings can be summed up as follows:

- L-PBFed Ti6Al4V specimens presented preferred grain growth direction along the build-up direction regardless of the manufacturing inclination angle. This induced a microstructural anisotropy that remained after the heat treatment.
- The different build-up orientations greatly affected the cutting tool wear because of the different orientation angles of the αGB layers relative to the registration angle of the tool. In particular, the tool life decreased gradually, up to 40%, going from machining the 0deg sample to the 90deg one.
- The tool wear caused a proportional increase of the surface roughness, except when the increase of the worn cutting edge radius, experienced when milling the 90deg sample, led to the ploughing mechanism, resulting in a smoother surface.
- The machined workpiece quality in terms of burrs presence and surface defects worsened with the tool wear increase. Specifically, the burrs extent increased progressively with the tool wear as well as the frequency of the adhered material on the machined surface. The combination of the two effects caused a general worsening of the machined surface quality.

- For all the build-up orientations of the samples, lamellar ribbon-like chips were obtained that shortened and ripped in two at increasing tool wear. Detailed chip morphology analysis was compliant with the tool wear results, being the shear plane angle of the chips of the 90deg sample lower than the one of the chips of the 0deg one.
- The cutting force measurements confirmed the tool wear results being 16% higher when machining the 90deg sample than the 0deg one.

4.2.2 Slotting with flat end mills – effect of different cutting parameters

The machinability in slotting operations with flat end mills was further investigated on the 0deg and 90deg samples, focusing on the surface finish. For this purpose, the feed per tooth and the cutting speed were varied (f_z+, f_z-, v_c-, v_c+) as reported in **Table 3.1**.

Surface texture and topography

For this study three topographies at the center of each slot were acquired every 10 mm using the 100× objective. The measured area of each optical profilometry was 455.9 × 448.8 μm^2. A wide range of areal roughness parameters was considered, belonging to all the different classes, such as height (*Sa*, *Sq*, *Sku*, *Ssk*, *Sp*, *Sv*, *Sz*), functional (*Sk*, *Spk*, *Svk*, *Smr1*, and *Smr2*), spatial (*Sal*, *Str*, and *Std*) and hybrid (*Sdq*, *Sdr*). Only the most relevant areal parameters will be hereafter discussed, after a preliminary evaluation via a DoE approach based on a two-factors, three-levels full factorial experimental plan. As expected, the cutting parameter that, in general, influenced the most the surface texture was the feed per tooth.

The arithmetical mean height *Sa* (see **Figure 4.14**) resulted to be about 255% higher on average for surfaces machined with f_z+ rather than with f_z-. In both cases, the 90deg samples presented a slightly higher *Sa* than the 0deg samples. The effect of the cutting speed on this parameter was much lower than the one of the feed per tooth: *Sa* increased by 11% on average going from v_c- to v_c+. The latter affected *Sa* in conjunction with the cutting speed: at v_c- *Sa* was greater for the 90deg sample than for the 0deg one, while at v_c+ the opposite was observed. The great difference in *Sa* values among surfaces machined with different f_z is attributable to the mechanics of chip formation, as reported in Section 2.2.2.

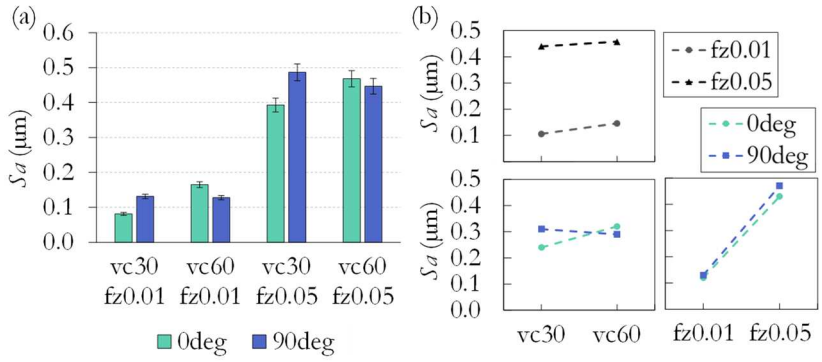

Figure 4.14: Arithmetical mean height *Sa* of the milled samples (a) and interaction plots of fitted means (b).

In fact, the higher the feed marks, which are spaced apart as much as the feed per tooth, the lower the density of peaks and the higher their height. Generally, an increase of the cutting speed in face milling improves the surface quality which, however, was not verified as a rule in the present work. This can be attributed to the fact that the 100% engagement of the end mill hindered part of the cooling action of the lubricant, leading to a rise of the cutting temperature that is known to deteriorate the surface quality. Moreover, at higher cutting speed, the cutting temperature usually increases due to the increased tool-workpiece interactions, which are known to trigger additional friction which converts into heat improving the plastic deformation of the workpiece material [24]. This allowed for the formation of higher peaks as confirmed by the measured values of the reduced peak height parameter *Spk* (see **Figure 4.17 (a)** and **(b)**). The higher *Sa* observed at v_c- for the 90deg samples compared to the 0deg ones is due to the different interaction between the cutting edge and the αGB layers. In the 0deg samples the α layers, which help the material removal during cutting, are favorably oriented with respect to the tool cutting edge, as was discussed in Section 4.2.1. Thus, at the microscopic level, the 90deg samples act as a material with higher shear strength with respect to the 0deg ones, which has been corroborated by the cutting force measurements reported in **Figure 4.12 (c)**. This should bring to higher surface roughness, i.e. to higher *Sa* values [117], as actually occurred. The increase of the cutting speed allowed for a slight (up to 8%) reduction of the surface roughness only for the 90deg samples. For these samples, an increase in the cutting temperatures may have favored the alloy machinability that was lower than that of the 0deg samples because of the αGB layers orientation. **Figure 4.15 (a)** and **(b)** presents the comparison of the different surface topographies of the two build-up orientations when machining with the same cutting parameters. The higher cutting resistance of the 90deg samples was corroborated by the double peak of the feed marks that formed on the surfaces machined with the with v_c- and f_z+, reported in **Figure 4.15 (c)**.

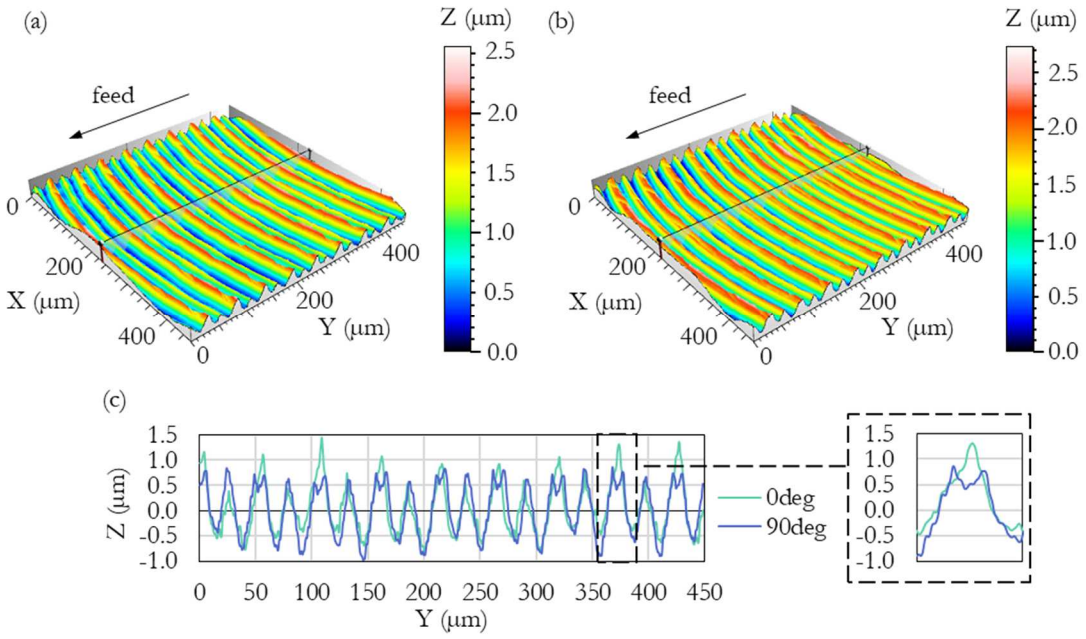

Figure 4.15: 3D surface topographies of the 0deg (a) and 90deg (b) samples and their roughness profiles (c) along the feed direction of surfaces milled with v_c of 30 m/min and f_z of 0.05 mm/tooth.

The presence of the double peak can be attributed to the returning cutting edge in the back-cutting phenomenon, which is known to be mainly caused by the axial runout of the tool or by high radial cutting forces [167,168]. According to the Authors just cited, the surface texture is mainly determined by the tool geometry, cutting conditions and workpiece material. Since the adopted tool geometry and cutting conditions of the example reported in **Figure 4.15** are the same, and that the tool axial runout can be neglected because of the repeatability of the obtained results, the only variable causing the back-cutting can be the workpiece material, namely its anisotropy induced by the AM process.

Considering the kurtosis *Sku* (see **Figure 4.16 (a)** and **(b)**), it is possible to note that, except for a single case, all the surfaces reported values lower or close to three, indicating that surfaces had a Gaussian height distribution. This means that the surfaces varied gradually, without extreme peaks or valleys. When comparing the two build-up orientations, the *Sku* values were on average the same. However, the effect of the different cutting parameters on them was different. At increasing the cutting speed and feed per tooth the kurtosis increased for the 0deg samples and decreased for the 90deg ones. The cutting speed had a limited effect on *Sku* values, whereas the effect of feed per tooth was more pronounced. At f_z-, the 0deg samples allowed for less spiky surfaces that were free of extreme peaks or valleys (lower *Sku* values), while at f_z+ this was true for the 90deg ones. This is due to the already mentioned effect of the αGB layers that helped the material removal for the 0deg samples at f_z-, and the tendency of the 90deg samples to lead to the formation of double peak feed marks at f_z+ that makes the surface less spiky. In general, the machined surfaces of the two build-up orientations reported opposite skewness.

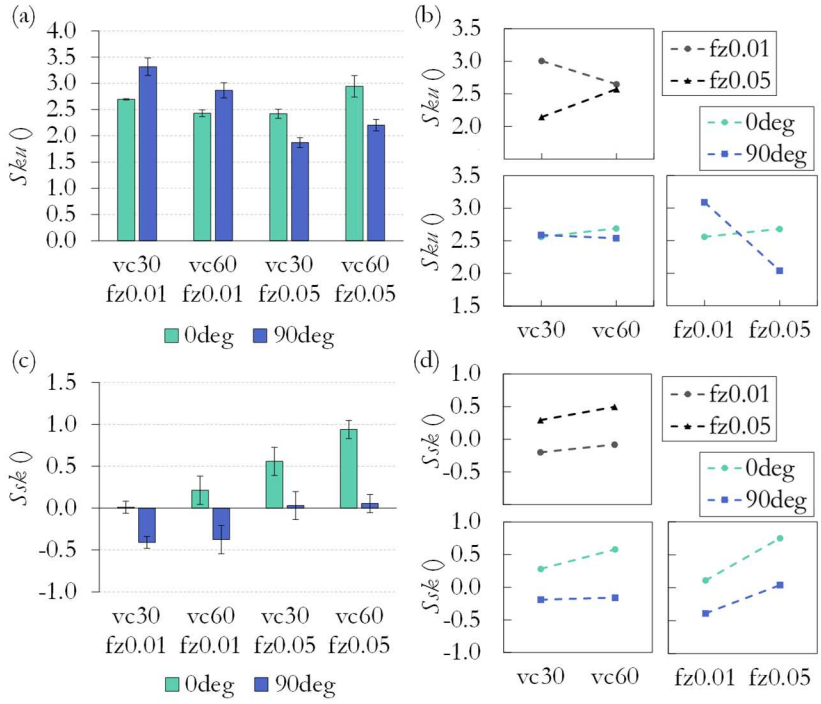

Figure 4.16: Kurtosis *Sku* and skewness *Ssk* of the milled samples (a) and (c), and interaction plots of fitted means (b) and (d), respectively.

In fact, the 0deg samples presented surfaces dominated by peaks, i.e. positive *Ssk* values, whereas the 90deg samples surfaces dominated by valleys, i.e. negative *Ssk* values (see **Figure 4.16 (c)** and **(d)**). These results agree with what commented on the former height parameters and show that the growth direction of the samples significantly influenced the surface texture in terms of skewness. Consequently, it can be said that the skewness is a discriminating parameter for distinguishing the build-up orientations of machined AMed surfaces, similarly to what was found by Cabanettes et al. [16] for as-built AMed surfaces. In particular, it was found that at f_z-, the 0deg samples showed an approximately symmetric surface (*Ssk* values near zero), while at f_z+ this was found for the 90deg samples. At increasing the feed per tooth and the cutting speed, *Ssk* increased with a more marked effect of the former cutting parameter.

As commented above, the 0deg samples presented machined surfaces dominated by peaks, which were, moreover, characterized by a greater percentage of material forming higher peaks compared to the 90deg samples, which means higher *Smr1* and *Spk* values (see **Figure 4.17 (a)** and **(b)**). On the contrary, the 90deg samples reported a greater percentage of material forming deeper valleys compared to the 0deg samples, which means lower *Smr2* and higher *Svk* values (see **Figure 4.17 (c)** and **(d)**). Both the reduced peak height and the valley depth, in general, increased at increasing the cutting parameters. Considering in detail the trend of the functional parameter *Spk*, it can be observed that the cutting parameters had a remarkable effect: the peak height increased with the increase of both the feed per tooth and the cutting speed, with the effect of the former more evident.

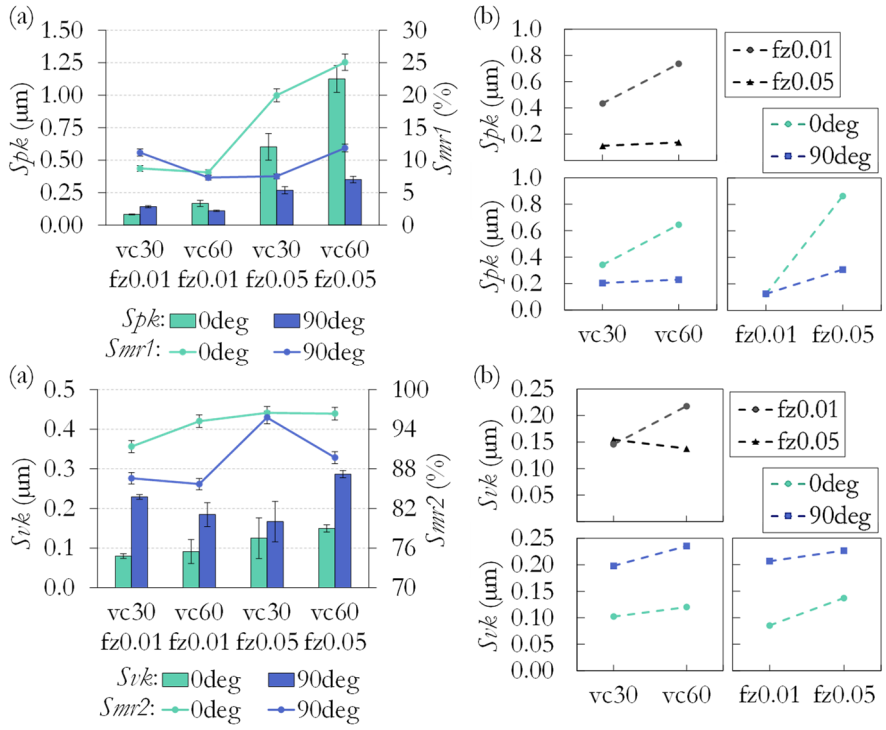

Figure 4.17: Reduced peak height *Spk* and peak material portion *Smr1* of the milled samples (a) and interaction plots of fitted means for *Spk* (b). Reduced valley depth *Svk* and valley material portion *Smr2* of the milled samples (c) and interaction plots of fitted means for *Svk* (d).

The different cutting parameters had a greater effect on the *Spk* and *Smr1* parameters for the 0deg samples (differences up to 7 times) compared to the 90deg ones (differences up to 2 times). This is in accordance with the fact that, in the 0deg samples, the αGBs interact with the cutting edge of the tool, leading to a wider range of textures when changing the cutting parameters (see also the differences between the two samples orientations of the *Ssk* parameter). On the other side, the cutting tool does not interact in the same way with the discontinuity zones, i.e. the αGBs, of the 90deg samples, which appear more intact to the cutting edge compared to the 0deg ones.

For what concerns the spatial parameters, in **Figure 4.18 (a)** and **(b)** the texture aspect ratio *Str* values are shown. As expected, the values are close to zero (this parameter equals one for isotropic surfaces) since the machined surfaces are anisotropic due to the presence of the feed marks. As can be seen from the graph, all the values are below 0.15. In general, the various cutting parameters have influenced the 0deg samples more than the 90deg ones. The two samples reported similar values when machined at low cutting speed, while differed the most when a higher cutting speed was applied. This parameter as well revealed the influence of the αGBs interaction with the cutting tool, but it was evident only at the highest cutting speed.

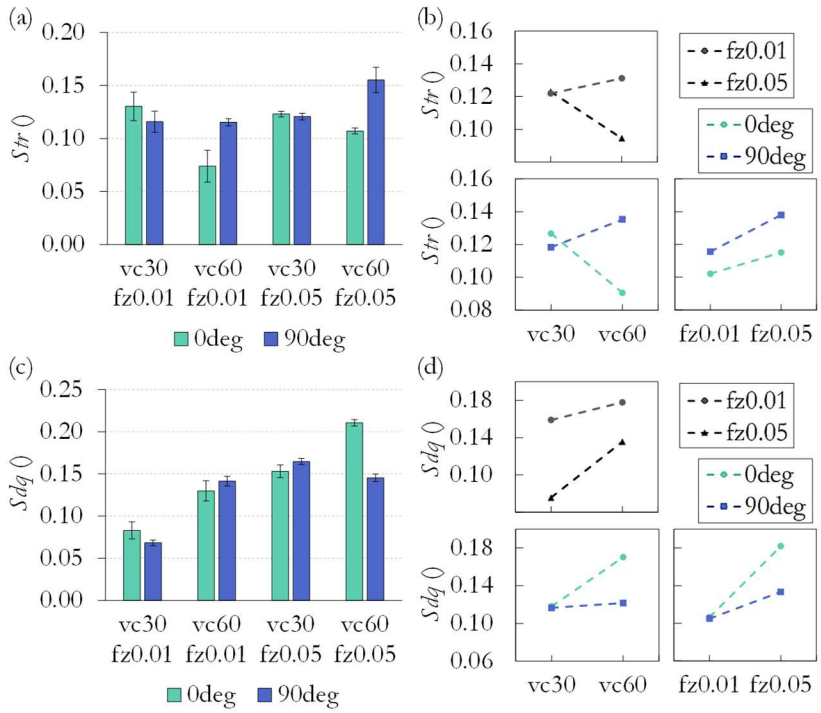

Figure 4.18: Texture aspect ratio *Str* and root mean square gradient *Sdq* of the milled samples (a) and (c), and interaction plots of fitted means (b) and (d), respectively.

Regarding the hybrid parameters, in **Figure 4.18 (c)** and **(d)** the root mean square gradient *Sdq* values are shown, which give information about the complexity of the surface. The surfaces became more complex at increasing cutting parameters, mostly when machining the 0deg samples. The increase of the cutting speed had a greater effect in increasing the complexity of the surface when the f_z- was utilized, however, f_z+ led on average to higher complexity. In general, all the samples reported low *Sdq* values indicating a good cosmetic appearance,

especially when machining at f_z- and v_c-. In fact, those surfaces appeared quite reflective at the naked eye, especially for the 0deg samples.

Surface defects

Figure 4.19 shows the defects found on the milled surfaces, which are characteristic of the titanium alloys. Feed marks were clear on all the sample surfaces, reflecting the feed per tooth set. Adhered micro-particles, debris of elemental chips, and smeared feed marks were also observed. The build-up orientation had no influence on the amount and typology of the surface defects. In general, adhered material and smeared feed marks were predominant in surfaces machined at f_z-, indicative of the fact that an increase in the material plasticity occurred. This result suggests that machining with low values of the feed per tooth may have increased the cutting temperatures, contrary to what is usually reported in the literature [127]. A possible explanation is that, in our case, the cooling effect of the lubricant may not have been sufficient to prevent the cutting temperature rising because of the higher contact time between the rotating tool and the workpiece due to the low feed, together with the fact that the 100% engagement of the tool prevented the lubricant to reach directly the cutting zone. At increasing cutting speed, the amount of adhered material debris and smearing increased, suggesting a further increase of temperature around the tool tip, according to what is commonly reported in the literature.

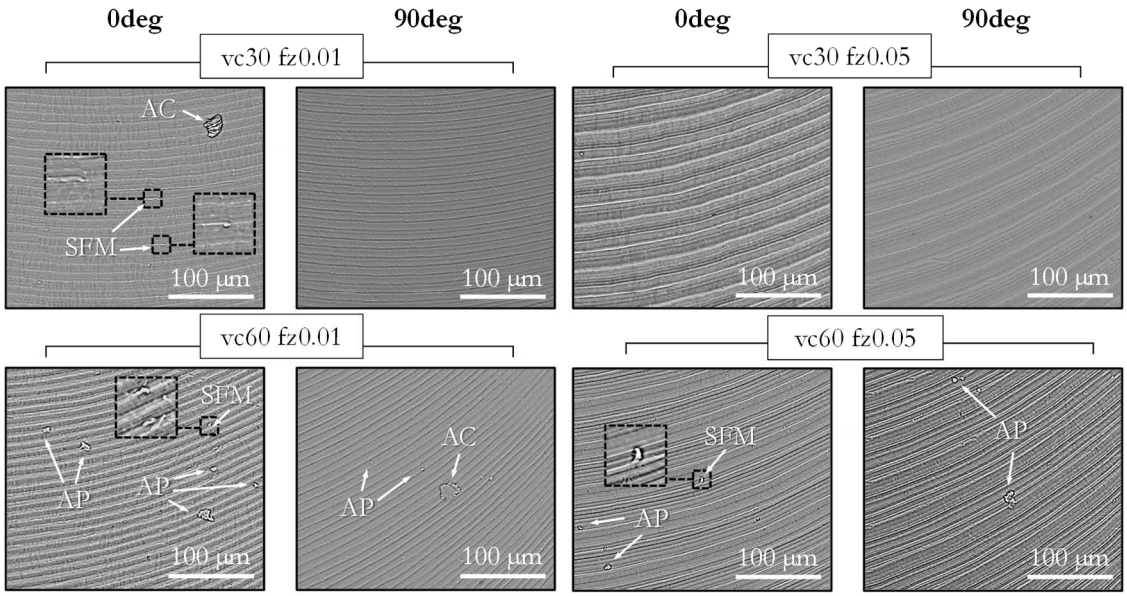

Figure 4.19: Surface defects of the machined slots. AC: adhered elemental chip, AP: adhered microparticles, SFM: smeared feed mark.

Burrs extent

The SEM observations of the machined surfaces revealed the presence of tear-type burrs at the up- and down-milling sides of the slots (see **Figure 4.20 (a)**). More pronounced burrs when machining with f_z- rather than with f_z+ can be immediately noted. Moreover, at f_z-, high quantities of material adhered to the up-milling side, especially at higher cutting speeds possibly because of the higher heat development in the cutting zone as explained in the previous sub-section. On the contrary, the increase of the feed per tooth avoided the material adhesion at

the sidewalls of the slot. The burrs height measurement (see **Figure 4.20 (b)** and **(c)**) confirmed the qualitative SEM analysis: the average burrs height was 9.9 ± 1.1 μm and 1.7 ± 0.99 μm at f_z- and f_z+, respectively, which both slightly increased at increasing cutting speed. In general, the burrs of the 90deg samples were 18% larger than those of the 0deg ones. As already mentioned, in the 0deg samples, the rotating cutting edge interacts with the weak αGBs in a way that helps the material removal decreasing the cutting forces. Thus, the plastic deformation, i.e. the dislocation movements which are known to promote the burrs formation and increase its extent [130], result to be less intense than in the 90deg samples. This may explain the lower tendency of the 0deg samples to form burrs respect to the 90deg ones.

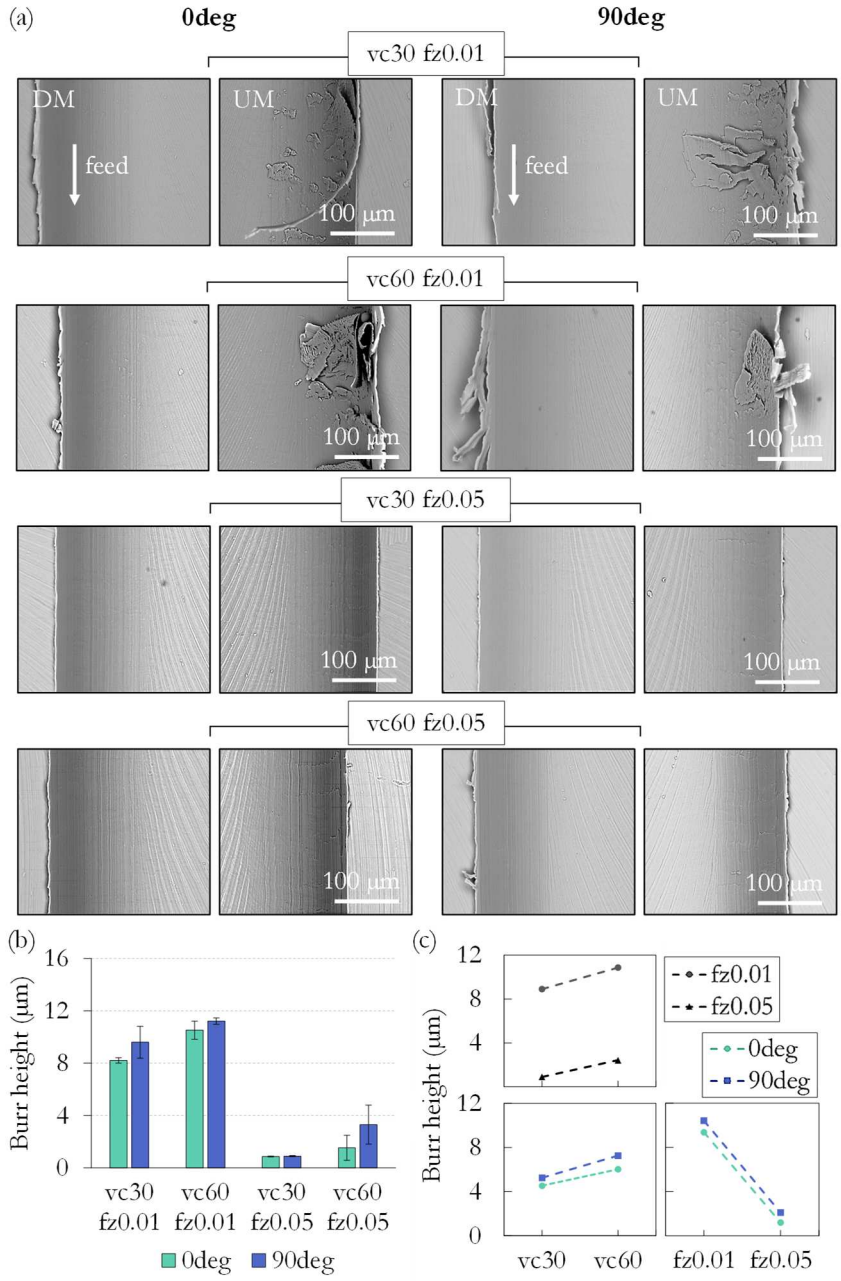

Figure 4.20: Tear-type burrs at the top of the machined slots. DM and UP stand for down-milling and up-milling, respectively (a); burr height of the milled samples (b), and interaction plots of fitted means (c).

Chip morphology

From a general point of view, curled ribbon chips with lamellar free surface formed at whatever milling condition (see **Figure 4.21**). Some specific differences can be pointed out to varying of both the cutting parameters and build-up orientations. When f_z- was utilized, chips tended to weld together forming longer chips. One of the principal reasons for this phenomenon can be ascribed to the development of high friction and thrust forces between the tool rake face and the workpiece [169]. This is in accordance with the high amount of adhered material at the up-milling sidewall of the slots as previously discussed. Moreover, machining at f_z- led to the formation of a non-negligible amount of elemental chips and thin metal debris, especially for v_c+, since the low feed hindered the complete formation of the chip at each tooth pass. In the latter case, the high pressing action of the tool was also confirmed by the presence of serrations and cracks at the lateral edges of the chips, which, instead, were absent when machining at f_z+.

In **Figure 4.22** the effect of the cutting parameters and build-up orientations on the chips free, back and lateral surfaces is reported. It was observed that the serration and cracks depth increased at increasing cutting speed, reaching up to 48 μm. Observing the lateral surface of the chips, only partial segmentation occurred when machining at f_z-, while marked segments can be observed at f_z+, which are known to be indicative of severe plastic deformation [165]. The maximum chip thickness decreased (up to 37%) at increasing cutting speed. This means that the chip compression ratio decreased with the cutting speed, denoting a lower cutting power [166]. This was validated also by the shear plane angle Φ of the primary shear zone visible on the lateral surface of the chips obtained at f_z+. The shear angle Φ was close to zero (perpendicular shear planes) when machining at v_c-, indicating high cutting forces, while it was greater than zero when machining at v_c+, which is known to denote lower cutting forces [103].

The free surface of the chips was characterized by lamellae that were thinner for f_z- than for f_z+. Moreover, an increased cutting speed led to thinner and more regular lamellae for both the feeds per tooth in accordance with [111]. In fact, at higher cutting speeds the plastic flow is promoted, allowing for the formation of more marked shearing. The reduction of the lamellae thickness by the cutting speed growth led at the same time to more curled chips in agreement with [170]. This may confirm that the cutting temperature increases at increasing cutting speed, causing the material ductility increase.

The back surface of the chips, which is in contact with the tool rake face, resulted to be smoother than the free surface. The combination of high friction and high temperature generated a flat surface with slight grooves as observed in the results of Section 4.2.1.

Both serrations and elemental chips were found to be more accentuated when machining the 90deg samples rather than the 0deg ones. Moreover, higher thicknesses, lower Φ angles, and lower curl radii were observed in 90deg samples chips. This consolidates what was found in Section 4.2.1: there is a greater ease of material removal for the 0deg samples due to the favorable αGBs interaction with the cutting edge.

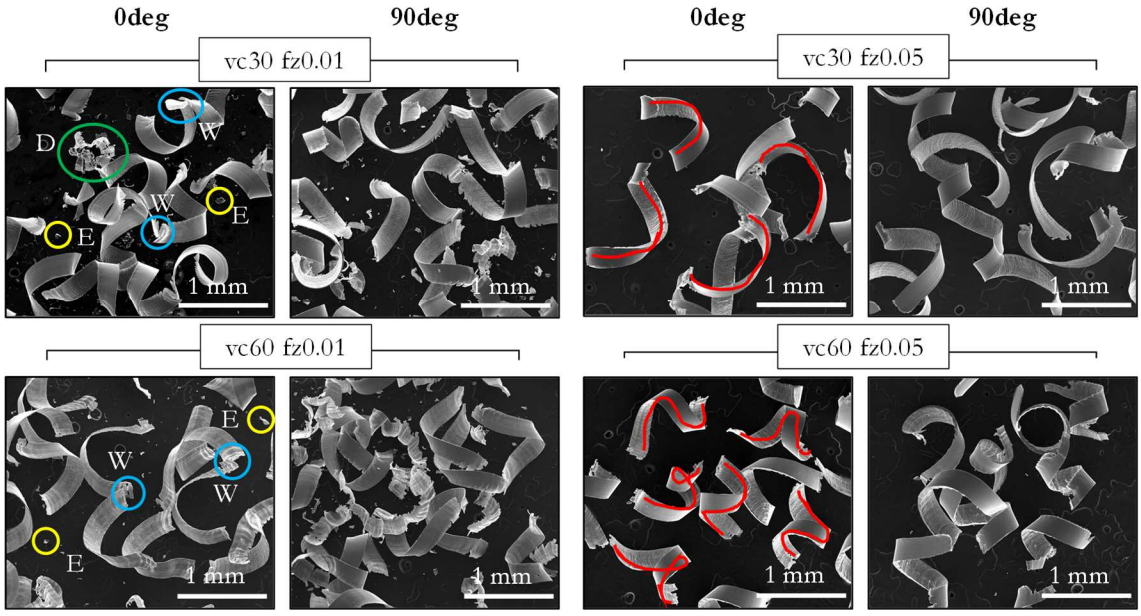

Figure 4.21: Chip morphology of the milled samples. W: chip welding; D: thin debris; E: elemental chip. The curl extent is highlighted in red.

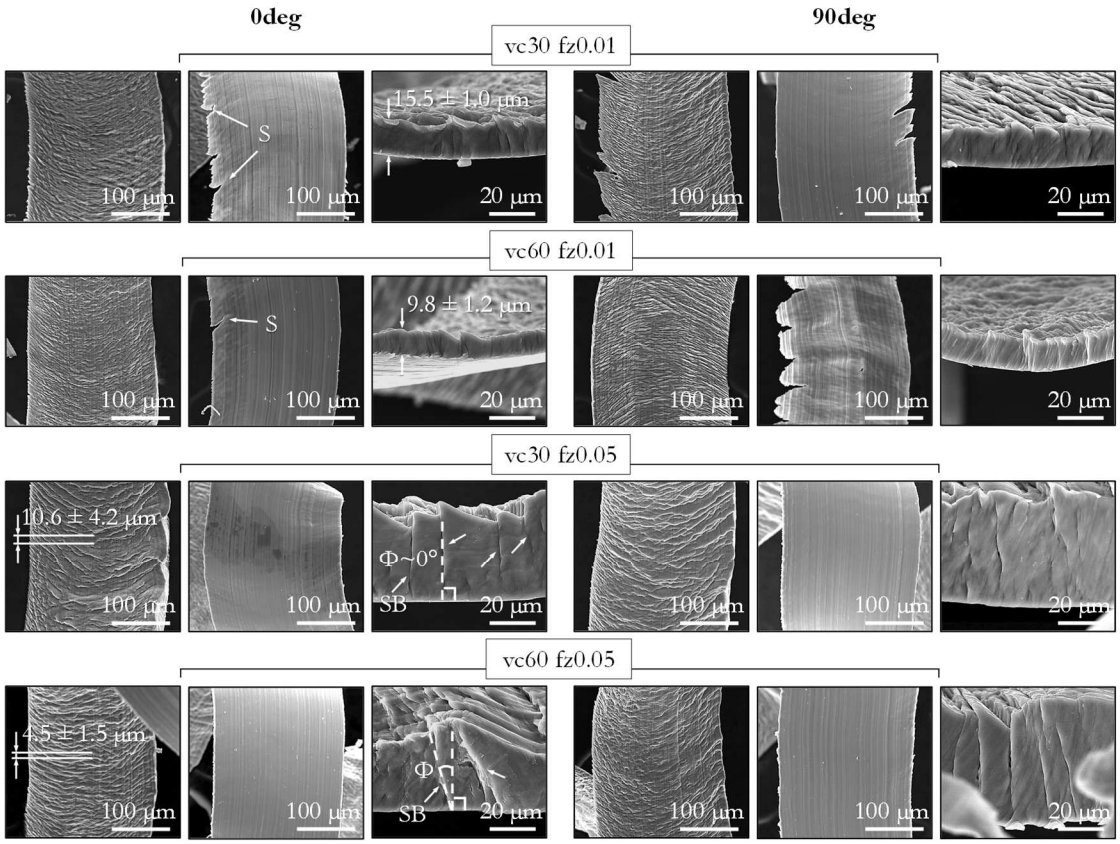

Figure 4.22: Effect of the cutting parameters and build-up orientations on the chips free, back and lateral surfaces. S: serration, SB: shear bands, Φ: shear plane angle.

Conclusions

The most relevant conclusions follow:

- The machined surface of the 0deg samples presented higher variations of areal texture parameters since the entity of the interaction between the cutting edge and the αGBs is preponderant when machining the 0deg samples than the 90deg ones. In fact, in the former case the cutting edge is parallel to the weak αGBs, and may come into contact with them more frequently than in the latter case.
- Generally, the 0deg and 90deg orientations led to machined surfaces with comparable surface roughness (*Sa*). However, the 0deg samples were dominated by higher peaks (positive *Ssk* and high *Spk*) and higher complexity (higher *Sdq*), particularly at the highest feed per tooth.
- The texture parameter that most distinguished the machined surfaces of the two build-up orientations was the skewness *Ssk*, which was on average positive for the 0deg samples and negative for the 90deg ones.
- The typology and amount of surface defects on the machined surfaces were mostly influenced by the cutting parameters rather than the build-up orientation. However, the latter influenced the burrs height, which was lower for the 0deg samples. The αGBs helped the material removal reducing the plastic deformation involved in the cutting process, this decreasing the dislocation movements, which are known to promote the burrs formation.
- Chip morphology analysis gave indications of lower cutting power and forces (lower chip compression ratios and greater shear plane angles) when machining the 0deg samples rather than the 90deg ones, in accordance with the findings of Section 4.2.1. This was accentuated at higher cutting speed, which promoted the material plastic flow allowing for higher chips curl radii.

4.2.3 Machining with ball end mills – effect of different cutting paths

Specific microstructural and mechanical considerations

In this study the wrought annealed Ti6Al4V alloy was taken into consideration as well, as stated in Section 3.2.1, abbreviated as WR. **Figure 4.23 (a)** and **(d)** display the microstructures along the height of the heat-treated AMed and WR workpieces, respectively. In both the alloys the α and β phases are distinguishable, which appear in light and dark after etching, respectively. The AMed workpieces microstructure is formed by α plates arranged in colonies and coarse αGBs along the BD as amply documented through the text, which results in an obvious anisotropy. The WR alloy, on the other hand, is formed by fine α phase equiaxed grains, thus exhibiting an isotropic microstructure. The Vickers microhardness of the two types of workpieces was found to be equivalent, being 322 ± 24 $HV_{0.1}$ and 317 ± 20 $HV_{0.1}$ for the AMed and WR samples, respectively. Therefore, despite the microstructural differences, the two types of workpieces showed the same microhardness, which is reasonable given that they are nominally the same alloy; moreover, the indentations generated on the surface were larger than the microstructural features, and, therefore, not sensitive to the different arrangement of grains. Furthermore, just a 3% difference in microhardness was detected among different

cross-sections of the AMed workpieces and among blocks with different planes inclinations. However, when comparing the β phase fraction of AMed and WR alloys through the mapping reported **Figure 4.23 (b)** and **(d)**, a substantial difference was found. The β phase fraction was 36% and 18% for AMed and WR alloys, respectively, as is also reported in a previous literature study [171]. Finally, a significant difference in the arrangement of the β phase, which lays at the α phase grain boundaries, is evident, as visible in **Figure 4.23 (b)** and **(d)**. The β phase has an elongated arrangement in the AMed alloy, whilst it is uniformly distributed in a globular form in the WR alloy.

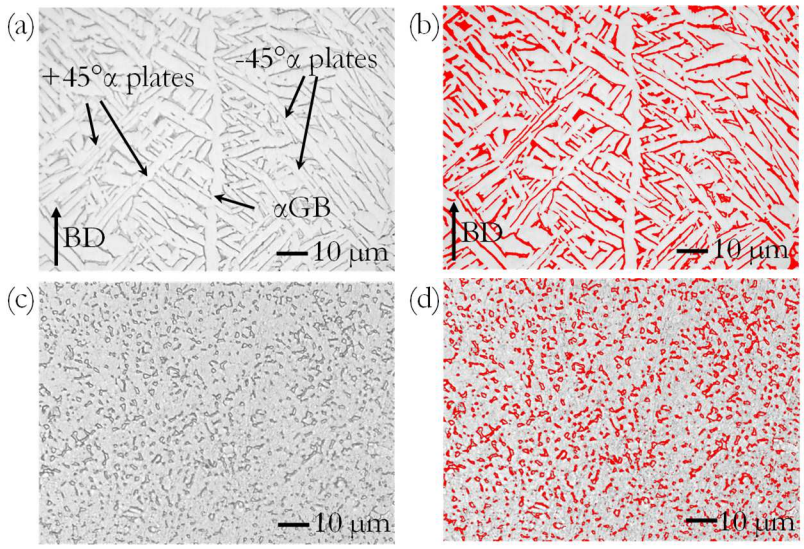

Figure 4.23: Microstructure of the heat-treated AMed (a), and WR Ti6Al4V workpieces (c). Mapping of the β phase for the AMed (b) and WR (d) workpieces.

Cutting forces

According to the reference system in **Figure 3.9**, for HU milling, *Fx* refers to the pick feed force, tangential to the feed direction of the tool, while for the VU milling *Fx* denotes the feed cutting force that acts alongside the feed direction of the tool. *Fy* is the feed force in the case of HU milling and the pick feed force in the case of VU milling. *Fz* denotes the cutting force parallel to the tool rotation axis for both the tool paths orientations. **Figure 4.24 (a)** displays the main effects plots of the resultant cutting force as a function of the workpiece manufacturing process, tool path orientation, and workpiece inclination angle. It is possible to observe that the cutting forces were generally greater for the AMed workpieces than for the WR ones. Moreover, HU milling led to higher mean cutting forces than VU, even if the effect of the tool path orientation was lower than the one of the alloy type. The inclination angle had the greater effect on the cutting forces: in particular, the forces were much higher for surfaces inclined at 15° compared to those inclined at 45° and 75°, the latter instead showed comparable cutting forces. Analyzing more in detail the trends of the force data, it can be noted that the effect of the manufacturing process presented an inverse trend ($Fres_{AM} < Fres_{WR}$) only in the case of HU milling on the 45° sample, as shown in **Figure 4.24 (b)**, which reports the effects plot of the resultant cutting forces in the case of the HU and VU cutting paths as a function of the workpiece inclination angle.

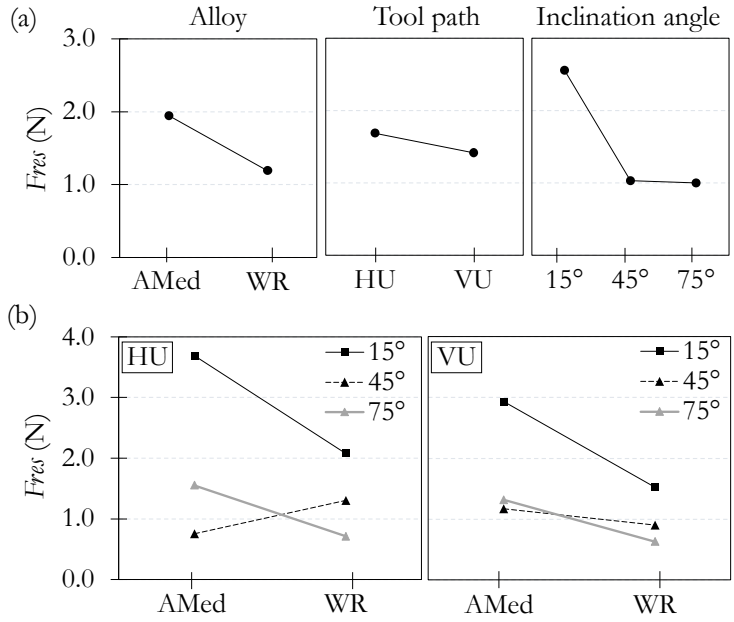

Figure 4.24: Main effects plots of the resultant cutting forces (a), and specific trends of the resultant cutting forces in the case of the HU and VU cutting paths (b).

In **Figure 4.25 (a)**, **(c)**, and **(e)** the cutting force components for the three differently inclined AMed workpieces at different tool path orientations are reported. The greatest force component when cutting the 15° inclined surfaces was the axial component *Fz*, both in HU and VU milling, because the tool engaged the workpiece surface from above due to the modest inclination angle. As far as HU milling is concerned, the AMed workpiece reported all the three force components always greater than the WR one, while in VU milling the main difference was recorded for the pick feed force component. Therefore, the AMed workpiece imposed greater resistance laterally to the feed direction. In the case of 45° inclined surfaces, the HU and VU milling reported an opposite trend of the force components. When milling with a horizontal tool path, the main force component is the axial one since, also in this case, the tool engages the workpiece from above, while in the vertical orientation, the main component was the feed force, since the tool climbs up the inclined surface. In the case of HU milling, the AMed workpiece reported very low feed and pick feed force components than the WR one, while the axial force components of the two alloys did not differ substantially. This was not replicated in VU milling, reporting the general trend, namely $Fres_{AM} > Fres_{WR}$. This suggests that the AMed workpieces, somehow, helped the chip formation in HU milling, as will be discussed at the end of this Section. For the 75° workpieces the main force component was the *Fx* one in both HU and VU, because, when milling highly inclined surfaces, the tool is prone to deflect away from the machined surface [172]. This was confirmed also by the fact that, in general, the pick feed force component was higher than the feed force one, especially when milling the AMed workpiece. This is usually an index of tool deflection [173,174]. On the contrary, the axial component of the force was really low. For the 75° inclination, the forces were always higher for the AMed workpiece than for the WR one, confirming the general trend.

Finally, analyzing the trend over time of the force signals, there was always the presence of two force peaks in one tool rotation (t_r), corresponding to the material cutting by the two

cutting edges of the tool for the 15° and 45° inclined samples (see **Figure 4.25 (b)**, **(d)** for HU milling of the AMed workpieces), indicating a stable cut. On the contrary, the 75° surfaces did not always report two regular peaks in one tool rotation, confirming the hypothesis of tool deflection during cutting (see **Figure 4.25 (f)**).

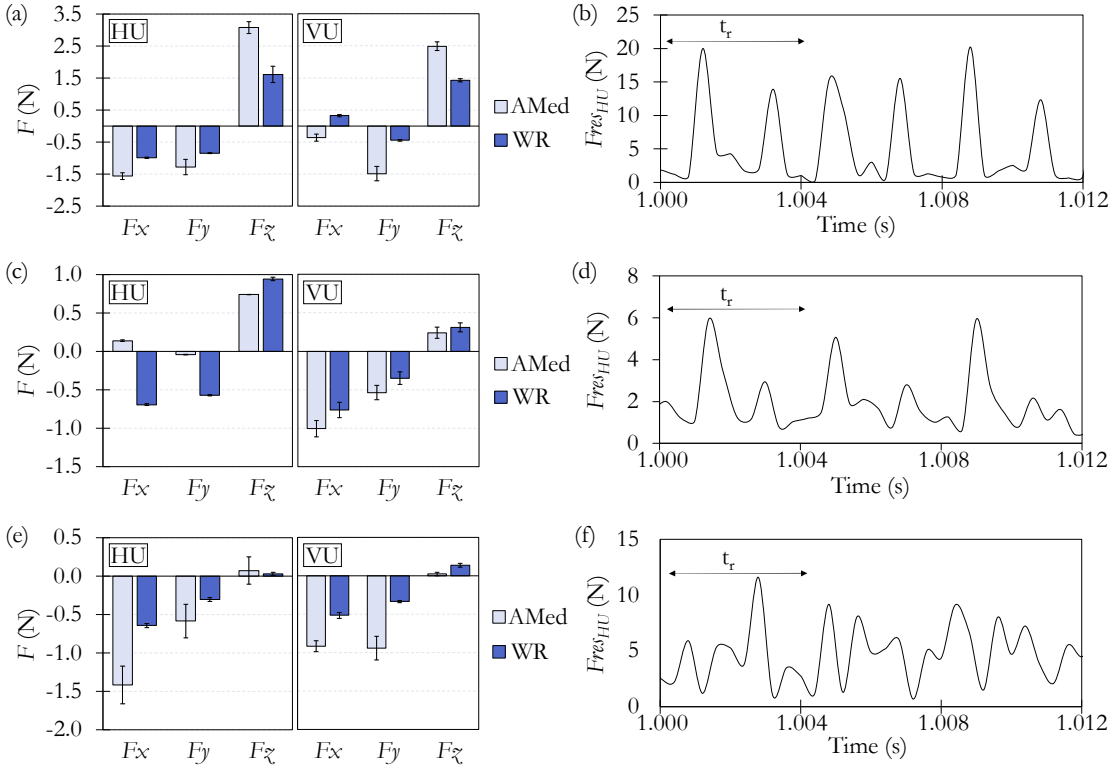

Figure 4.25: Comparison of the cutting force components for the 15° (a), 45° (c), and 75° (e) workpieces at different tool path orientations, and resultant cutting force over time of the 15° (b), 45° (d), and 75° (f) AMed workpieces machined with HU milling.

Surface texture and topography

For each machined surface, five scans of 1.5 × 1.2 mm^2 were captured: one at the center of the machined slot and four at the corners with 20× objective. The surface topography of the milled workpieces was always characterized by a cusp-shaped structure as generated in conventional machining operations. The morphology of the tool marks was consistent with the chosen pick feed *pf*, but not with the feed *f*. This is because the vibrations occurring during machining have a direct impact on the surface topography [175]. In particular, the roughness profiles along the tool feed direction of all the machined surfaces of the 15° and 45° workpieces show regular tool marks with distances corresponding to the feed *f* instead of to the feed per tooth *f*/2. This can be seen in **Figure 4.26 (b)** and **(d)** for what concerns the HU milling of the AMed workpieces. Such features of the surface texture exclude that chatter occurred, and, rather, denote a tool run-out, as suggested in [175]. In fact, the regularity of the features of the surface texture indicates that the tool vibrated with constant amplitude at each rotation of the tool, as happens when the tool vibrates with the tooth passing frequency and its harmonics. Moreover, the force signal trend over time revealed the occurrence of two force peaks in one tool revolution, as reported in the previous sub-section. On the contrary, the 75° workpieces

showed machined surfaces with no well-defined tool marks in the feed direction (see **Figure 4.26 (f)**). By observing the topography as a whole, it was possible to notice a large waviness. The observed results are compliant with the hypothesis of the tool deflection that was made when analyzing the cutting force signals.

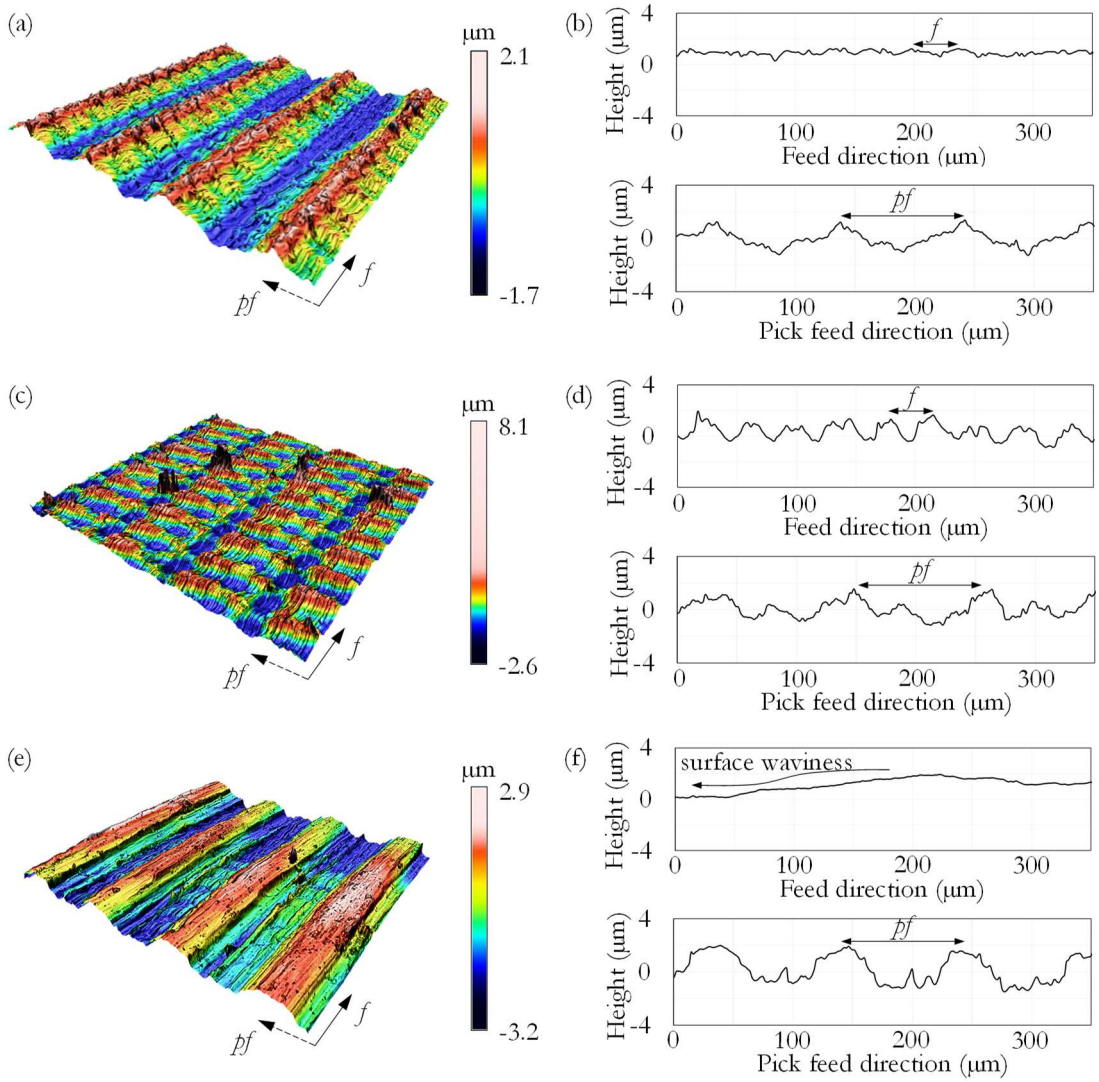

Figure 4.26: 3D surface topographies (a)-(c)-(e), and 2D roughness profiles (b)-(d)-(f) of the 15°, 45°, and 75° AMed workpieces respectively, machined with HU milling. The dimensions of the reported scans are 384.5 × 356.5 µm.

Figure 4.27 (a) reports the main effects plots of the roughness parameters examined in this study, as a function of the manufacturing process, tool path orientation, and workpiece inclination angle. As for the cutting forces, also in this case the main effect was given by the workpiece inclination angle. However, differences were also recorded when the type of alloy and the tool path varied. In general, the AMed samples, compared to the WR ones, reported surfaces with roughness *Sa* greater than 21%, with a more complex texture (*Sdr* > 49%), and with a higher average height of the feed marks (*Spk* > 30%). The values of the amplitude parameters *Ssk* and *Sku* were, instead, lower for the AMed workpieces than for the WR ones, by 14% and 28% respectively. This denotes the prevalence of inordinately spike structures on

the WR surfaces, which can be identified as adhered particles. As far as the tool path is concerned, the HU surfaces, compared to the VU ones, reported higher *Sa* values, as it can be also found in the literature [172,176,177]; however, when considering the other surface roughness parameters, the texture complexity, mean peaks height, skewness and kurtosis values were higher for VU than for HU milling. Therefore, horizontal milling made it possible to obtain surfaces with less prominent and more regular feed marks, with less material adhesion. Since the major differences between the two cutting paths refer to the *Ssk* and *Sku* values, it can be stated that in VU milling the chip is more difficult to evacuate, tending to stick to the surface. The milling operations carried out on the surfaces inclined by 15° led to low roughness *Sa* values, together with low surface complexity, low average height of the peaks and average depth of the valleys, however bringing *Ssk* and *Sku* values above the average. Overall, such surfaces were quite smooth, but with a higher amount of adhered material/smeared feed marks compared to the core roughness. Conversely, the 45° inclined workpieces resulted in high roughness *Sa*, high complexity, high peaks, and deep valleys, therefore surfaces with very marked features, as can be observed in the example reported in **Figure 4.26 (c)** and **(d)**. The machining operations performed on the 75° workpieces, on the other hand, produced surfaces with roughness parameters that were largely identical to those of the15° inclined ones, except for the skewness and kurtosis parameters. In fact, observing the 3D topographies and the 2D profiles in **Figure 4.26 (a)**-**(b)** and **(e)**-**(f)** it is possible to note that the 75° inclined surfaces led to bumpier surfaces with a more gradual variation of heights, which results in lower *Ssk* and *Sku* values than the 15° inclined surfaces. The difference in the surface topography of the different inclinations is related to the principal cutting mechanism that took part during the machining operation. The results suggest that the cutting tool machined better the 45° inclined surfaces since uniform and well-defined concave features characterized the texture, as suggested in [172], therefore the overall surface resulted rougher, while, for the other two inclinations, the cutting mechanism was principally the plowing one rather than shearing. In the case of the 15° inclined workpieces, plowing was due to the low effective cutting speed [176–178], as suggested also by the high cutting forces (see **Figure 4.24**). Furthermore, when the cutting speed is low, the deformation rates are low as well, and the material strength is higher, resulting in higher cutting forces [115]. In the case of the 75° inclined workpieces, the plowing effect may have arisen from the instability of the tool that induced vibrations [172] and/or from the high effective cutting speed [24,179]. In fact, the latter usually causes an increase of the cutting zone temperature, with the consequent increase of the workpiece material plasticity, which, in turn, decreases the cutting forces, as actually occurred (see **Figure 4.24**). The SEM analysis of the defects will further clarify the analysis of the surface topography.

Figure 4.27 (b) shows the trends of the roughness parameters for the three inclined surfaces as a function of the alloy type. In all the HU milling cases, the 45° inclined workpieces reported opposite trends compared to the other two, namely the trends of the main effects plots. This resulted in lower roughness, lower peaks, and shallower valleys in the 45° AMed workpiece than in the WR one. However, these surfaces showed higher *Ssk* and *Sku* values, thus denoting a greater presence of peaks and irregular heights, due to the presence of adhered material. In the case of VU milling, however, the 45° inclined workpiece reported opposite

trends only in the case of the *Ssk* and *Sku* parameters. Therefore, the core roughness of the 45° inclined surfaces remained high, nevertheless the surfaces were freer of adhered material than the other two inclinations.

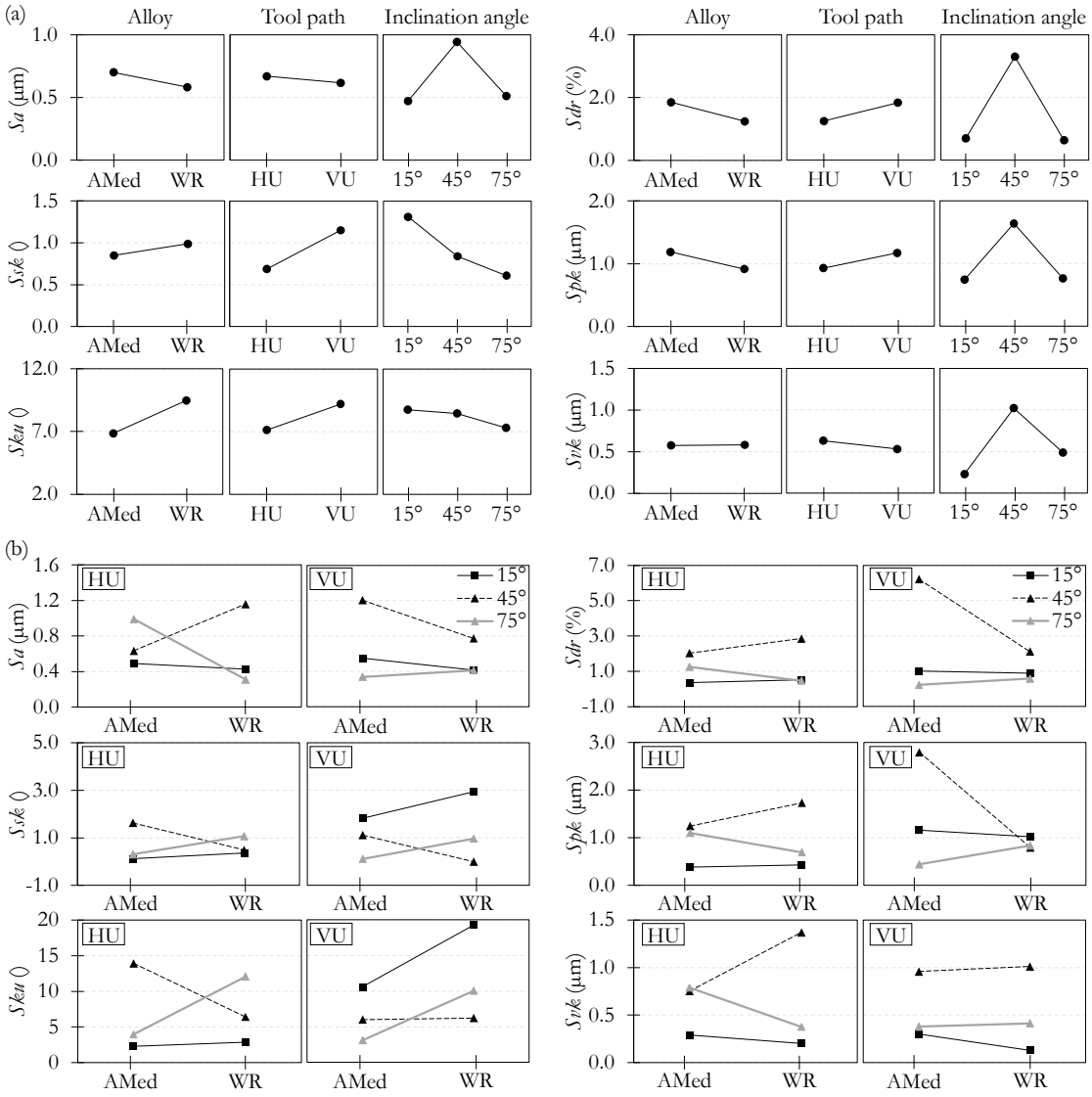

Figure 4.27: Main effects plots for the examined roughness parameters (a), and specific trends of the examined roughness parameters in the case of HU and VU cutting paths (b).

Surface defects

The SEM analysis of the machined surfaces shown in **Figure 4.28** supports the outcomes of the areal roughness parameters. In general, compared to the AMed surfaces, the WR ones showed a higher amount of adhered material particles, which were mostly smeared chips and debris of chips. This may be related to the different ductility of the two alloys, in particular, it is known that the WR Ti6Al4V is more ductile than the heat-treated AMed one [180], thus favoring a more intense adhesion of workpiece material on the machined surface [103]. Comparing the tool path effect, the VU milled surfaces reported a higher amount of adhesion than the HU ones, confirming the hypothesis of the difficulty of an efficient chip evacuation

in such operations as commented in the previous sub-section. In all the cases the lay pattern in the *pf* direction was visible, while the feed marks were clear only for the 15° and 45° inclined surfaces, and the 75° inclined workpieces reported smoother surfaces. The 15° inclined workpieces reported more smeared tool marks, especially in VU milling, showing also adhered chip debris up to 50 μm of dimensions. These results confirm the possibility that the plowing occurred when machining both the 15° and the 75° inclined workpieces. Finally, the HU milled surface of the AMed 45° inclined workpiece showed smaller but more prominent adhered material on the top of the tool marks than the WR counterpart, which agrees with the higher values of *Ssk* and *Sku* found in the latter case. Contrarily, the AMed 45° inclined workpiece VU milled reported jagged tool marks, which were less accentuated in the WR counterpart, which is compliant with the higher *Sa* and *Sdr* values of the former case.

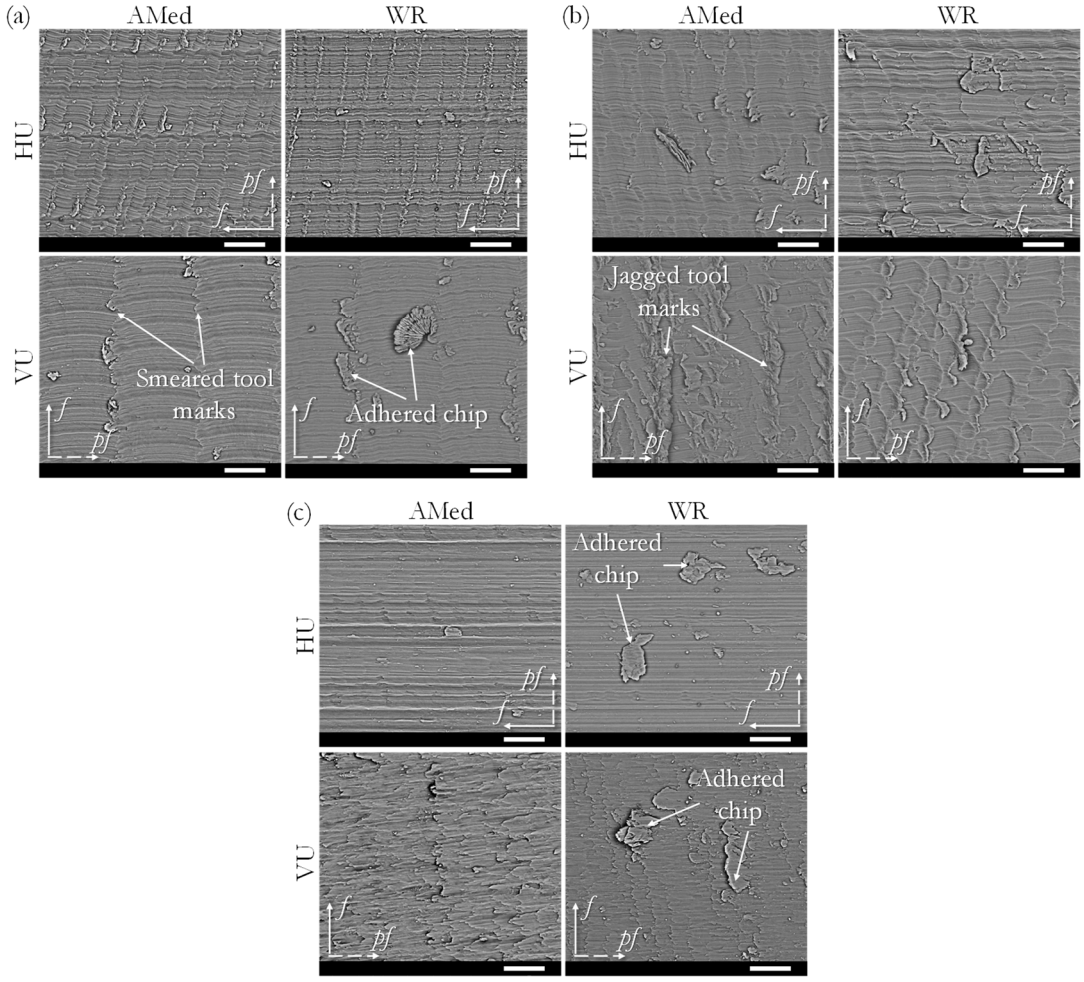

Figure 4.28: SEM images of the machined surfaces of 15° (a), 45° (b) and 75° (c) workpieces. Scale bar: 50 μm.

Chip morphology

Figure 4.29 (a)-(c) report some examples of SEM images of chips collected under the different studied conditions. The different chip morphology as a function of the tool path is a clear indication of the fact that the chip flow changed in HU and VU milling even if the downcutting condition was set in both cases. In particular, VU milling led to the formation of

short and fan-shaped chips, while HU milling mostly resulted in slender needle-like chips no matter the alloy microstructure, i.e. AMed or WR. Evident dissimilarities of the chip morphology can be also seen at varying machined surface inclination: the chips were overall longer in 15° inclined surfaces and shorter for the 45° and 75° ones. Serration and cracks were particularly present in the chips of the 45° inclined workpieces, especially when machining the AMed ones in HU milling. On the contrary, HU milling of the 45° inclined WR workpieces led to fan-shaped highly segmented coarse chips, along with elemental and discontinuous ones, showing the shear planes on their back surface, in accordance with the higher cutting forces that were recorded. Even in the case of VU milling of both the alloys workpieces inclined at 45° discontinuous chips were formed with marked serrations. Discontinuous chips are usually related to high surface roughness and complexity, confirming the results for the 45° inclined workpieces reported in the section dedicated to the surface topography. It is worth noting that, in the case of the 75° inclined workpieces, the number of chips joined together was the highest. This is a consequence of the high *Fx* force component, as commented for **Figure 4.25 (e)**, which compressed the rake face of the tool against the workpiece, inducing friction welding of the chips. The rear surface of all the collected chips was characterized by a smooth surface with scratch marks in the direction of the tool rotation, generated as a result of the high contact and shear stresses experienced by the chips in contact with the tool rake face. Moreover, some adhered workpiece material was observed in all the chip back surfaces indicating that micro welding occurred between the chip and the tool during chip formation.

Some more detailed comments can be made by looking at the quantitative analysis of the chips features reported in **Figure 4.29 (d)**. In general, between the AMed and WR alloys, there was no evident difference in the size of the lamellae on the chip free surface, except for the 45° inclined workpieces that were HU milled. In the latter case, the lamellae were 27% thinner for the AMed sample than for the WR one. This is an indication of the fact that in the AMed sample the plastic flow was promoted, as will be discussed at the end of this Section. Overall, VU milling led to higher lamellae width than HU milling. In particular, the chips of the VU 45° inclined workpieces showed 78% higher lamellae width than the other chips obtained in VU milling. The SEM images at higher magnification revealed that there was an evident discontinuity in such chips, promoted by shearing along the primary shear zone as a consequence of the Ti6Al4V low thermal conductivity. In this case, the unstable thermoplastic shear may be related to the increased heat in the cutting zone during machining, developing a conflict between thermal softening and work hardening in the primary shear zone, thus inducing the crack initiation in the chip [181]. This is supported by the fact that the cutting forces in VU milling of the 45° inclined workpieces resulted to be among the lowest, despite the high final surface roughness, suggesting that the thermal softening effect prevailed over the hardening one [182]. The most noteworthy differences in the lamellae width are those at varying workpiece inclination angles, consistently with the fact that at varying the machined surface inclination angle, the different contact point of the ball end mill causes a change of the effective tool diameter and, thus, of the cutting speed, which is the main factor influencing the lamellae frequency [111,181]. The actual cutting speed increased from the 15° inclined workpiece to the 75° one, which should have consequently led to a progressive thinning of the lamellae, a condition that was verified in HU milling. On the contrary, in VU milling this

correlation was not confirmed: the reason can be a different chip flow mechanism in such cutting path, as commented also in [177,183]. In fact, the lamellae width of the chips collected from VU milled workpieces with 15° and 75° inclined surfaces was the same, whereas it was higher for the 45° inclined workpieces as above commented.

For what concerns the chip length, also in this case, in general, there was no evident difference between the AMed and WR workpieces, except for the HU milled 45° inclined workpieces and the VU milled 75° inclined ones. In the first case, the chips were 81% longer for the AMed samples than for the WR ones, while in the second case the chips were 59% shorter for the AMed samples than for the WR ones. The SEM analysis of the chips of the WR 45° inclined workpiece showed that the shorter length resulted from the significant degree of deformation of the chips in the welded ends, which had a jagged and rough morphology. Furthermore, the drop in the chip length can be attributed to the chips predisposition to shatter into little fragments during these cutting operations due to adiabatic shear, as previously described. In the case of the 75° inclined workpieces, the AMed chips resulted shorter since they were perforated with irregular ends, as a consequence of the high compressive forces [184] exerted by the tool on the workpiece inclined plane as previously observed. Overall, HU milling led to 64% longer chips than the VU milling in agreement with the previous comments on the different chip flow mechanisms as a function of the cutting path. Finally, the different tool-workpiece engagement in ball end milling at varying the workpiece inclination angle led to different chip lengths. The chips obtained when machining the 15° inclined workpieces were the longest (up to + 62%), as expected [185].

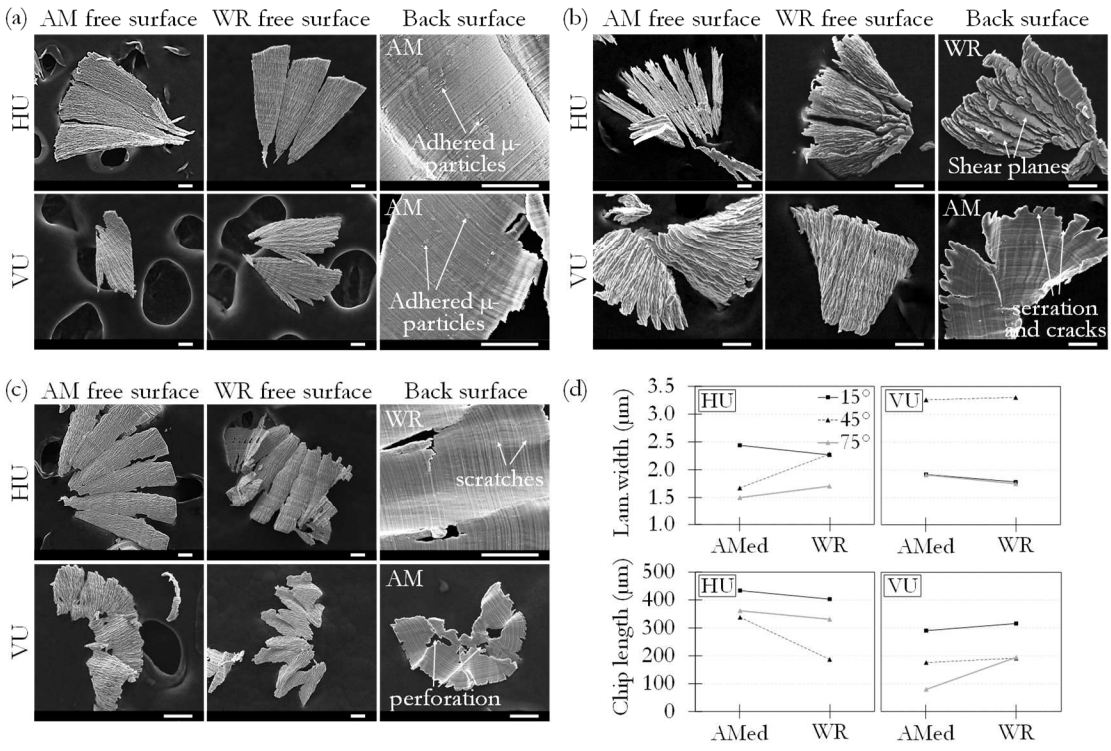

Figure 4.29: SEM images of the chips at varying cutting conditions of 15° (a), 45° (b) and 75° (c) workpieces. Scale bar: 50 μm; specific trends of the chip features in the case of HU and VU cutting paths (d).

Tool-workpiece interactions

Some microstructural observations are here presented to explain the differences in machinability reported in this Section between the two alloys. **Figure 4.30** displays a scale model of the tool-workpiece interaction for the three inclined workpieces and the respective zoom of the tool cutting edge engagement with the microstructure of the AMed workpieces. The coarse αGB layers along the BD are highlighted in dark blue, the α plates with + 45° and – 45° orientations are in purple and green, respectively. In ball end milling, the vertical αGBs have a negligible influence on the cutting operation because their orientation does not interact positively with the cutting edge that is removing the material, which was the case of the flat end milling operations discussed in this Chapter. The results discussed in this Section showed that the main differences between the AMed and WR alloys were found for the 45° inclined workpieces machined under HU tool path, which reported a trend opposite to the average. In particular, the AMed workpieces were characterized by lower cutting forces and lower surface roughness with less prominent tool marks (thus lower *Spk* and *Svk* values) than the WR ones. Furthermore, the AMed chips were more regular than the WR ones, which, instead, had extended welding zones, high segmentation, and discontinuous morphology with wider lamellae. All these features confirm the fact that when machining the AMed 45° inclined workpieces there was lower tool-chip friction involved which enhances the surface quality and the chip homogeneity. Since the tool wear observed at SEM after machining was negligible, the identified discrepancies can be attributed only to the two workpieces distinct microstructures, which produce a different material response to cutting, resulting in different tool-workpiece interactions. Looking at the representation of the interaction between the cutting edge and the AMed microstructure for the 45° inclined workpiece in **Figure 4.30 (d)**, it is easy to see that the cutting edge may occasionally encounter the α plates colonies with parallel direction to it, i.e. with the – 45° α plates in green. The α grains groups parallel to the cutting edge can locally minimize the force required to remove the material for two reasons: 1) the α phase is more prone to accommodate plastic deformation than the β phase, and 2) the β phase boundaries do not obstruct the plastic deformation. In fact, it is known from the literature that the α colonies are preferential zones for the movement of the dislocations and crack initiation [186,187] and that the β phase at the α grain boundaries limits the slip length [187]. Thus, as the cutting edge engages the various α colonies, the material resistance to cutting decreases, as does the tool-chip friction, when the α colonies are tangential to the cutting edge, that is the case of the 45° inclined AMed workpiece. On the contrary, the WR workpieces are characterized by equiaxed isotropic grains (see **Figure 4.23 (c)**) and no analogous microstructural characteristic to the AMed workpieces allowed for a reduction in material resistance to cutting, resulting in higher cutting forces and the consequent degradation of the surface quality. The same reasoning does not apply to the VU milling, which, as already pointed out in the previous sections, offers the chip flow mechanism that differs from the one in HU milling, and is not defined in the literature. In the case of HU milling of the other two inclined workpieces, namely 15° and 75°, the trends were compliant since both the AMed workpieces reported higher cutting forces and surface roughness than the WR ones. Observing how the cutting edge of the tool interacts with the microstructure of the AMed workpieces with the 15° and 75° inclined surfaces in **Figure 4.30 (b)** and **(f)** respectively, it is possible to see that the

α colonies are oriented in a direction that is irrelevant to the cutting edge. From this observation it would be expected that the results of the cutting forces and the roughness parameters are similar between the two alloys, however, this was not the case, as above stated. The obtained results can be linked to the β phase fraction and arrangement differences between the AMed and WR alloys, as commented for **Figure 4.23**. In fact, the volume fraction of the β phase is higher for the AMed alloy than for the WR one; moreover, the β phase is in the form of elongated aggregates in the former case, while in the case of the WR alloy it has a homogeneous distribution and in a globular form. As previously stated, the β phase impedes the movement of the dislocations making plastic deformation difficult. Moreover, it is common knowledge that also the grain boundary area constitutes an obstacle for the movement of the dislocations, which is facilitated in the case of equiaxed grains rather than in lamellar ones [188]. This would explain why, when the α colonies are not in a concordant position with that of the cutting edge, the cutting forces are greater for AMed alloy than for WR one. The same concepts can be extended to VU milling of 15° and 75° inclined workpieces.

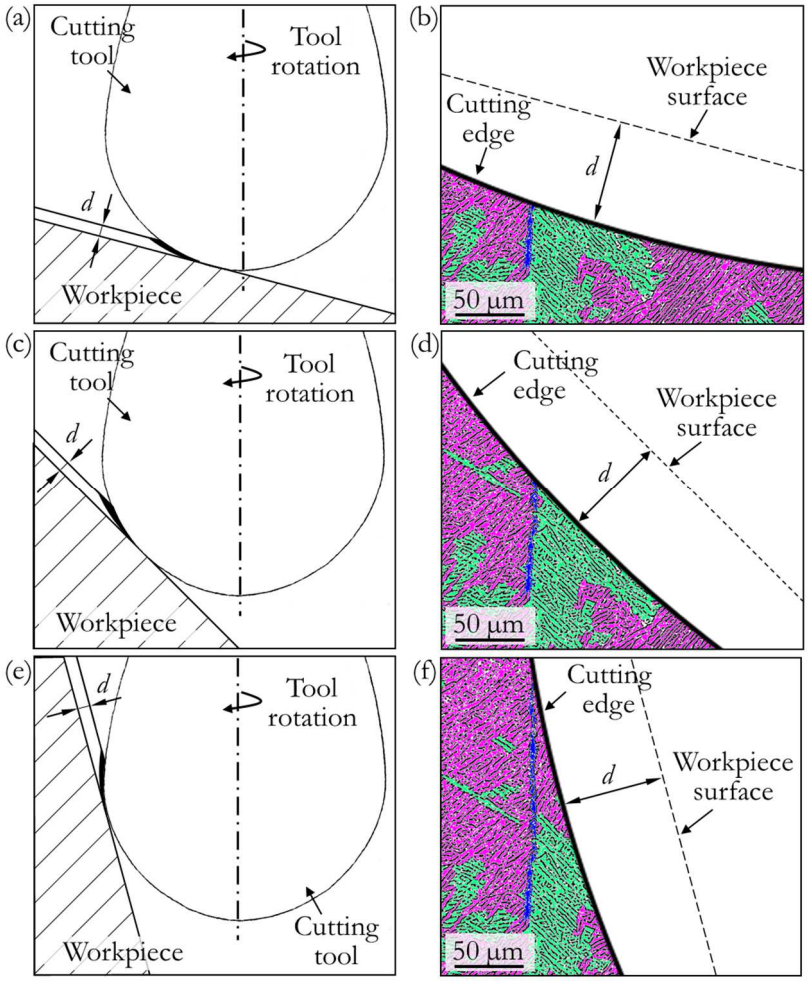

Figure 4.30: Scale model of the tool-workpiece interaction for the 15° (a), 45° (c), and 75° (e) inclined surfaces, and the respective zoom (b), (d), and (f) of the tool cutting edge interaction with the microstructure of the AMed workpieces. The α grains with different orientations are distinctly colored.

Conclusions

The key findings are the following:

- The AMed workpieces led to higher cutting forces together with higher surface roughness and more prominent tool marks, but a lower quantity of adhered material than the WR ones. However, the AMed and WR alloys showed an inverted trend in machinability when machining the 45° workpieces in HU milling, leading to lower cutting forces, lower surface roughness, and less prominent tool marks in the case of AMed workpieces.
- The better machinability shown by such AMed workpieces can be ascribed to their microstructural features, namely α phase colonies tangential to the cutting edge in the case of the 45° ones, which favor the material removal by locally lowering the material resistance to deformation.
- In general, regardless of the alloy microstructure, VU milling allowed for lower cutting forces, no matter the machined surface inclination, and lower surface roughness, however, it led to a more complex surface texture and higher amount of adhered material.
- 15° inclined workpieces led to the highest cutting forces but allowed for the smoothest surfaces.

4.2.4 Machining with ball end mills – effect of different cutting parameters

The machinability in ball end milling operations was further investigated on the 45° AMed and WR inclined surface as commented in Section 3.3.1, conducting HU milling operations varying the cutting parameters, namely two depth of cut (*d*15 and *d*73) and two feeds (*f*30 and *f*40) were selected (see **Table 3.2**).

Surface texture and topography

Figure 4.31 reports the main effects plots of the most significant roughness parameters examined in this study, as a function of the depth of cut, feed and manufacturing process. It was possible to observe that the surface roughness *Sa* increased at least three times when machining with the higher depth of cut, at a given feed. Moreover, the roughness *Sa* slightly increased at increasing feed. These observations are in accordance with common knowledge about metal machining as reported in Section 2.2.3. Nevertheless, the most interesting outcome to highlight is that the AMed and WR workpieces reported dissimilar *Sa* values when machining with the higher depth of cut, as visible in the last column of **Figure 4.31**. In fact, machining with *d*15 led to comparable surface roughness values between AMed and WR workpieces, whilst machining with *d*73 put into light the differences among the two. In the latter case, the WR machined surfaces showed 80% and 42% higher *Sa* values than the AMed ones when adopting *f*30 and *f*40, respectively. A similar trend was noticed also for the *Spk* and *Svk* parameters. In particular, the WR surfaces machined with the higher depth of cut showed higher peaks height and deeper valleys than the corresponding AMed surfaces. This is because

the WR samples were characterized by more prominent feed marks. The analyzed surfaces always reported positive averaged values of *Ssk*, indicating surfaces with a predominance of spikes that protrude above the mean line. This is typical for conventional cutting operations such as milling and turning, which produce cusp-shaped topography. The only exceptions were observed for the AMed samples machined with *d*15, reporting negative *Ssk* values, which is peculiar of good finishing processes. The samples with the highest skewness values were the WR and AMed ones machined with parameters *f*30-*d*15 and *f*30-*d*73, respectively. This is related to the presence of very high peaks on the surface, such as pointy adhered particles. This was confirmed by the trend of the *Sku* values, which, in general, were higher than three denoting a spiky surface, and they were much greater for the samples just mentioned.

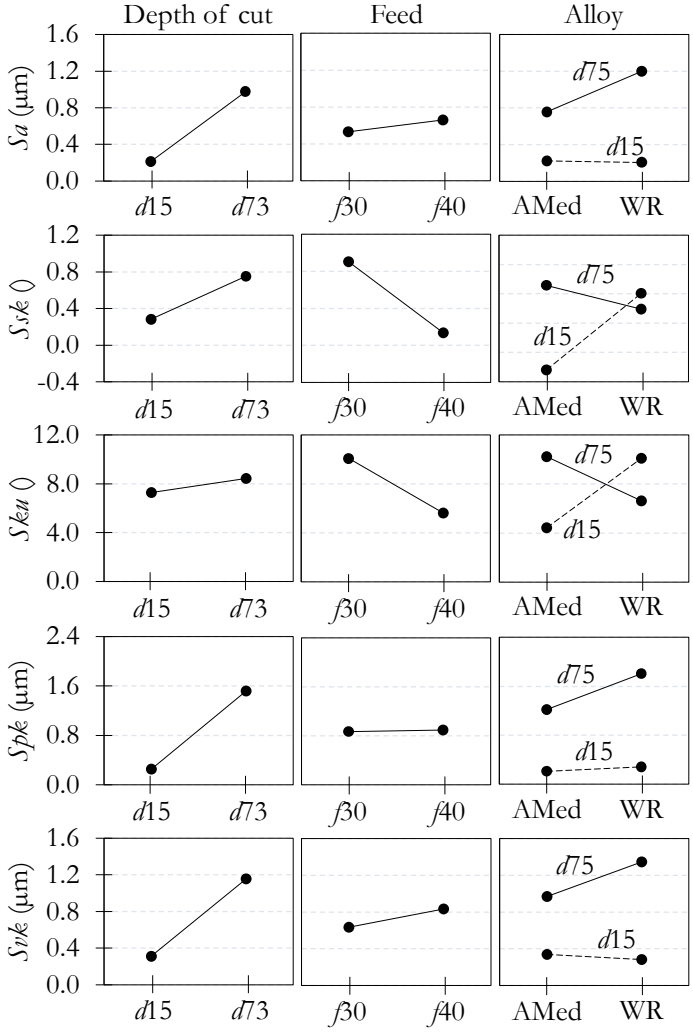

Figure 4.31: Main effects plots for the most significant roughness parameters.

Surface defects

The observations made on the areal roughness parameters were confirmed by the SEM analysis of the machined surfaces (see images in **Figure 4.32**). It was possible to note machining feed marks in all the analyzed cases. The feed marks were denser for surfaces machined with the lower cutting depth (*d*15), and were more pronounced in the case of WR

samples, especially when machined at the higher cutting depth (*d*73). In general, the surfaces machined with the higher depth of cut reported a higher quantity of adhered material. In particular, the WR surfaces machined with *d*73 were characterized by a higher amount of large particles of adhered material, identified as smeared chips. This explains the higher *Sa* and *Spk* values found for these surfaces, as well as the *Ssk* and *Sku* values that set in the middle, accordingly to the fact that the adhered material had a bumpy morphology. On the other hand, the AMed samples machined with *d*15 displayed rare adhered particles and more regular feed marks. This well correlates with the low values of all the roughness parameters reported in the previous section, in particular with the negative values of *Ssk* and the lower values of *Sku*. The surfaces of the WR slots machined with the parameters *f*30-*d*15 as well as the ones of the AMed slots machined with *f*30-*d*73 were characterized by the presence of a higher amount of small but highly prominent adhered microparticles identified as chips debris. Again, this agrees with the high values of *Ssk* and *Sku* found in these cases.

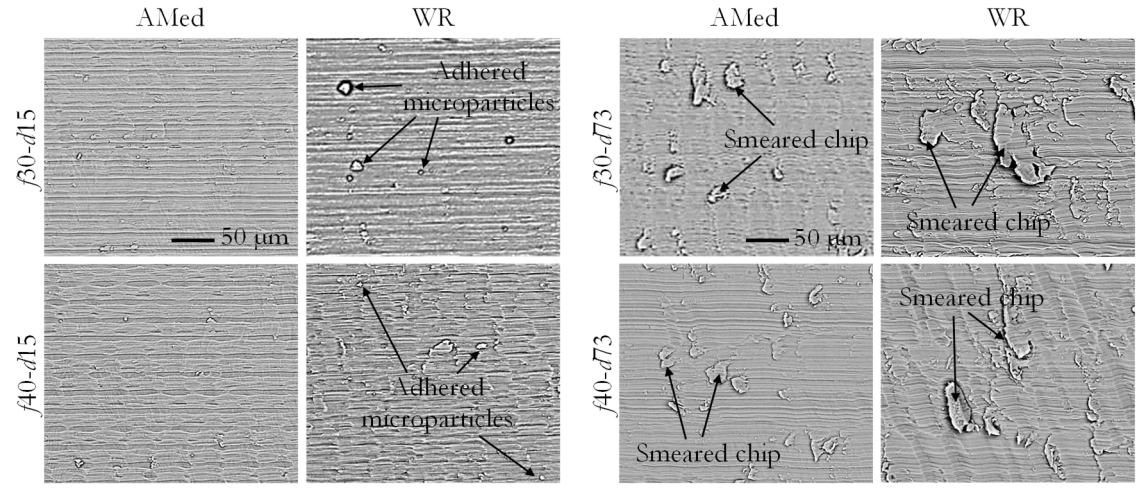

Figure 4.32: SEM images of the 45° HU milled surfaces at varying cutting parameters and alloy type.

Chip morphology

Figure 4.33 (a) reports SEM images of the chips obtained under the different investigated conditions. In general, needle-like chips were obtained when machining with the lower depth of cut (*d*15), no matter the alloy microstructure. Moreover, the needle-like chips were found to be welded at one end into groups of 3-5 chips in the case of the lower feed (*f*30-*d*15). The chips welded together, particularly when the higher depth of cut was adopted. In addition, serration and cracks occurred at the free ends of the chips when machining at the higher cutting depth, especially when machining the AMed workpieces. The WR samples machined with *d*73 presented fan-shaped coarse chips together with elemental chips, confirming what was commented in Section 4.2.3, also for lower feeds. The quantitative analyses reported in **Figure 4.33 (b)** show the same trends for the lamellae width and chip width at any investigated condition. Moreover, at the lower depth of cut (*d*15), AMed and WR samples did not show any major difference in the chip features. The widths of the lamellae and chips slightly increased with the feed. For the higher depth of cut (*d*73), the widths of both the features also increased and, in general, the differences between the two alloys were more pronounced. In particular, the average values of the widths of the lamellae and chips were always higher for the WR

samples. The high plastic deformation of the shear bands in the chips with wider lamellae can have contributed to the widening of the entire chips in the direction perpendicular to that of the lamellae. This can explain the similarities of the trend of the two chip features, as observed above. The chip greatest width obtained when machining WR samples with *d*73 may also derive from the welding of two consecutive chips along the entire chip length, because of higher friction forces developed under the most severe cutting conditions. The length of the AMed chips was higher for the higher depth of cut, congruent with the fact that a greater portion of material was involved in the cutting process. The WR samples showed an opposite trend because of their high degree of deformation as already commented in Section 4.2.3.

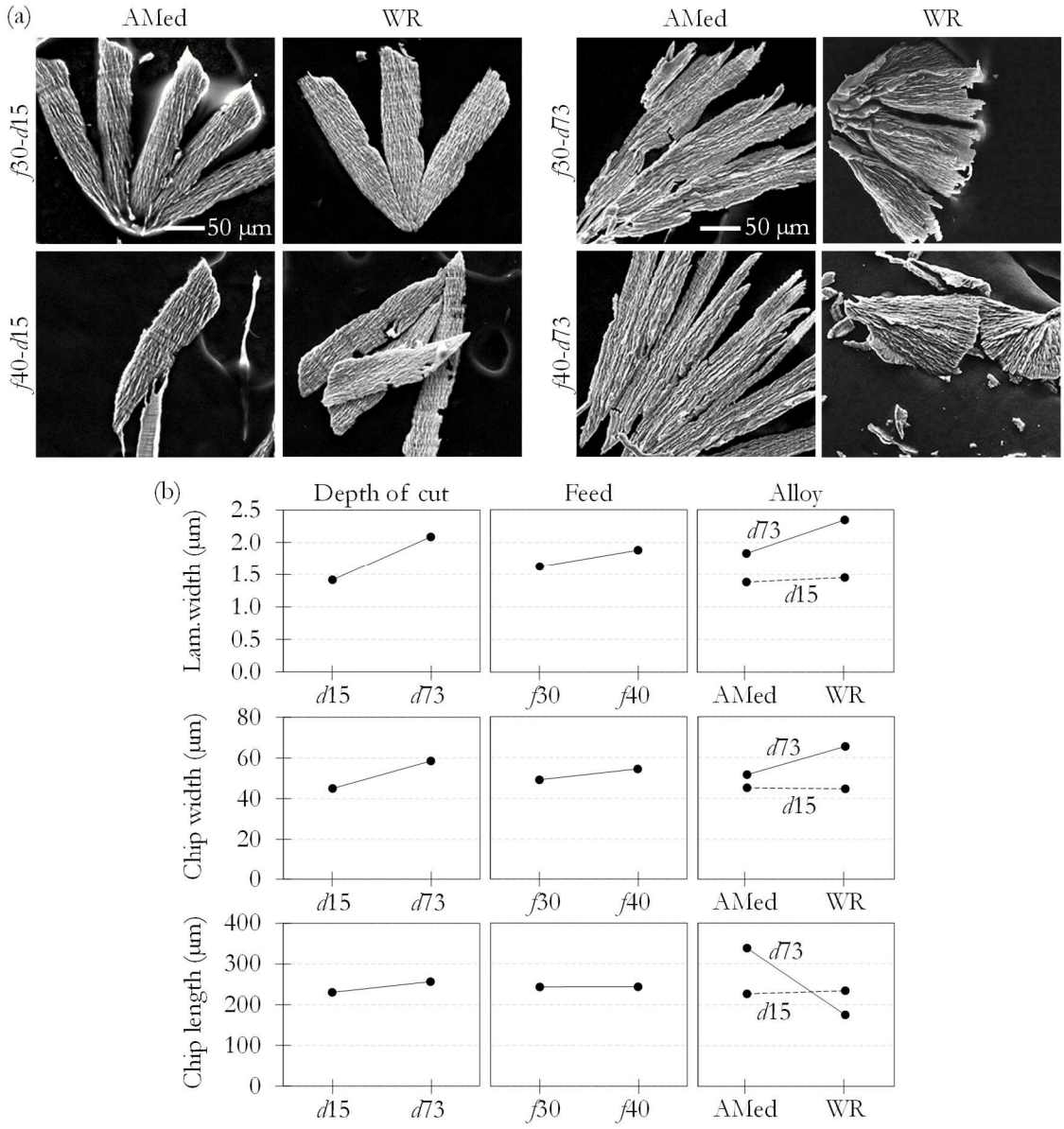

Figure 4.33: SEM images of the chips of the 45° HU milled surfaces at varying cutting parameters and alloy type (a), and main effects plots for the chips geometrical features (b).

Conclusions

The results reported in this Section showed that the tool-workpiece interactions described in Section 4.2.3 for the 45° inclined plane, have a much less effect when a smaller depth of cut is utilized, inducing the AMed and WR alloys to behave approximately the same. In fact, given the same cutting conditions, the smaller the depth of cut the lower the cutting forces. Therefore, the impact of differently oriented α colonies on the material resistance to cutting is less. On the other hand, when a larger portion of material is machined, the cutting forces are higher and the effect of the different microstructures can play a major role.

4.3 Machinability in turning operations

4.3.1 Longitudinal and face turning – surface integrity

Specific microstructural and mechanical considerations

The different scanning strategy adopted for the L-PBF of cylindrical bars, namely stripes and chessboard ones, led to different β grains width as shown in the micrographs and the size distribution histograms of **Figure 4.34**. The bars manufactured with the stripes scanning strategy (**Figure 4.34 (a)**) showed a β grains width 44% higher than the one of the bars manufactured with the chessboard scanning strategy (**Figure 4.34 (b)**).

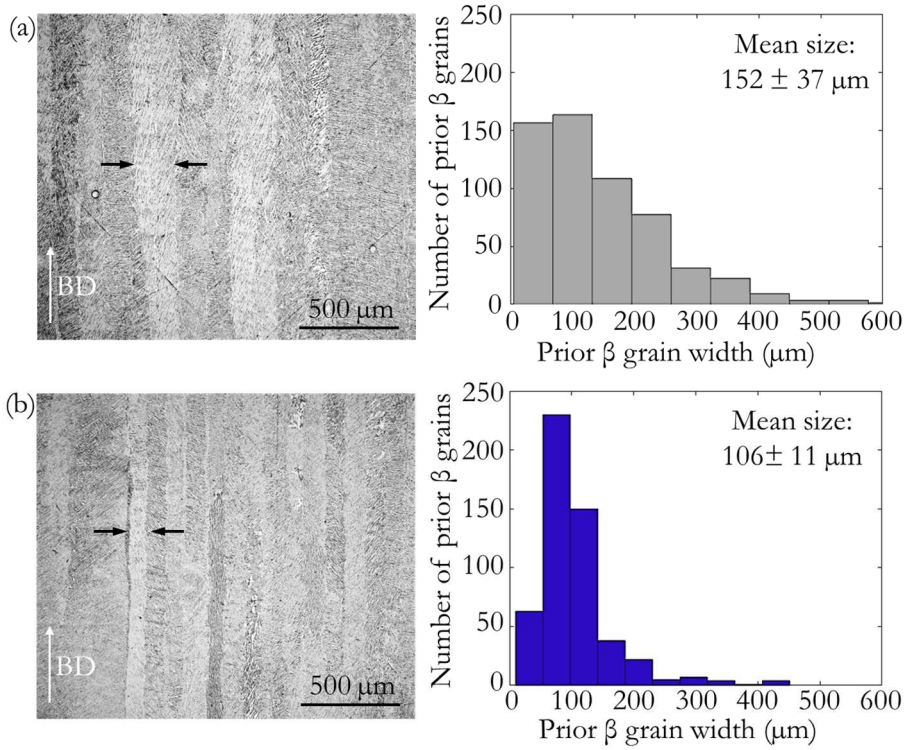

Figure 4.34: Micrographs along the BD and size distribution histograms of the prior β grains width and their mean size for the L-PBFed bars with stripes scanning strategy (a) and chessboard scanning strategy (b).

Table 4.2 reports the microhardness variations along the BD for the investigated samples. By adopting chessboard as scanning strategy, the microhardness increased by 17%. This strengthening is related to the grain refinement, ruled by the Hall–Petch relationship as commented in Section 2.1.4.

Table 4.2: Microhardness of the L-PBFed Ti6Al4V cylinders along the BD.

	Scanning strategy	
	Stripes	Chessboard
Microhardness ($HV_{0.05}$)	307 ± 14	359 ± 18

As reported in **Figure 3.12** of Section 3.3.2, the different cutting directions, i.e. longitudinal and face turning, make possible a different interaction between the cutting tool and the microstructure. Indeed, the tool travels parallel and perpendicularly to the grain growth direction when turning and facing, respectively.

Microstructural and mechanical alterations upon machining

The microstructures of the machined sub-surfaced after longitudinal turning (LT) and face turning (FT) under flood and cryogenic conditions are presented in **Figure 4.35**. In general, as a result of the cutting process, an SPD layer formed below the machined surface with grains bent towards the cutting direction (CD). This zone is solely characterized by the presence of one-directional grain boundaries. The deformation of the grains decreased as the distance from the machined surface increased until, at a certain depth, no deformation of the bulk material was visible anymore.

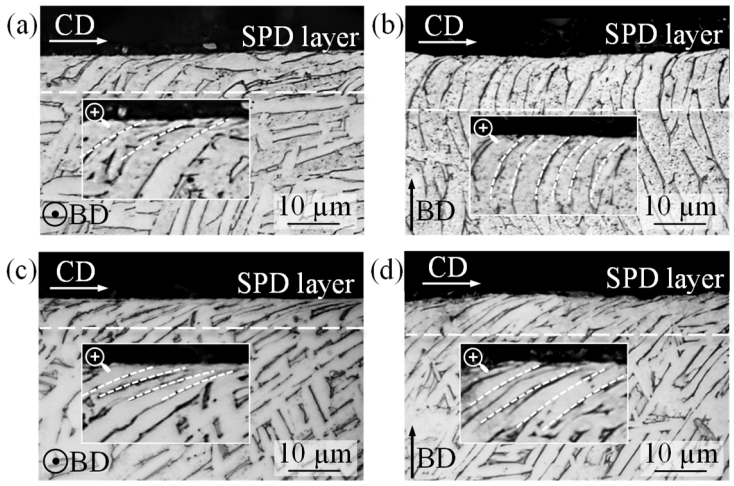

Figure 4.35: L-PBFed Ti6Al4V microstructure of the samples scanned with the stripes strategy and machined under flood (a)-(b) and cryogenic (c)-(d) longitudinal and face turning, respectively.

Figure 4.36 (a) reports the thickness of the SPD layer at varying cutting conditions, whereas **Figure 4.36 (b)** shows the nanohardness percentage variation of the sample machined sub-surface referring to the bulk nanohardness. In general, samples obtained by face turning showed a thicker SPD layer, especially for the bars scanned with the stripes strategy. For those

samples, a 68% and 89% increase in the SPD layer thickness was obtained compared to the corresponding samples manufactured under flood and cryogenic environment, respectively. This difference was reduced in the case of longitudinal turning to 14% and 45%, respectively. The cooling effect did not have a strong impact on the SPD layer extension, being the values for samples machined under flood and cryogenic environment comparable. Finally, the scanning strategy had a substantial effect solely in the case of face turning. To explain the influence of the scanning strategy and cutting direction on the machined sub-surface alterations, the density of the αGBs must be taken into consideration once again. The αGBs are material discontinuities that may favor the material removal during cutting, as found in the studies on milling operations of the previous Sections. Being the prior β grains width lower when using the chessboard scanning strategy, the density of the weak αGBs was higher in these samples, which may have made easier the cutting operation, reducing the strength offered by the material. As already stated, differences in sub-surface alterations were particularly evident in facing operations. In fact, in such operations, the insert cuts progressively the whole cross-section of the rotating bar along its radius. This ensures that the cutting edge encounters the weak αGBs, which are along the BD, more frequently than it happens during cylindrical turning, enhancing their effect on the cutting operation. In addition, the softer the material the higher the tendency of being plastically deformed by the tool. On the contrary, in longitudinal turning, the cutting tool moves parallel to the αGB phase layers, making their presence negligible in the cutting process.

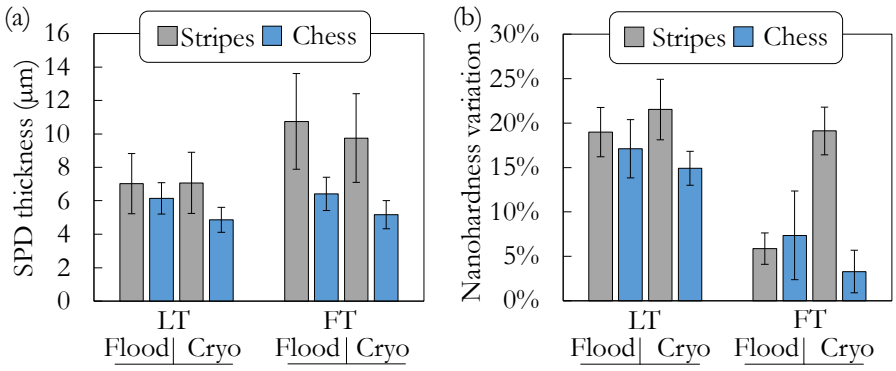

Figure 4.36: SPD layer thickness (a) and nanohardness percentage variation of the machined sub-surface (b).

Surface texture and topography

For each surface, three scans of 0.7 × 3.0 mm^2 were acquired with 20× objective. **Figure 4.37** reports the areal roughness parameters values for all the machined surfaces. Examining the parameters trend, the cutting direction had a great effect in determining the surface texture. In particular, all the examined parameters, on average, decreased between 27% and 61% in face turning rather than in longitudinal one, except for the *Svk* parameter, which increased by 55%. The same trends were found analyzing the scanning strategy influence, even if less pronounced. Specifically, the chessboard strategy led to a reduction of *Sa*, *Spk,* and *Svk* values between 3% and 18%, and to a 25% increase of the *Svk* values with respect to the stripes strategy. These results indicate that both facing and the chessboard scanning strategy allowed

for the formation of machined surfaces characterized by lower roughness, lower peaks height, and principally dominated by deep valleys rather than peaks.

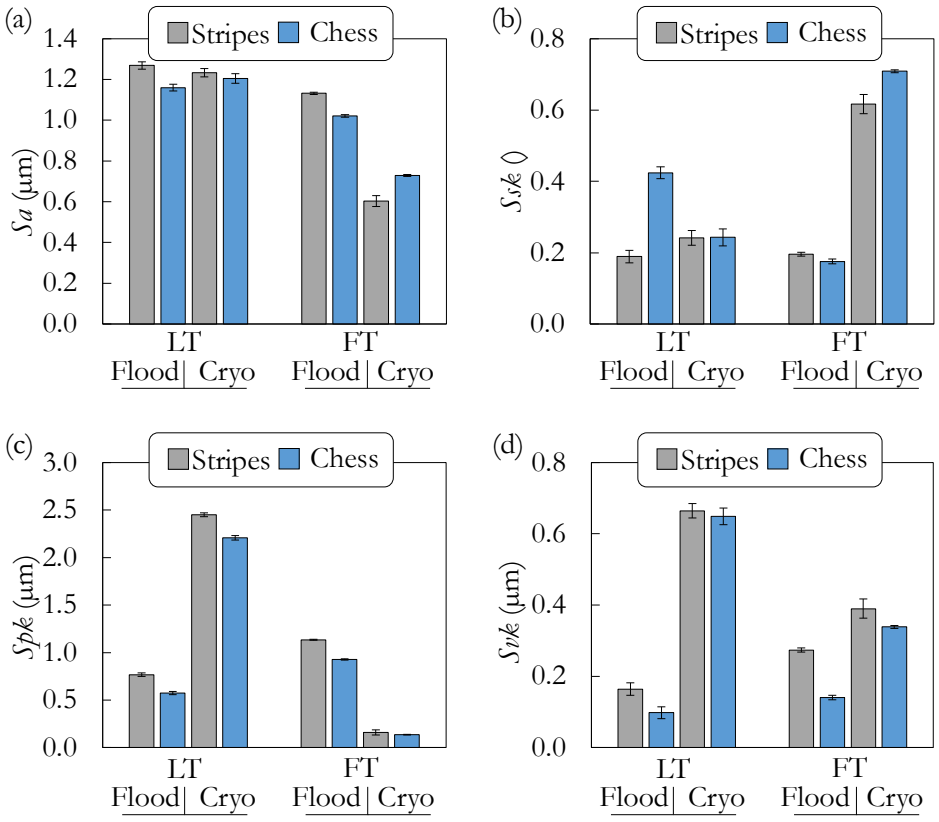

Figure 4.37: Surface roughness parameters of the machined surfaces.

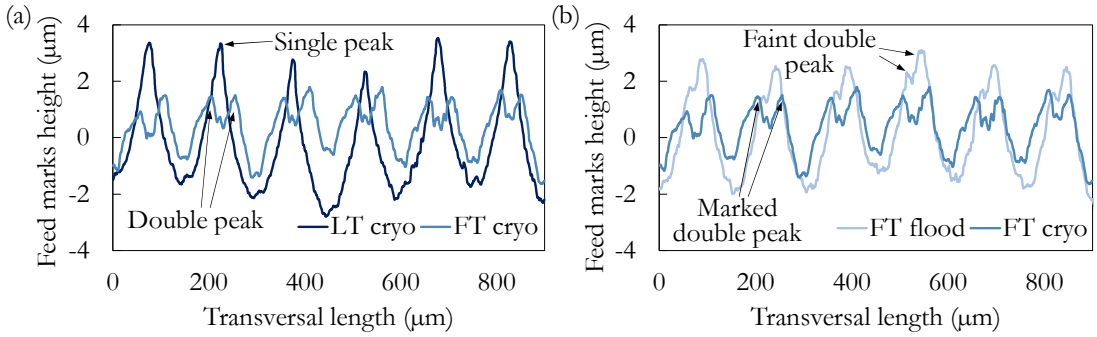

Figure 4.38: Comparison of the roughness profiles of the feed marks in longitudinal turning and face turning under cryogenic cooling (a), and in face turning under flood and cryogenic conditions (b).

To understand the influence of the scanning strategy and cutting direction on the surface topography, the αGBs density must be considered also in this case. As discussed above, in bars manufactured with the chessboard scanning strategy the density of the weak αGBs was higher, which may have reduced the cutting forces, and, in turn, the surface roughness, as actually occurred. As previously stated, the αGBs effect was especially noticeable in face turning operations, since the cutting edge encounters the weak αGBs more often than it does during longitudinal turning, as if it were in contact with a material with lower shear strength. This

suggests why the *Sa* values measured in facing operations were lower than those measured in longitudinal turning, as well as why the *Sa* values found in facing were more sensitive to the different scanning strategy.

For what concerns the cooling condition effect, the cryogenic cooling reduced the surface roughness *Sa* by 18% with respect to the flood condition, while it had the opposite effect on the other areal parameters, with a great increase especially of the *Ssk* parameter (+202%). Therefore, cryogenic cutting led to machined surfaces dominated by high peaks and great valleys, even if overall the roughness reduced. When considering the roughness profile of the feed marks, it was noticed that face turning led to the formation of a double peak, while longitudinal turning led to neat peaks, as showed in **Figure 4.38 (a)** for the cryogenic condition. Both the peaks were more pronounced under cryogenic cooling condition with respect to the flood one, as visible in **Figure 4.38 (b)** for face turning. In the first case, this corresponded to reduced *Spk* and increased *Svk* values, with intermediate *Spk* values. In the case of longitudinal turning, the spiked peaks resulted in greater *Spk* and *Ssk* values, being the majority of the material located below the core roughness. This finding can be attributed to the lower cutting temperatures of the cryogenic condition, which hindered the local softening of the material peaks, confirming what was found in previous works on cryogenic machining [189,190]. The effect of the cryogenic cooling condition on the surface topography was especially observed between comparing the textures of the two cutting directions. In fact, when flood conditions were applied, the differences in the roughness parameters among the samples were lower. Probably the lower cutting temperatures avoided the plastic deformation of the workpiece while cutting, increasing the impact on cutting dynamics of the αGBs, as previously mentioned.

Surface defects

The SEM analyses of the machined surfaces revealed the presence of defects usually found on difficult-to-cut alloys surfaces, as shown in **Figure 4.39**. Besides the differences in surface topography between the samples obtained with different scanning strategies, no detectable differences were found in the SEM analyses of the machined surface defects. On the contrary, when considering the effect of the cutting direction, a higher incidence of smeared feed marks and adhered microparticles were observed in longitudinal turning, which usually occurs at increasing cutting temperature. These observations can be explained by the fact that material removal in facing is favored by the presence of αGBs that may have hindered excessive heat generation in the cutting zone. The major effect was given by the cooling condition, which led to the formation of greater matrix tearing and surface grooves. This is in accordance with the lower cutting temperatures characterizing this operation. **Figure 4.40** reports a chart with the summary of the defects entity.

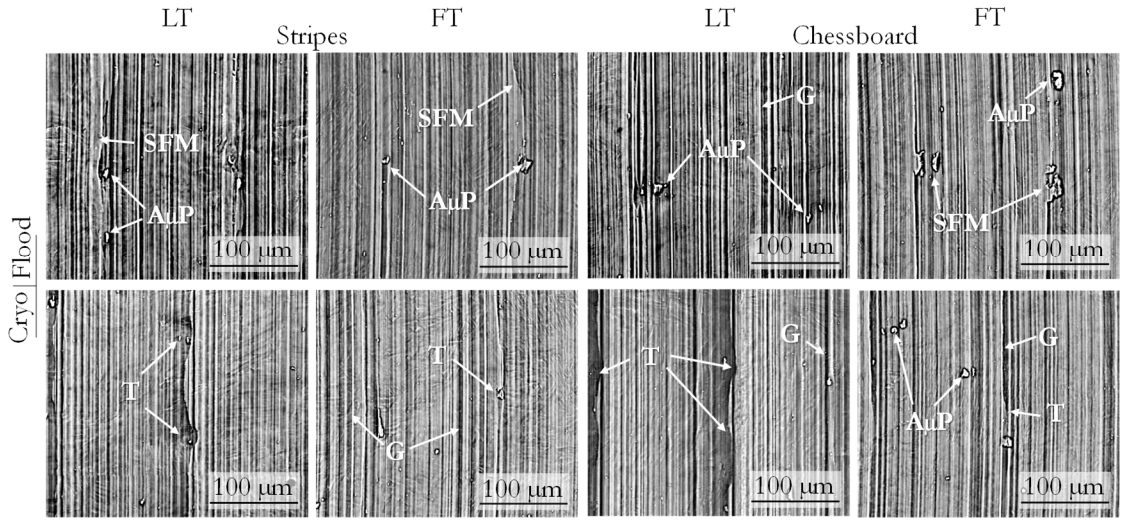

Figure 4.39: SEM images of the machined surface defects (AμP: adhered microparticles; SFM: smeared feed marks; T: tearing; G: grooves).

	Flood | Cryo (LT)		Flood | Cryo (FT)	
AμP	●●	●●	●	●●
SFM	●●	○	●	○
T	●	●●●	○	●●
G	●	●●	○	●●

Figure 4.40: Defects entity chart.

Conclusions

The most relevant conclusions follow:

- The scanning strategy had an impact on the size of the columnar grains (+44% grains width in the case of stripes with respect to chessboard) which is related to the material microhardness (−17% $HV_{0.05}$ in the case of stripes with respect to chessboard) and to the density of the αGB layers after heat treatment.
- The microstructural anisotropy deriving from the AM process greatly influenced the surface integrity of the machined samples both in terms of sub-surface (−35% SPD layer extent with −36% nanohardness in the case of stripes with respect to chessboard) and superficial features (overall stripes scanning strategy led to rougher and more spiky surfaces with respect to chessboard one).
- The weak αGBs promoted the material removal, especially when favorably oriented with respect to the cutting edge, allowing for a 28% reduction of the surface roughness and 61% reduction of peaks heights in the case of face turning rather than in longitudinal one.
- Cryogenic cooling emphasized the effect of the material anisotropy in determining the surface integrity.

Chapter 5

Conclusions

In this Ph.D. thesis general guidelines have been found to understand how the additive manufactured-induced anisotropy affects the machinability of L-PBFed Ti6Al4V alloy. The latter presented preferred grain growth direction along the build-up direction regardless of the build-up orientation angle or the geometry of the printed part. This induced a microstructural anisotropy that remained after the heat treatment. The AM process parameters such as build-up orientation and scanning strategy influenced the columnar grains size that is related to the material microhardness and to the density of the discontinuity zones of the material, i.e. αGB layers along the columnar grains which develop upon the heat treatment. The main effect was the one of the scanning strategies: stripes scanning strategy led to a + 44% columnar grains width than the chessboard one. This induced a microhardness reduction by 17% in the case of stripes strategy than the chessboard and to the decrease in the αGB layers density. The microstructural anisotropy deriving from the AM process greatly influenced the machinability in both milling and turning operations. The weak αGBs and the α lamellae colonies promoted the material removal when favorably oriented respect to the cutting edge. In the case of flat end milling and turning operations, the best machinability was obtained when cutting the sample surface perpendicular to the build-up direction, whilst in ball end milling, AMed surfaces at 45° respect to the build-up direction reported better machinability than the wrought alloy. In particular, the flat end mills life decreases gradually, up to 40%, going from machining samples horizontally oriented respect to the base platform to vertically oriented samples. This led to a progressive worsening of the workpiece quality both in terms of surface topography and burrs extent. The results are related to the microstructural anisotropy of the samples: when the registration angle of the tool is parallel to the αGB layers, the material removal is favored because the cutting forces decrease (- 14%). When analyzing surface finish at varying cutting parameters in flat end milling operations, it was found that, the machined surface of the horizontally oriented samples presented higher variations of areal texture parameters since the entity of the interaction between the cutting edge and the αGBs is preponderant than when machining the vertically oriented ones. In fact, in the former case the cutting edge is parallel to the weak αGBs, and may come into contact with them more frequently than in the latter case. Generally, the horizontally and vertically oriented samples led to machined surfaces with comparable surface roughness *Sa*. However, the horizontally oriented samples were dominated by higher peaks (positive *Ssk* and high *Spk*) and higher complexity (higher *Sdq*), particularly at the highest feed per tooth. The texture parameter that most distinguished the machined surfaces of the two build-up orientations was the skewness *Ssk*, which was on average positive for the horizontally oriented samples and negative for the vertically oriented ones. Therefore, the horizontally oriented samples reported a more prominent surface texture, but the burrs height was 16% lower for the horizontally oriented samples than the vertically oriented ones. Ball end milling operations carried out both on L-PBFed and wrought Ti6Al4V inclined surfaces highlighted the worse machinability of the former than the latter. In fact, the AMed workpieces led to higher cutting forces together with higher surface roughness and more prominent tool marks, but a lower quantity of adhered material than the wrought ones. However, the AMed and wrought alloys showed an inverted trend in machinability when machining the 45° workpieces in horizontally upward milling, leading to lower cutting forces, lower surface roughness, and less prominent tool marks in the case of AMed workpieces. The better machinability shown by such AMed workpieces is ascribed to their microstructural

features, namely α phase colonies tangential to the cutting, which favor the material removal by locally lowering the material resistance to deformation. The different machinability of the two alloys was clear only when machining with the highest depth of cut, since the microstructural anisotropy had a much less effect when a smaller depth of cut was utilized, inducing the AMed and wrought alloys to behave approximately the same. The microstructural anisotropy deriving from the AM process greatly influenced the surface integrity in turning operations. In particular, the extent of the severe plastically deformed layer was lower by 35% in the case of stripes scanning strategy with respect to the chessboard one, with −36% nanohardness. Overall stripes scanning strategy led to rougher and more spiky surfaces with respect to chessboard one. The weak αGBs promoted the material removal, when favorably oriented with respect to the cutting edge, allowing for a 28% reduction of the surface roughness and 61% reduction of peaks height in the case of face turning rather than in longitudinal turning. Cryogenic cooling emphasized the differences between the two cutting directions, i.e. longitudinal and face turning. In fact, the differences in roughness parameters among the samples were minor when flood conditions were applied. This result can be related to the lower cutting temperatures characterizing the cryogenic operations, which limits the material plastic deformation while cutting, enhancing the influence played by the material anisotropy in determining the surface integrity.

The results obtained so far make clear that, when machining AMed alloys, the anisotropy of the microstructure cannot be ignored to evaluate the machining performances. The findings of this research on the machinability of L-PBFed Ti6Al4V samples represent a step forward into the interpretation of the AMed parts machinability, by establishing a link between their mechanical properties and the mechanics of chip formation. The overall results can provide useful guidance in industries involved in the use of AM, to design both the AM and machining processes to obtain efficient production of high-quality AMed parts.

To further investigate the effect of the AM-induced anisotropy on machinability it would be useful to assess which and how other AM process parameters affects the columnar grains size and how the machinability comply with different cutting parameters. Most of all, it would be helpful to assess if the findings of this study on the L-PBFed Ti6Al4V are confirmed if other AM technologies are used, understanding how the microstructure of other metal alloys is affected by AM and how does it influence the machinability.

References

[1] Gu D. Laser Additive Manufacturing of High-Performance Materials. 1st ed. Springer-Verlag Berlin Heidelberg; 2015.

[2] EOS history n.d. https://www.eos.info/en/about-us/history (accessed July 30, 2021).

[3] Arcam EBM n.d. https://www.ge.com/additive/who-we-are/about-arcam (accessed July 30, 2021).

[4] Metal Additive Manufactruing history n.d. https://additive-manufacturing-report.com/technology/metal/metal-additive-manufacturing-history/ (accessed July 30, 2021).

[5] Senvol Database n.d. http://senvol.com/material-search/ (accessed August 2, 2021).

[6] AMPOWER Report - Additive Manufacturing Report n.d. https://additive-manufacturing-report.com (accessed August 2, 2021).

[7] Metal Additive Manufacturing Market by Application and Geography - Forecast and Analysis 2020-2024 2020. https://www.technavio.com/report/metal-additive-manufacturing-market-industry-analysis (accessed August 5, 2021).

[8] Wohlers Report 2019 3D Printing and Additive Manufacturing - State of the Industry. 2019.

[9] Wohlers Report 2021 3D Printing and Additive Manufacturing - Global State of the Industry. 2021.

[10] Case study: hydraulic crossing n.d. https://www.metal-am.com/introduction-to-metal-additive-manufacturing-and-3d-printing/case-study-hydraulic-crossing/ (accessed August 2, 2021).

[11] Maconachie T, Leary M, Lozanovski B, Zhang X, Qian M, Faruque O, et al. SLM lattice structures : Properties , performance , applications and challenges. Mater Des 2019;183:108137.

[12] Atzeni E, Salmi A. Economics of additive manufacturing for end-usable metal parts. Int J Adv Manuf Technol 2012;62:1147–55.

[13] DebRoy T, Wei HL, Zuback JS, Mukherjee T, Elmer JW, Milewski JO, et al. Additive manufacturing of metallic components – Process, structure and properties. Prog Mater Sci 2018;92:112–224.

[14] Liu S, Shin YC. Additive manufacturing of Ti6Al4V alloy: A review. Mater Des 2019;164:8–12.

[15] Thompson SM, Bian L, Shamsaei N, Yadollahi A. An overview of Direct Laser Deposition for additive manufacturing ; Part I : Transport phenomena , modeling and diagnostics. Addit Manuf 2015;8:36–62.

[16] Cabanettes F, Joubert A, Chardon G, Dumas V, Rech J, Grosjean C, et al. Topography of as built surfaces generated in metal additive manufacturing: A multi scale analysis from form to roughness. Precis Eng 2018;52:249–65.

[17] Singla AK, Banerjee M, Sharma A, Singh J, Bansal A, Gupta MK, et al. Selective laser melting of Ti6Al4V alloy: Process parameters, defects and post-treatments. J Manuf Process 2021;64:161–87.

[18] Jiménez M, Romero L, Domínguez IA, Espinosa MDM, Domínguez M. Additive Manufacturing Technologies: An Overview about 3D Printing Methods and Future Prospects. Complexity 2019;2019.

[19] Vrancken B, Thijs L, Kruth JP, Van Humbeeck J. Heat treatment of Ti6Al4V produced by Selective Laser Melting: Microstructure and mechanical properties. J Alloys Compd 2012;541:177–85.

[20] Pragana JPM, Sampaio RFV, Bragança IMF, Silva CMA, Martins PAF. Hybrid metal additive manufacturing: A state–of–the-art review. Adv Ind Manuf Eng 2021;2:100032.

[21] Kok Y, Tan XP, Wang P, Nai MLS, Loh NH, Liu E, et al. Anisotropy and heterogeneity of microstructure and mechanical properties in metal additive manufacturing: A critical review. Mater Des 2018;139:565–86.

[22] Gorsse S, Hutchinson C, Gouné M, Banerjee R. Additive manufacturing of metals: a brief review of the characteristic microstructures and properties of steels, Ti-6Al-4V and high-entropy alloys. Sci Technol Adv Mater 2017;18:584–610.

[23] ASTM 52904: Additive manufacturing - Process characteristics and performance - Practice for metal powder bed fusion process to meet critical applications n.d.

[24] Guo P, Zou B, Huang C, Gao H. Study on microstructure, mechanical properties and machinability of efficiently additive manufactured AISI 316L stainless steel by high-power direct laser deposition. J Mater Process Technol 2017;240:12–22.

[25] Bai Y, Zhao C, Yang J, Hong R, Weng C, Wang H. Microstructure and machinability of selective laser melted high-strength maraging steel with heat treatment. J Mater Process Technol 2021;288:116906.

[26] Fortunato A, Lulaj A, Melkote S, Liverani E, Ascari A, Umbrello D. Milling of maraging steel components produced by selective laser melting. Int J Adv Manuf Technol 2018;94:1895–902.

[27] Ning J, Liang SY. Predictive Modeling of Machining Temperatures with Force – Temperature Correlation Using Cutting Mechanics and Constitutive Relation. Materials (Basel) 2019;12.

[28] Segebade E, Gerstenmeyer M, Dietrich S, Zanger F, Schulze V. Influence of anisotropy of additively manufactured AlSi10Mg parts on chip formation during orthogonal cutting. Procedia CIRP 2019;82:113–8.

[29] Jarosz K, Patel K V., Özel T. Mechanistic force modeling in finish face milling of additively manufactured Inconel 625 nickel-based alloy. Int J Adv Manuf Technol 2020;111:1535–51.

[30] Sunny S, Gleason G, Bailey K, Mathews R, Malik A. Importance of microstructure modeling for additively manufactured metal post-process simulations. Int J Eng Sci 2021;166:103515.

[31] ISO/ASTM 52900: Additive manufacturing — General principles — Terminology 2017:1–19.

[32] Ziaee M, Crane NB. Binder jetting: A review of process, materials, and methods. Addit

Manuf 2019;28:781–801.

[33] Gokuldoss PK, Kolla S, Eckert J. Additive manufacturing processes: Selective laser melting, electron beam melting and binder jetting-selection guidelines. Materials (Basel) 2017;10.

[34] Friel RJ. Metal Sheet Lamination – Ultrasonic. Ref Modul Mater Sci Mater Eng 2021.

[35] Bhavar V, Kattire P, Patil V, Khot S, Gujar K, Singh R. A review on powder bed fusion technology of metal additive manufacturing. Addit. Manuf. Handb. First, CRC press; 2017.

[36] Gibson I, Rosen D, Stucker B. Directed Energy Deposition Processes. Addit. Manuf. Technol. Second, New York, NY: Springer; 2015, p. 245–68.

[37] Koike R, Takemura S, Kakinuma Y, Kondo M. Enhancement of powder supply efficiency in directed energy deposition based on gas-solid multiphase-flow simulation. Procedia CIRP 2018;78:133–7.

[38] Lee H-J, Ahn D-G. Investigation of Elimination of Powder Spreading in Manufacture of Thin and Wide Preheating Beads from Co-Cr Alloy Powders Using a P-ebeam. J Mater Res Technol 2021;14:1873–83.

[39] Digital Alloys' Guide to Metal Additive Manufacturing - Economics of Metal Additive Manufacturing 2019. https://www.digitalalloys.com/blog/economics-metal-additive-manufacturing/ (accessed August 4, 2021).

[40] Herzog D, Seyda V, Wycisk E, Emmelmann C. Additive manufacturing of metals. Acta Mater 2016;117:371–92.

[41] Bruzzo F, Catalano G, Demir AG, Previtali B. In-process laser re-melting of thin walled parts to improve surface quality after laser metal deposition. Key Eng Mater 2019;813 KEM:191–6.

[42] Lizzul L, Sorgato M, Bertolini R, Ghiotti A, Bruschi S, Fabbro F, et al. On the influence of laser cladding parameters and number of deposited layers on as-built and machined AISI H13 tool steel multilayered claddings. CIRP J Manuf Sci Technol 2021;35:361–70.

[43] Childerhouse T, Hernández-Nava E, Tapoglou N, M'Saoubi R, Franca L, Leahy W, et al. The influence of finish machining depth and hot isostatic pressing on defect distribution and fatigue behaviour of selective electron beam melted Ti-6Al-4V. Int J Fatigue 2021;147:1–11.

[44] Wüst P, Edelmann A, Hellmann R. Areal surface roughness optimization of maraging steel parts produced by hybrid additive manufacturing. Materials (Basel) 2020;13.

[45] Lu X, Chiumenti M, Cervera M, Li J, Lin X, Ma L, et al. Substrate design to minimize residual stresses in Directed Energy Deposition AM processes. Mater Des 2021;202:109525.

[46] Hrabe N, Gnäupel-Herold T, Quinn T. Fatigue properties of a titanium alloy (Ti–6Al–4V) fabricated via electron beam melting (EBM): Effects of internal defects and residual stress. Int J Fatigue 2017;94:202–10.

[47] Sochalski-Kolbus LM, Payzant EA, Cornwell PA, Watkins TR, Babu SS, Dehoff RR, et al. Comparison of Residual Stresses in Inconel 718 Simple Parts Made by Electron Beam Melting and Direct Laser Metal Sintering. Metall Mater Trans A Phys Metall Mater Sci 2015;46:1419–32.

[48] Lee H, Huat C, Lim J, Low MJ, Tham N, Matham Murukeshan V, et al. Lasers in Additive Manufacturing: A Review. Int J Precis Eng Manuf Technol 2017;4:307.

[49] Cobbinah PV, Nzeukou RA, Onawale OT, Matizamhuka WR. Laser powder bed fusion of potential superalloys: A review. Metals (Basel) 2021;11:1–37.

[50] Zhang B, Li Y, Bai Q. Defect Formation Mechanisms in Selective Laser Melting: A Review. Chinese J Mech Eng (English Ed 2017;30:515–27.

[51] Kruth JP, Levy G, Klocke F, Childs THC. Consolidation phenomena in laser and powder-bed based layered manufacturing. CIRP Ann - Manuf Technol 2007;56:730–59.

[52] Attar H, Ehtemam-Haghighi S, Kent D, Dargusch MS. Recent developments and opportunities in additive manufacturing of titanium-based matrix composites: A review. Int J Mach Tools Manuf 2018;133:85–102.

[53] Vafadar A, Guzzomi F, Rassau A, Hayward K. Advances in metal additive manufacturing: A review of common processes, industrial applications, and current challenges. Appl Sci 2021;11:1–33.

[54] Doubenskaia M, Domashenkov A, Smurov I, Petrovskiy P. Study of Selective Laser Melting of intermetallic TiAl powder using integral analysis. Int J Mach Tools Manuf 2018;129:1–14.

[55] Everton SK, Hirsch M, Stavroulakis PI, Leach RK, Clare AT. Review of in-situ process monitoring and in-situ metrology for metal additive manufacturing. Mater Des 2016;95:431–45.

[56] Yadroitsev I, Gusarov A, Yadroitsava I, Smurov I. Single track formation in selective laser melting of metal powders. J Mater Process Technol 2010;210:1624–31.

[57] Spierings AB, Herres N, Levy G. Influence of the particle size distribution on surface quality and mechanical properties in AM steel parts. Rapid Prototyp J 2011;17:195–202.

[58] Sun S, Brandt M, Easton M. Powder bed fusion processes: An overview. Elsevier Ltd; 2017.

[59] Anderson IE, Figliola RS, Morton H. Flow mechanisms in high pressure gas atomization. Mater Sci Eng A 1991;148:101–14.

[60] Entezarian M, Allaire F, Tsantrizos P, Drew RAL. Plasma atomization: A new process for the production of fine, spherical powders. JOM 1996 486 1996;48:53–5.

[61] Champagne B, Angers R. Fabrication of powders by the rotating electrode process. J Powder Met Powder Technol 1980;16:359–67.

[62] Qi H, Azer M, Ritter A. Studies of Standard Heat Treatment Effects on Microstructure and Mechanical Properties of Laser Net Shape Manufactured INCONEL 718. Metall Mater Trans A Phys Metall Mater Sci 2009;40A.

[63] Seifi M, Salem A, Beuth J, Harrysson OLA, Lewandowski JJ. Overview of Materials Qualification Needs for Metal Additive Manufacturing. JOM 2016;68:747–64.

[64] Aboulkhair NT, Everitt NM, Ashcroft I, Tuck C. Reducing porosity in AlSi10Mg parts processed by selective laser melting. Addit Manuf 2014;1:77–86.

[65] Lee S, Kim J, Shim DS, Park SH, Choi YS. Micro-Cracking in Medium-Carbon Steel Layers Additively Deposited on Gray Cast Iron Using Directed Energy Deposition. Met Mater Int 2020;26:708–18.

[66] Delgado J, Ciurana J, Serenó L. Comparison of forming manufacturing processes and selective laser melting technology based on the mechanical properties of products. Virtual Phys Prototyp 2011;6:37–41.

[67] Tang M, Pistorius PC. Oxides, porosity and fatigue performance of AlSi10Mg parts produced by selective laser melting. Int J Fatigue 2017;94:192–201.

[68] Kempen K, Thijs L, Van Humbeeck J, Kruth JP. Mechanical Properties of AlSi10Mg Produced by Selective Laser Melting. Phys Procedia 2012;39:439–46.

[69] Thijs L, Kempen K, Kruth JP, Van Humbeeck J. Fine-structured aluminium products with controllable texture by selective laser melting of pre-alloyed AlSi10Mg powder. Acta Mater 2013;61:1809–19.

[70] Fayazfar H, Salarian M, Rogalsky A, Sarker D, Russo P, Paserin V, et al. A critical review of powder-based additive manufacturing of ferrous alloys: Process parameters, microstructure and mechanical properties. Mater Des 2018;144:98–128.

[71] Wang J, Liu S, Fang Y, He Z. A short review on selective laser melting of H13 steel. Int J Adv Manuf Technol 2020;108:2453–66.

[72] Lee J, Choe J, Park J, Yu JH, Kim S, Jung ID, et al. Microstructural effects on the tensile and fracture behavior of selective laser melted H13 tool steel under varying conditions. Mater Charact 2019;155:109817.

[73] Ren B, Lu D, Zhou R, Li Z, Guan J. Preparation and mechanical properties of selective laser melted H13 steel. J Mater Res 2019;34:1415–25.

[74] Mutua J, Nakata S, Onda T, Chen ZC. Optimization of selective laser melting parameters and influence of post heat treatment on microstructure and mechanical properties of maraging steel. Mater Des 2018;139:486–97.

[75] Ziętala M, Durejko T, Polański M, Kunce I, Płociński T, Zieliński W, et al. The microstructure, mechanical properties and corrosion resistance of 316 L stainless steel fabricated using laser engineered net shaping. Mater Sci Eng A 2016;677:1–10.

[76] Sun Z, Tan X, Tor SB, Yeong WY. Selective laser melting of stainless steel 316L with low porosity and high build rates. Mater Des 2016;104:197–204.

[77] Yap CY, Chua CK, Dong ZL, Liu ZH, Zhang DQ, Loh LE, et al. Review of selective laser melting: Materials and applications. Appl Phys Rev 2015;2.

[78] Vilaro T, Colin C, Bartout JD, Nazé L, Sennour M. Microstructural and mechanical approaches of the selective laser melting process applied to a nickel-base superalloy. Mater Sci Eng A 2012;534:446–51.

[79] Qiu C, Adkins NJE, Attallah MM. Selective laser melting of Invar 36 : Microstructure and properties. Acta Mater 2016;103:382–95.

[80] Zhang LC, Attar H. Selective Laser Melting of Titanium Alloys and Titanium Matrix Composites for Biomedical Applications: A Review. Adv Eng Mater 2016;18:463–75.

[81] Chlebus E, Kuźnicka B, Kurzynowski T, Dybała B. Microstructure and mechanical behaviour of Ti-6Al-7Nb alloy produced by selective laser melting. Mater Charact 2011;62:488–95.

[82] Zhang LC, Klemm D, Eckert J, Hao YL, Sercombe TB. Manufacture by selective laser melting and mechanical behavior of a biomedical Ti-24Nb-4Zr-8Sn alloy. Scr Mater 2011;65:21–4.

[83] Rack HJ, Qazi JI. Titanium alloys for biomedical applications. Mater Sci Eng C 2006;26:1269–77.

[84] ASTM F1472 - 20a: Standard Specification for Wrought Titanium-6Aluminum-4Vanadium Alloy for Surgical Implant Applications n.d.

[85] Titanium Consulting & Trading: wrought Ti6Al4V grade 5 annealed n.d. http://www.tct.it/assets/titanium-ti6al4v-astm-gr-5---annealed.pdf (accessed August 20, 2021).

[86] Morri A. Trattamenti termici delle leghe di titanio α+β, correlazioni fra microstruttura e comportamento meccanico. Metall Ital 2008;100:1–10.

[87] Thijs L, Montero Sistiaga ML, Wauthle R, Xie Q, Kruth JP, Van Humbeeck J. Strong morphological and crystallographic texture and resulting yield strength anisotropy in selective laser melted tantalum. Acta Mater 2013;61:4657–68.

[88] de Formanoir C, Michotte S, Rigo O, Germain L, Godet S. Electron beam melted Ti-6Al-4V: Microstructure, texture and mechanical behavior of the as-built and heat-treated material. Mater Sci Eng A 2016;652:105–19.

[89] Wang T, Zhu YY, Zhang SQ, Tang HB, Wang HM. Grain morphology evolution behavior of titanium alloy components during laser melting deposition additive manufacturing. J Alloys Compd 2015;632:505–13.

[90] Thijs L, Verhaeghe F, Craeghs T, Humbeeck J Van, Kruth JP. A study of the microstructural evolution during selective laser melting of Ti-6Al-4V. Acta Mater 2010;58:3303–12.

[91] Kobryn PA, Semiatin SL. Microstructure and texture evolution during solidification processing of Ti–6Al–4V. J Mater Process Technol 2003;135:330–9.

[92] Vilaro T, Colin C, Bartout JD. As-fabricated and heat-treated microstructures of the Ti-6Al-4V alloy processed by selective laser melting. Metall Mater Trans A Phys Metall Mater Sci 2011;42:3190–9.

[93] ASTM F3301-18a: Additive Manufacturing – Post Processing Methods – Standard Specification for Thermal Post-Processing Metal Parts Made Via Powder Bed Fusion n.d.

[94] Simonelli M, Tse YY, Tuck C. Effect of the build orientation on the mechanical properties and fracture modes of SLM Ti-6Al-4V. Mater Sci Eng A 2014;616:1–11.

[95] Carroll BE, Palmer TA, Beese AM. Anisotropic tensile behavior of Ti-6Al-4V components fabricated with directed energy deposition additive manufacturing. Acta Mater 2015;87:309–20.

[96] Sharma H, Parfitt D, Syed AK, Wimpenny D, Muzangaza E, Baxter G, et al. A critical evaluation of the microstructural gradient along the build direction in electron beam melted Ti-6Al-4V alloy. Mater Sci Eng A 2019;744:182–94.

[97] Rahmati S, Vahabli E. Evaluation of analytical modeling for improvement of surface roughness of FDM test part using measurement results. Int J Adv Manuf Technol 2015 795 2015;79:823–9.

[98] Liu H, Li M, Qin X, Huang S, Hong F. Numerical simulation and experimental analysis of wide-beam laser cladding. Int J Adv Manuf Technol 2019;100:237–49.

[99] Gunenthiram V, Peyre P, Schneider M, Dal M, Coste F, Fabbro R, et al. Analysis of

laser-melt pool-powder bed interaction during the selective laser melting of a stainless steel. J Laser Appl 2017;29.

[100] Khairallah SA, Anderson AT, Rubenchik A, King WE. Laser powder-bed fusion additive manufacturing: Physics of complex melt flow and formation mechanisms of pores, spatter, and denudation zones. Acta Mater 2016;108:36–45.

[101] Thompson A, Senin N, Leach RK. Towards an additive surface atlas. Proc - ASPE/Euspen 2016 Summer Top Meet Dimens Accuracy Surf Finish Addit Manuf 2016:156–61.

[102] Dumas M, Cabanettes F, Kaminski R, Valiorgue F, Picot E, Lefebvre F, et al. Influence of the the finish cutting operations on the the fatigue performance of Ti-6Al-4V parts produced by Selective Laser Melting. Procedia CIRP 2018;71:429–34.

[103] Grzesik W. Advanced Machining Processes of Metallic Materials: Theory, Modelling, and Applications. second. Elsevier; 2017.

[104] Stephenson DA, Agapiou JS. Metal Cutting Theory and Practice. 3rd ed. CRC Press; 2018.

[105] ISO 8688-2: Tool life testing in milling - End milling n.d.

[106] ISO 3685: Tool-life testing with single-point turning tools 1993.

[107] Patil Amit S, Ingle sushil V, More Yogesh S, S NM. Machining Challenges in Ti-6Al-4V . -A Review. Int J Innov Eng Technol 2015;5:6–23.

[108] Ezugwu EO, Wang ZM. Materials Processing Technology Titanium alloys and their machinability a review. J Mater Process Technol 1997;68.

[109] Jianxin D, Yousheng L, Wenlong S. Diffusion wear in dry cutting of Ti-6Al-4V with WC/Co carbide tools. Wear 2008;265:1776–83.

[110] Toenshoff HK, Denkena B. Basics of Cutting and Abrasive Processes. 1st ed. Springer-Verlag Berlin Heidelberg; 2013.

[111] Molinari A, Musquar C, Sutter G. Adiabatic shear banding in high speed machining of Ti-6Al-4V: Experiments and modeling. Int J Plast 2002;18:443–59.

[112] Vyas A, Shaw MC. Mechanics of Saw-Tooth Chip Formation in Metal Cutting. J Manuf Sci Eng 1999;121:163–72.

[113] Grzesik W. Prediction of the Functional Performance of Machined Components Based on Surface Topography: State of the Art. J Mater Eng Perform 2016;25:4460–8.

[114] Ahsan KB, Mazid AM, Pang GKH. Morphological investigation of Ti-6Al-4V chips produced by conventional turning. Int J Mach Mach Mater 2016;18:138–54.

[115] Arrazola P, Garay A, Iriarte LM, Armendia M, Arrazola P, Garay A, et al. Machinability of Titanium alloys (Ti6Al4V and Ti555.3). J Mater Process Technol 2009;209:2223–30.

[116] Shivpuri R, Hua J, Mittal P, Srivastava AK, Lahoti GD. Microstructure-Mechanics Interactions in Modeling Chip Segmentation during Titanium Machining. CIRP Ann 2002;51:71–4.

[117] Özel T, Hsu TK, Zeren E. Effects of cutting edge geometry, workpiece hardness, feed rate and cutting speed on surface roughness and forces in finish turning of hardened AISI H13 steel. Int J Adv Manuf Technol 2005;25:262–9.

[118] Polishetty A, Shunmugavel M, Goldberg M, Littlefair G, Singh RK. Cutting Force and

Surface Finish Analysis of Machining Additive Manufactured Titanium Alloy Ti-6Al-4V. Procedia Manuf 2017;7:284–9.

[119] Kumar R, Kumar Sahooa A, Satyanarayana K, Venkateswara Rao G. Some studies on cutting force and temperature in machining Ti-6AL-4V alloy using regression analysis and ANOVA. Int J Ind Eng Comput 2013;4:427–36.

[120] Chen Y, Li H, Wang J. Cutting forces and tool wear in dry milling of Ti6Al4V. Adv Mater Res 2012;565:454–9.

[121] Ítalo Sette Antonialli A, Eduardo Diniz A, Pederiva R. Vibration analysis of cutting force in titanium alloy milling. Int J Mach Tools Manuf 2010;50:65–74.

[122] Ulutan D, Ozel T. Machining induced surface integrity in titanium and nickel alloys : A review. Int J Mach Tools Manuf 2011;51:250–80.

[123] Jawahir IS, Brinksmeier E, M'Saoubi R, Aspinwall DK, Outeiro JC, Meyer D, et al. Surface integrity in material removal processes: Recent advances. CIRP Ann - Manuf Technol 2011;60:603–26.

[124] Felhő C, Kundrák J. Effects of Setting Errors (Insert Run-Outs) on Surface Roughness in Face Milling When Using Circular Inserts. Mach 2018, Vol 6, Page 14 2018;6:14.

[125] Benardos PG, Vosniakos GC. Prediction of surface roughness in CNC face milling using neural networks and Taguchi's design of experiments. Robot Comput Integr Manuf 2002;18:343–54.

[126] Ginting A, Nouari M. Surface integrity of dry machined titanium alloys. Int J Mach Tools Manuf 2009;49:325–32.

[127] Da Silva LRR, Filho AF, Costa ES, Marcucci Pico DF, Sales WF, Guesser WL, et al. Cutting Temperatures in End Milling of Compacted Graphite Irons. Procedia Manuf 2018;26:474–84.

[128] Brown M, Crawforth P, M'Saoubi R, Larsson T, Wynne B, Mantle A, et al. Quantitative characterization of machining-induced white layers in Ti–6Al–4V. Mater Sci Eng A 2019;764:138220.

[129] Niknam SA, Songmene V. Milling burr formation, modeling and control: A review. Proc Inst Mech Eng Part B J Eng Manuf 2015;229:893–909.

[130] Rodrigues AR, Jasinevicius RG. Machining scale: Workpiece grain size and surface integrity in micro end milling. Elsevier Ltd; 2016.

[131] Said Z, Gupta M, Hegab H, Arora N, Khan AM, Jamil M, et al. A comprehensive review on minimum quantity lubrication (MQL) in machining processes using nano-cutting fluids. Int J Adv Manuf Technol 2019;105:2057–86.

[132] Boswell B, Islam MN, Davies IJ, Ginting YR, Ong AK. A review identifying the effectiveness of minimum quantity lubrication (MQL) during conventional machining. Int J Adv Manuf Technol 2017;92:321–40.

[133] Weinert K, Inasaki I, Sutherland JW, Wakabayashi T. Dry Machining and Minimum Quantity Lubrication. CIRP Ann 2004;53:511–37.

[134] Priarone PC, Robiglio M, Settineri L, Tebaldo V. Milling and Turning of Titanium Aluminides by Using Minimum Quantity Lubrication. Procedia CIRP 2014;24:62–7.

[135] Hong SY, Ding Y, Jeong W cheol. Friction and cutting forces in cryogenic machining

of Ti–6Al–4V. Int J Mach Tools Manuf 2001;41:2271–85.

[136] Sartori S, Pezzato L, Dabalà M, Maurizi Enrici T, Mertens A, Ghiotti A, et al. Surface Integrity Analysis of Ti6Al4V After Semi-finishing Turning Under Different Low-Temperature Cooling Strategies. J Mater Eng Perform 2018;27:4810–8.

[137] Fernandez-Zelaia P, Nguyen V, Zhang H, Kumar A, Melkote SN. The effects of material anisotropy on secondary processing of additively manufactured CoCrMo. Addit Manuf 2019;29:100764.

[138] Schroepfer D, Treutler K, Boerner A, Gustus R, Kannengiesser T, Wesling V, et al. Surface finishing of hard-to-machine cladding alloys for highly stressed components 2021:1427–42.

[139] Litwa P, Hernandez-Nava E, Guan D, Goodall R, Wika KK. The additive manufacture processing and machinability of CrMnFeCoNi high entropy alloy. Mater Des 2021;198:109380.

[140] Zhao Y, Sun J, Li J. Study on chip morphology and milling characteristics of laser cladding layer. Int J Adv Manuf Technol 2015;77:783–96.

[141] Hojati F, Daneshi A, Soltani B, Azarhoushang B, Biermann D. Study on machinability of additively manufactured and conventional titanium alloys in micro-milling process. Precis Eng 2020;62:1–9.

[142] Ni C, Zhu L, Zheng Z, Zhang J, Yang Y, Hong R, et al. Effects of machining surface and laser beam scanning strategy on machinability of selective laser melted Ti6Al4V alloy in milling. Mater Des 2020;194:108880.

[143] Milton S, Morandeau A, Chalon F, Leroy R. Influence of Finish Machining on the Surface Integrity of Ti6Al4V Produced by Selective Laser Melting. Procedia CIRP 2016;45:127–30.

[144] Shunmugavel M, Polishetty A, Goldberg M, Littlefair G. Tool Wear and Surface Integrity Analysis of Machined Heat Treated Selective Laser Melted Ti-6Al-4V. Int J Mater Form Mach Process 2016;3.

[145] Sartori S, Moro L, Ghiotti A, Bruschi S. On the tool wear mechanisms in dry and cryogenic turning Additive Manufactured titanium alloys. Tribol Int 2017;105:264–73.

[146] Shunmugavel M, Polishetty A, Goldberg M, Nomani J, Littlefair G. Influence of build orientation on machinability of selective laser melted titanium alloy-Ti-6Al-4V. World Acad Sci Eng Technol Int J Chem Mol Nucl Mater Metall Eng 2017;11:515–519.

[147] Oyelola O, Crawforth P, M'Saoubi R, Clare AT. Machining of Additively Manufactured Parts: Implications for Surface Integrity. Procedia CIRP 2016;45:119–22.

[148] MYSINT100, 3D selective laser fusion printer for metal powder n.d. https://www.sisma.com/en/products/mysint100/ (accessed August 3, 2021).

[149] EOS M 280 n.d. https://store.eos.info/collections/refurbished-machines/products/eos-m-280 (accessed August 3, 2021).

[150] ASTM E112 - Standard Test Methods for Determining Average Grain Size 2013.

[151] ASTM E92: Standard Test Methods for Vickers Hardness and Knoop Hardness of Metallic Materials 2017.

[152] ISO 25178: Geometric Product Specifications (GPS) – Surface texture: areal n.d.

[153] Burger U, Kuttolamadom M, Bryan A, Mears L, Kurfess T. Volumetric flank wear characterization for titanium milling insert tools. Proc ASME Int Manuf Sci Eng Conf 2009, MSEC2009 2009;2:97–104.

[154] Ucun I, Aslantas K, Bedir F. An experimental investigation of the effect of coating material on tool wear in micro milling of Inconel 718 super alloy. Wear 2013;300:8–19.

[155] Sorgato M, Bertolini R, Bruschi S. On the correlation between surface quality and tool wear in micro–milling of pure copper. J Manuf Process 2020;50:547–60.

[156] Lizzul L, Sorgato M, Bertolini R, Ghiotti A, Bruschi S. Influence of additive manufacturing-induced anisotropy on tool wear in end milling of Ti6Al4V. Tribol Int 2020;146:106200.

[157] Lizzul L, Sorgato M, Bertolini R, Ghiotti A, Bruschi S. Anisotropy effect of additively manufactured Ti6Al4V titanium alloy on surface quality after milling. Precis Eng 2021;67.

[158] Lizzul L, Sorgato M, Bertolini R, Ghiotti A, Bruschi S. Surface finish of additively manufactured Ti6Al4V workpieces after ball end milling. Procedia CIRP 2021;102:228–33.

[159] Lizzul L, Bertolini R, Ghiotti A, Bruschi S. Turning of Additively Manufactured Ti6Al4V: Effect of the Highly Oriented Microstructure on the Surface Integrity. Mater 2021, Vol 14, Page 2842 2021;14:2842.

[160] Jawaid A, Koksal S, Sharif S. Cutting performance and wear characteristics of PVD coated and uncoated carbide tools in face milling Inconel 718 aerospace alloy. J Mater Process Technol 2001;116:2–9.

[161] Turley DM. A scanning electron microscope study of attrition wear in tungsten carbide taper pin reamers. Wear 1974;27:259–66.

[162] Zheng L, Chen W, Huo D. Experimental investigation on burr formation in vibration-assisted micro-milling of Ti-6Al-4V. Proc Inst Mech Eng Part C J Mech Eng Sci 2019;233:4112–9.

[163] Ucun I, Aslantas K, Bedir F. The performance Of DLC-coated and uncoated ultra-fine carbide tools in micromilling of Inconel 718. Precis Eng 2015;41:135–44.

[164] Sun SH, Koizumi Y, Saito T, Yamanaka K, Li YP, Cui Y, et al. Electron beam additive manufacturing of Inconel 718 alloy rods: Impact of build direction on microstructure and high-temperature tensile properties. Addit Manuf 2018;23:457–70.

[165] Wang Y, Zou B, Wang J, Wu Y, Huang C. Effect of the progressive tool wear on surface topography and chip formation in micro-milling of Ti–6Al–4V using Ti(C7N3)-based cermet micro-mill. Tribol Int 2020;141:105900.

[166] Astakhov VP, Shvets S. The assessment of plastic deformation in metal cutting. J Mater Process Technol 2004;146:193–202.

[167] Ryu SH, Choi DK, Chu CN. Roughness and texture generation on end milled surfaces. Int J Mach Tools Manuf 2006;46:404–12.

[168] Saha S, Deb S, Bandyopadhyay PP. An analytical approach to assess the variation of lubricant supply to the cutting tool during MQL assisted high speed micromilling. J Mater Process Technol 2020;285.

[169] Niu Z, Jiao F, Cheng K. An innovative investigation on chip formation mechanisms in

micro-milling using natural diamond and tungsten carbide tools. J Manuf Process 2018;31:382–94.

[170] Ee KC, Balaji AK, Jawahir IS. Progressive tool-wear mechanisms and their effects on chip-curl/chip-form in machining with grooved tools: An extended application of the equivalent toolface (ET) model. Wear 2003;255:1404–13.

[171] Hamza HM, Deen KM, Haider W. Microstructural examination and corrosion behavior of selective laser melted and conventionally manufactured Ti6Al4V for dental applications. Mater Sci Eng C 2020;113:110980.

[172] Toh CK. Surface topography analysis in high speed finish milling inclined hardened steel. Precis Eng 2004;28:386–98.

[173] Spence AD, Altintas Y. Modeling Techniques and Control Architectures for Machining Intelligence. In: C.T. Leondes, editor. Control Dyn. Syst. vol 70, Elsevier; 1995, p. 243–89.

[174] Kull Neto H, Diniz AE, Pederiva R. The influence of cutting forces on surface roughness in the milling of curved hardened steel surfaces. Int J Adv Manuf Technol 2016;84:1209–18.

[175] Polli ML, Da Silva FF. Analysis of the dynamic stability of ball-end milling of AISI D6 hardened steel. Mater Res 2019;22:1–9.

[176] Tan L, Yao C, Ren J, Zhang D. Effect of cutter path orientations on cutting forces , tool wear , and surface integrity when ball end milling TC17. Int J Adv Manuf Technol 2017;88:2589–602.

[177] Kang MC, Kim KK, Lee DW, Kim JS, Kim NK. Characteristics of inclined planes according to the variations of cutting direction in high-speed ball-end milling. Int J Adv Manuf Technol 2001;17:323–9.

[178] Wojciechowski S, Maruda RW, Barrans S, Nieslony P, Krolczyk GM. Optimisation of machining parameters during ball end milling of hardened steel with various surface inclinations. Measurement 2017;111:18–28.

[179] Zhang PR, Liu ZQ, Guo YB. Machinability for dry turning of laser cladded parts with conventional vs. wiper insert. J Manuf Process 2017;28:494–9.

[180] Jha JS, Toppo SP, Singh R, Tewari A, Mishra SK. Deformation behavior of Ti-6Al-4V microstructures under uniaxial loading: Equiaxed Vs. transformed-β microstructures. Mater Charact 2021;171:110780.

[181] Shyha I, Gariani S, El-Sayed MA, Huo D. Analysis of microstructure and chip formation when machining Ti-6Al-4V. Metals (Basel) 2018;8.

[182] Hou J, Zhou W, Duan H, Yang G, Xu H, Zhao N. Influence of cutting speed on cutting force, flank temperature, and tool wear in end milling of Ti-6Al-4V alloy. Int J Adv Manuf Technol 2014;70:1835–45.

[183] Ng E, Engineering M. Experimental Evaluation of Cutter Orientation When Ball Nose End Milling Inconel 718™. J Manuf Process 2000;2:108–15.

[184] Rahman MA, Rahman M, Kumar AS. Chip perforation and 'burnishing–like' finishing of Al alloy in precision machining. Precis Eng 2017;50:393–409.

[185] Sonawane H, Joshi SS. Modeling of chip geometry in ball-end milling of superalloy using strains in deformed chip (SDC) approach. Int J Mach Tools Manuf 2018;130–131:49–

64.

[186] Gil FJ, Ginebra MP, Manero JM, Planell JA. Formation of a-Widmanstatten structure: effects of grain size and cooling rate on the Widmanstatten morphologies and on the mechanical properties in Ti6Al4V alloy. J Alloys Compd 2001;329:142–52.

[187] Lütjering G. Influence of processing on microstructure and mechanical properties of (α + β) titanium alloys. Mater Sci Eng A 1998;243:32–45.

[188] Galindo-Fernández MA, Mumtaz K, Rivera-Díaz-del-Castillo PEJ, Galindo-Nava EI, Ghadbeigi H. A microstructure sensitive model for deformation of Ti-6Al-4V describing Cast-and-Wrought and Additive Manufacturing morphologies. Mater Des 2018;160:350–62.

[189] Schoop J, Sales WF, Jawahir IS. High speed cryogenic finish machining of Ti-6Al4V with polycrystalline diamond tools. J Mater Process Technol 2017;250:1–8.

[190] Bertolini R, Lizzul L, Bruschi S, Ghiotti A. On the surface integrity of Electron Beam Melted Ti6Al4V after machining. Procedia CIRP, vol. 82, 2019.